



**Universitat de les
Illes Balears**

Doctoral Thesis

2019

**SUBMESOSCALE DYNAMICS IN THE
WESTERN MEDITERRANEAN SEA**

María Esther Capó Truyols



Universitat de les Illes Balears

Doctoral Thesis

2019

Doctoral programme in Physics

SUBMESOSCALE DYNAMICS IN THE WESTERN MEDITERRANEAN SEA

María Esther Capó Truyols

Thesis Supervisor: Alejandro Orfila Förster

Thesis Supervisor: Evan Mason

Thesis Tutor: Romualdo Romero March

Doctor of Philosophy in Physics

University of the Balearic Islands



Universitat
de les Illes Balears

This thesis has been written by María Esther Capó Truyols under the supervision of Dr. Alejandro Orfila Förster and Dr. Evan Mason.

Palma de Mallorca, October 28, 2019

Supervisors:

A blue ink signature consisting of several vertical and diagonal strokes, appearing to be the name 'Alejandro Orfila Förster'.

A blue ink signature consisting of a series of loops and curves, appearing to be the name 'Dr. Evan Mason'.

PhD Student:

A blue ink signature consisting of a large, flowing loop and a smaller stroke, appearing to be the name 'María Esther Capó Truyols'.

Agradecimientos

Mi primer y mayor agradecimiento es, por supuesto, para Jano. Aquella propuesta tuya – “¿Y por qué no haces la tesis?”–, cinco años atrás, fue una de tus mejores ocurrencias. Desde aquel momento ocupas el puesto de honor en mi directorio personal de frases célebres. Gracias, mejor amigo.

Gracias, Evan, por tus sugerencias: me sugeriste que leyera aquellos papers que finalmente inspiraron mi tesis; me sugeriste que le enviara aquel manuscrito a Jim; y me sugeriste que me pasara a Python y que dejara estar las carpetitas y trabajara desde la terminal. Gracias por todo lo que he aprendido contigo y, sobre todo, por tu actitud y tu enorme paciencia.

Estoy sentada frente a mi querido *Predator*, con mis nuevas gafas de ver de cerca, pensando en alguna frase solemne que describa lo que ha supuesto para mí todo este proceso. Pero sólo se me ocurre esta expresión: ¡Me lo he pasado bomba!. Supongo que habré tenido algún mal momento, pero ya no lo recuerdo... ventajas de hacerse mayor. Me divierte y me hace feliz mi trabajo, estudiar, leer artículos, aunque cada vez se editen con la letra más pequeña, esas charlas sobre la física y lo físico con Ismael y Jano a la hora de comer, aprender cosas nuevas todos los días y seguir sin entender muchas otras... poc a poc.

Gracias a todos los que habéis formado parte de mi “circunstancia” durante estos años. Compañeros del Imedea: Ismael, Dani, Juanma, Arantxa, Alex, Vero, Bárbara, Angel, Antonio y muchos más... Personal de administración, de limpieza, conserjes... Gràcies, Miquel i Juanjo, quina paciència teniu!. Gracias Simón y Ananda por vuestro apoyo. Gracias, Marta, por tu ayuda y por esos cafés con unas risas.

Jim, thank you so much for giving me this opportunity.

Gràcies, família: Alin, Juana, Octavio, Pepe, Martí, Mateo, Lupe... no enteneu res del que faig però confiau en mi perquè sabeu que m’encanta. Vos estim.

Gràcies, Víctor, per estimar-me tant. Ets sa meva vida, t'estim, t'admir i estic tan orgullosa de tu!

Gràcies amics: Jano (otra vez tú), Maria, Antònia, Ramon i companyia... perquè sempre estau allà, i sobre tot perquè reim molt i ho passam molt bé junts. Gràcies 74, per aquest cor tan gran que tens, perquè sempre estàs content i per mi només tens paraules d'admiració, suport i aquests “piropos” que me fan riure tant... i gràcies per fer-me es sopar!

Y hablando de comida, gracias a las chicas de Tot Casolà, que me han hecho el

dinar casi todos los días durante estos años.

Mi más sincero agradecimiento a Romain Escudier por permitirme utilizar los datos de su simulación, punto de partida de esta Tesis.

Este trabajo ha sido financiado por el Proyecto Intramural EVOS del Consejo Superior de Investigaciones Científicas (CSIC 201530E067) y por la Universitat de les Illes Balears, a través de la acción especial del Govern de les Illes Balears (AAEE110/2017).

Abstract

The transition from mesoscale to submesoscale dynamics is investigated in the western Mediterranean Sea (WMed) using a set of ROMS model simulations.

The research is structured in a series of sequential stages covering the mesoscale-to-submesoscale range, starting from a regional overview of the WMed ocean circulation and zooming in towards local processes.

The mesoscale exploration is assessed in terms of the Lorenz energy cycle (LEC), which provides a quantification of the kinetic-potential energy exchanges through eddy-mean flow interactions. The sources of eddy kinetic energy are analyzed by applying a regional formulation of the LEC to 18 years of the ROMSWMED32 numerical simulation at eddy-resolving resolution (3.5 km), which allows identification of whether the energy exchange between the mean and eddy flow is local or nonlocal. The patterns of energy conversion between the mean and eddy kinetic and potential energy are estimated in three subregions of the domain: the Alboran Sea, the Algerian Basin, and the Northern Basin.

Results from the LEC analysis reveal that the Alboran Sea is the most energetic region in the WMed. The spatial characterization of the energy conversion routes, together with the physical and dynamical characteristics of the area, hints at two principal submesoscale mechanisms involved in maintaining balance: topographic vorticity generation (TVG) and frontogenesis (FG).

The transition toward the submesoscale is explored in the Alboran Sea by means of two nested, realistic simulations covering this region with increasing horizontal resolutions ranging from 1.5 km (WMed1500) to 0.5 km (Alb500). Unbalanced submesoscale dynamics emerge in the finer solution as the model resolution is increased.

The occurrence of TVG and FG in Alb500 does not display a clear spatial nor temporal variability which facilitates an overall statistical approach. Instead, our analysis is focused on particular events of FG and TVG which are considered to be representa-

tive of the Alboran Sea dynamics.

TVG is explored and quantified using the barotropic vorticity balance equation, in which the generation of vorticity through flow-topography interaction relies on contributions from bottom stress and form drag, the latter being the principal source.

FG is analyzed in a recurrent, intense density front located at the eastern edge of the permanent western anticyclonic gyre (WAG) which has a similar structure to that of the climatological Almeria-Oran front. Alb500 accurately reproduces the process of FG in this front, instigated by the straining of the mesoscale velocity field, and the generation of ageostrophic secondary circulation, exhibiting transient downwelling events reaching peak vertical velocities of $\mathcal{O}(1)$ km day $^{-1}$.

The vertical velocity background revealed throughout the analysis of the Alb500 solution suggests that vertical motions in the Alboran Sea might stem from additional sources of perturbations in the submesoscale range, such as mixed layer instabilities, tidal effects or topographic internal waves. Exploring these mechanisms and the possible interactions among them is beyond the scope of this Thesis; planned further analysis of the Alb500 simulation using Lagrangian techniques is likely to shed light on such processes.

Resumen

La transición de la mesoscala a la submesoscala se investiga en el Mar Mediterráneo occidental mediante una serie de simulaciones con el modelo ROMS.

El estudio se compone de varias etapas que cubren este rango de escalas, partiendo de una descripción regional de la circulación en el Mediterráneo occidental hacia los procesos que tienen lugar a escalas locales.

El análisis de mesoscala se lleva a cabo en términos del ciclo de energía de Lorenz (LEC, de sus siglas en inglés), que permite cuantificar los intercambios de energía cinética y potencial que tienen lugar en el fluido mediante interacciones entre el flujo medio y el flujo turbulento. Las fuentes de energía cinética turbulenta se investigan a partir de ROMSWMED32, una simulación de mesoscala (3.5 km) que abarca un periodo de 18 años. Una formulación regional del LEC permite discernir si dichos intercambios de energía tienen un origen local o remoto.

Los patrones de conversión de energía se investigan en tres subregiones: Mar de Alborán, Cuenca de Argelia y Cuenca de Norte.

Los resultados del LEC revelan que el Mar de Alborán es la zona más energética del Mediterráneo occidental. La distribución espacial de las rutas de conversión de energía, junto con las características geográficas y dinámicas de esta región, sugieren dos mecanismos de submesoscala como principales responsables del mantenimiento del balance de energía: generación topográfica de vorticidad (TVG, de sus siglas en inglés) y frontogénesis (FG).

La transición hacia la submesoscala en el Mar de Alborán se investiga mediante dos simulaciones realistas anidadas que cubren esta región, con resoluciones que aumentan desde 1.5 km (WMed1500) hasta 0.5 km (Alb500). La dinámica de submesoscala se aprecia en Alb500 según aumenta la resolución.

Los procesos de TVG y FG en Alb500 no presentan una clara variabilidad espacial ni temporal que permita una descripción estadística de los mismos. Por tanto, el análisis

de estos mecanismos se lleva a cabo sobre eventos aislados que pueden considererse representativos de la dinámica del Mar de Alborán.

La cuantificación y el análisis de la TVG se realiza a partir de la ecuación del balance de vorticidad barotrópica. La generación de vorticidad debido a la interacción de la corriente con la topografía se evalúa en términos del esfuerzo cortante de fondo (en inglés, *bottom stress*) y del arrastre (en inglés, *form drag*), siendo este último la fuente principal.

La FG se analiza en un intenso y recurrente frente de densidad localizado en el extremo oriental de giro anticiclónico del oeste (WAG, de sus siglas en inglés) cuya estructura es muy similar a la del habitual frente de Almería-Oran. Alb500 reproduce de forma precisa el proceso de FG de este frente, inducido por el aumento de tensión del campo de velocidad geostrófica superficial, así como el desarrollo de la circulación secundaria ageostrófica asociada al frente, con episodios de intenso movimiento vertical descendente (en inglés, *downwelling*) alcanzando velocidades del orden de 1 km al día.

El campo de velocidad vertical que revela el análisis de la simulación Alb500 sugiere que los movimientos verticales en el Mar de Alborán pueden ser originados por otros tipos de perturbaciones de submesoscala, tales como inestabilidades en la capa de mezcla, las mareas, o bien ondas internas de origen topográfico. La exploración de estos mecanismos y de las posibles interacciones que tiene lugar entre ellos va más allá de los objetivos de esta Tesis, si bien se pretende profundizar en el estudio de dichos procesos con un futuro y exhaustivo análisis de la simulación Alb500 utilizando técnicas lagrangianas.

Resum

La transició de la mesoescala a la submesoescala s'investiga a la Mar Mediterrània occidental a partir d'una sèrie de simulacions amb el model ROMS.

L'estudi està format per varis etapes que abasten aquest rang d'escales, des d'una descripció regional de la circulació a la Mediterrània occidental, fins als processos que tenen lloc a escales locals.

L'anàlisi de mesoescala es realitza en termes del cicle d'energia de Lorenz (LEC, de les seves sigles en anglès), que permet quantificar els intercanvis d'energia cinètica i potencial que tenen lloc en un fluid degut a les interaccions entre el fluxe mitjà i el fluxe turbulent. Les fonts d'energia cinètica turbulenta s'investiguen amb ROMSWMED32, una simulació de mesoescala (3.5 km) que abarca un període de 18 anys. Una formulació regional del LEC permet diferenciar si aquests intercanvis d'energia són d'origen local o remot.

Els patrons de conversió d'energia s'investiguen a tres sub-regions: Mar d'Alboran, Conca d'Algèria i Conca del Nord.

Els resultats del LEC mostren que la Mar d'Alboran és la zona més energètica de la Mediterrània occidental. La distribució espacial de les rutes de conversió d'energia, juntament amb les característiques geogràfiques i dinàmiques d'aquesta regió, suggereixen dos mecanismes de submesoescala com a principals responsables del manteniment del balanç d'energia: generació topogràfica de vorticitat (TVG, de les seves sigles en anglès) i frontogènesi (FG).

La transició cap a la submesoescala a la Mar d'Alboran s'investiga a partir de dues simulacions realistes niuades que cobreixen aquesta regió, amb resolucions que augmenten des de 1.5 km (WMed1500) fins a 0.5 km (Alb500). La dinàmica de submesoescala s'aprecia en Alb500 segons augmenta la resolució.

Els processos de TVG i FG simulats amb Alb500 no presenten una clara variabilitat espacial ni temporal que faciliti la seva descripció estadística. Per tant, l'anàlisi

d'aquests mecanismes es realitza a partir d'esdeveniments aïllats que es poden considerar representatius de la dinàmica de la Mar d'Alborán.

La quantificació i l'anàlisi de la TVG es realitza mitjançant l'equació de balanç de la vorticitat barotòpica. La generació de vorticitat per interacció del corrent amb la topografia s'avalua en termes de l'esforç de tall (en anglès, *bottom stress*) i de l'arrossegament (en anglès, *form drag*), que n'és la principal font.

La FG s'analitza en un intens i recurrent front de densitat localitzat a l'extrem oriental del gir anticilònic de l'Oest (WAG, de les seves sigles en anglès) d'estrucció molt similar a l'habitual front d'Almeria-Orà. Alb500 simula de forma precisa el procés de FG d'aquest front, provocat per l'augment de tensió del camp de velocitat geostròfica superficial, així com la generació de la circulació secundària ageostròfica associada al front, amb episodis d'intens moviment vertical descendent (en anglès, *downwelling*) assolint velocitats de l'ordre d'1 km per dia.

El camp de velocitat vertical que mostra l'anàlisi de la simulació Alb500 suggereix que els moviments verticals a la Mar d'Alboran podrien ser causats per altres tipus de perturbacions de submesoescala, tals com inestabilitats dins la capa de mescla, efectes de la marea, o bé ones internes d'origen topogràfic. L'exploració d'aquests mecanismes i de les seves possibles interaccions no és l'objectiu d'aquesta Tesi, si bé la futura i exhaustiva anàlisi de la simulació Alb500 mitjançant tècniques Lagrangianes preten profunditzar en el coneixement d'aquests processos.

Contents

List of Abbreviations	ix
1 Introduction	1
1.1 Scales in the ocean circulation	2
1.2 Submesoscale processes	4
1.3 Motivation	6
1.4 Objectives and methods	6
1.5 Analysis region	7
2 Model configuration and data	15
2.1 The ROMS model	16
2.1.1 The ROMSWMED32 simulation	18
2.1.2 WMed1500 and Alb500 nested simulations	20
2.2 Discussion	29
3 The Lorenz energy cycle: estimation of the energy conversion routes in the western Mediterranean Sea.	33
3.1 Energy analysis	34
3.1.1 Kinetic energy and available potential energy	34
3.1.2 The Lorenz Energy Cycle	36
3.2 Results	40
3.2.1 Surface mean currents	40
3.2.2 Kinetic Energy analysis	42

3.2.3	Energy budgets	44
3.2.4	Regional LEC and mean-eddy flow interactions	46
3.3	Discussion	51
4	Mesoscale to submesoscale transition in the Alboran Sea	57
4.1	Data	59
4.2	Mean circulation	59
4.2.1	Surface mesoscale circulation	61
4.2.2	3D structure	61
4.3	The submesoscale transition	71
4.3.1	The surface signature of SMCs	71
4.3.2	Energy fluxes	75
4.4	Discussion	77
5	Submesoscale processes	81
5.1	Topographic vorticity generation	82
5.2	Frontogenesis	99
5.3	Discussion	107
6	Summary and Conclusions	109
A	The Rossby radius of deformation.	113
B	Vorticity	115
C	ROMSWMED32 validation	117
C.1	Some validation aspects	117
C.2	Assessment of statistical equilibrium and model spin-up	118
D	The RANS equations	121
E	Notes about derivation of the KE balance equations	123

List of Abbreviations

3F: Cape Three Forks

AC: Algerian Current

AJ: Atlantic Jet

Al: Almeria

AO: Almeria-Oran

APE: Available Potential Energy

AW: Atlantic Water

BC: Balearic Current

BV: Barotropic Vorticity

CFL: Courant-Friedrichs-Lowy

CI: Centrifugal Instability

CM: Cala de Mijas

CS: Camarinal Sill

EAG: Eastern Anticyclonic Gyre

EAPE: Eddy Available Potential Energy

EKE: Eddy Kinetic Energy

FG: Frontogenesis

KE: Kinetic Energy

KPP: K-Profile Parameterization

- LEC:** Lorenz Energy Cycle
- LIW:** Levantine Intermediate Water
- MAPE:** Mean Available Potential Energy
- MKE:** Mean Kinetic Energy
- ML:** Mixed Layer
- MLEs:** Mixed Layer Eddies
- MLIs:** Mixed Layer Instabilities
- Mo:** Motril
- MW:** Mediterranean Water
- NC:** Northern Current
- PE:** Potential Energy
- PGE:** Pressure Gradient Errors
- QG:** Quasigeostrophic
- RANS:** Reynolds Averaged Navier Stokes
- ROMS:** Regional Oceanic Modeling System
- SCV:** Submesoscale Coherent Vortex
- SMCs:** Submesoscale Currents
- SoG:** Strait of Gibraltar
- SSH:** Sea Surface Height
- THC:** Thermohaline Circulation
- TN:** Tarifa Narrows
- TTW:** Turbulent Thermal Wind
- TVG:** Topographic Vorticity Generation
- WAG:** Western Anticyclonic Gyre
- WMed:** Western Mediterranean Sea

Chapter 1

Introduction

While most of the energy input from the atmosphere into the ocean is absorbed by large scale currents, the necessary dissipation required to maintain balance takes place at molecular scales. In between these extremes, a variety of intermediate scale processes necessarily occur to set the pathways towards reaching energy equilibrium.

Recent studies in ocean (sub)mesoscale processes have shown increasing evidence of the interactions among the different scales. In the ocean, kinetic energy (KE) is mostly concentrated in the time-varying flow, while the potential energy (PE) is stored in the mean circulation. The Lorenz energy cycle (LEC) is an effective tool for providing a quantitative assessment of the energy generation, dissipation, and conversion terms among the different energy forms. The LEC was first implemented in the atmosphere by Lorenz (1955), who proposed the study of the energy cycle based on the description of the steady-state balance of the four basic energy reservoirs: the KE and the available PE of the mean flow and of the time-varying circulation. For oceanic turbulent flows, Harrison and Robinson (1978) presented a pioneer work involving an exhaustive analysis of the LEC from a numerical ocean circulation experiment; Oort et al. (1994) addressed the problem of the large-scale energetics of the global ocean from a variety of ocean surface observations and, more recently, Storch et al. (2012) provided an estimate of the LEC for the World Ocean derived from a $1/10^\circ$ numerical simulation.

Available observational datasets still remain too sparse in space and time and cannot be used to study the energy conversion pathways between the mean and time-varying flow. In this regard, numerical models can produce realistic simulations long enough to achieve a statistically stationary ocean state so that the dynamics can be investigated from the analysis of energy budgets involved in the balance equations.

1.1 Scales in the ocean circulation

Ocean circulation is thus governed by processes within a wide range of time and spatial scales, from the planetary scale long term thermohaline circulation to the short-lived small scale eddies and meanders of the order of few km or less. Between these limits, oceanic motions are mediated by a broad spectrum of flow structures and by the interactions among them.

At higher levels, boundary currents constitute an essential component of the circulation. They are mainly driven by winds, tides and salinity and temperature gradients, and are steered by the shape of the basins and by Earth's rotation. A few examples are the Gulf Stream in the North Atlantic, the Kuroshio in the Pacific, the Benguela in the South Atlantic or the Agulhas in the Indian Ocean. At the basin scale, the gyres are rotating current systems with diameters of thousands of kilometers and the largest and more permanent boundary currents are found at their rims. The five major gyres occupy the northern and southern half of the Atlantic and the Pacific oceans and the southern Indian Ocean.

With typical horizontal scales between $\mathcal{O}(10\text{-}100)$ km and timescales on the order of several weeks or months, mesoscale eddies contain most of the energy transferred from the atmosphere into the ocean by winds, heat and fresh-water fluxes. They play an essential role in carrying properties such as heat, salt and geochemical tracers around the ocean. The largest mesoscale eddies primarily stem from strong horizontal shear instabilities in the large-scale boundary currents, although smaller structures can emerge (not necessarily in the vicinity of a boundary current) from baroclinic instabilities promoted by horizontal density gradients. Even though only the surface signature of mesoscale eddies can be detected from satellite images of sea surface height or temperature, they are three dimensional structures that can extend in the vertical down into the pycnocline.

Dynamically, the mesoscale field is in geostrophic balance, with the Coriolis force balancing the pressure gradient term. In this regard, the horizontal scales of mesoscale eddies can be estimated from the Rossby radius of deformation, as this is the scale at which the effects of Earth rotation become as important as the gravitational forces. The barotropic or external Rossby radius, $R_0 = \sqrt{gH}/f$, where g is gravitational acceleration, H is the water column depth and f the Coriolis parameter, can be defined as the distance over which deformations of the free surface by Coriolis force are balanced by the gravitational tendency to flatten the surface (Pedlosky, 2013). In a more realistic ocean, these horizontal scales also depend on the vertical stratification, characterized by the Brunt-Väisälä frequency $N(z)$ (z is the vertical coordinate), and they are better determined using the *baroclinic* Rossby radius, estimated by Chelton et al. (1998) as $R_1 = \int_{-H}^0 N(z) dz / \pi f$ (see Appendix A for details).

Going down towards smaller scales, ocean submesoscale currents (SMCs) are characterized by horizontal scales of $\mathcal{O}(1)$ km, vertical lengths of $\mathcal{O}(10\text{-}100)$ m and a duration of hours to days (McWilliams, 2016). Beyond the differences in the scales, SMCs are ageostrophic motions in which inertia overcomes the Coriolis force, thus the dynamics are dominated by advection.

A quantitative distinction between mesoscale and submesoscale motions can be done in terms of the adimensional Rossby (\mathcal{R}_o) and Froude (\mathcal{F}_r) numbers, which provide a measure of advection, rotation, stratification and gravitational effects:

- $\mathcal{R}_o = V/fl$, where V and l are the characteristic horizontal velocity and length scales, respectively, measures the ratio between inertial and Coriolis forces (or between the vertical relative vorticity, $\zeta = \partial v/\partial x - \partial u/\partial y$, where u and v are the horizontal velocity components in the x and y directions, respectively, and the planetary vorticity, defined by f in the vertical; see Appendix B).
- $\mathcal{F}_r = V/Nh$, with h being the vertical length scale, compares inertial and gravitational forces (or an advecting velocity and the phase speed of an internal gravity wave).

Geostrophically balanced motions are characterized by $\mathcal{R}_o, \mathcal{F}_r \ll 1$, while SMCs have $\mathcal{O}(1)$ \mathcal{R}_o and \mathcal{F}_r numbers.

In the same range of spatial and temporal scales as SMCs, inertia-gravity waves (IGWs, including near-inertial waves and internal tides) are dominant modes of high-

frequency internal variability in the ocean (Zaron and Rocha, 2018). IGWs can interact with unbalanced SMCs, with possible consequences in the mixing process and in the energy transfers towards dissipation, although these interaction mechanisms and their relevance are still open issues.

The route to energy dissipation is completed at the microscale by the largely isotropic three-dimensional turbulence (with $h \sim l$), characterized by the highest \mathcal{R}_o and \mathcal{F}_r .

1.2 Submesoscale processes

Several mechanisms have been proposed for extracting energy from geostrophic motions towards dissipation involving a forward energy cascade. Primarily at the ocean surface, unbalanced submesoscale processes have been widely identified and comprehensively described; *e.g.*, mixed layer instabilities (MLIs) associated with weakly stratified layers (Boccaletti et al., 2007; Thomas et al., 2008; Fox-Kemper et al., 2008) or frontogenesis in the intense density fronts and filaments (Capet et al., 2008; McWilliams, 2016; Mahadevan, 2016) can be a major contribution to energy release. At the bottom, a mechanism consisting of dissipative interaction of the geostrophic flow against topography has been recently proposed (Molemaker et al., 2015; Gula et al., 2015a, 2016).

MLIs occur in the weakly stratified mixed layer (ML) when lateral buoyancy gradients, $\nabla_h b$ (the subscript h denotes the horizontal vector component), are enhanced by atmospheric forcing (surface fluxes) or by the mesoscale eddy strain field, leading to the generation of mixed layer eddies (MLEs) and fronts (Boccaletti et al., 2007; Fox-Kemper et al., 2008; Thomas et al., 2008; McWilliams, 2016). MLEs are especially active in winter, when mixing is promoted by surface atmospheric cooling. By the action of gravity, buoyancy gradients are dynamically active and baroclinic instabilities develop, releasing available potential energy in the form of a secondary ageostrophic circulation. The secondary circulation acts to restratify the ML by tilting isopycnals toward the horizontal. Because of the weak stratification (small N) these instabilities lie in the submesoscale range, with spatial and time scales of $\mathcal{O}(1)$ km and $\mathcal{O}(1)$ day, respectively (Boccaletti et al., 2007).

Frontogenesis (FG; Hoskins and Bretherton, 1972; Rudnick and Davis, 1988) is a

leading submesoscale mechanism in the upper ML, with the presence of strong lateral density gradients, weak stratification, vertical shear and relatively small Rossby radius based on the mixed layer depth (Thomas et al., 2008) and thus enhanced \mathcal{R}_o , \mathcal{F}_r numbers. The process is instigated by the strengthening of the $\nabla_h b$, promoted by the straining of the mesoscale velocity field. After initiation by the large scale deformation flow, the along-front geostrophic balance is disrupted and a secondary circulation develops in the cross-front plane. In the ML, this secondary circulation is mainly driven by vertical mixing, so the classical *geostrophic thermal wind* balance relation (with the cross-front pressure gradient balancing the Coriolis force associated with the alongfront current) is no longer valid. Instead, a *turbulent thermal wind* (TTW) equation predicts that the buoyancy gradient in the ML will be mostly balanced by the vertical mixing of momentum (D'Asaro, 1988; Capet et al., 2008; Gula et al., 2014; McWilliams, 2016). Since the development of the mathematical theory of frontogenesis in the context of the atmosphere (Hoskins and Bretherton, 1972), this process has been widely studied around the world ocean, both from observations and from a modeling perspective (Spall, 1995; Capet et al., 2008).

In the bottom layers, the interaction of the mesoscale currents with topography has been recently proposed as a primary route to dissipation. Commonly referred to as topographic vorticity generation (TVG), this mechanism involves a sequence of processes through which the impacting mean flow creates frictional torques in the bottom boundary layer, generating vertical vorticity and transferring the energy to submesoscale wakes which provide the necessary shear to drive molecular mixing and dissipation. Initially proposed by D'Asaro (1988), vorticity generation by flow-topography interaction has been investigated in the principal boundary currents (Molemaker et al., 2015; Gula et al., 2015a) and also at a regional scale (D'Asaro, 1988; Hristova et al., 2014; Vic et al., 2015; Srinivasan et al., 2017; Morvan et al., 2019).

Beyond SMCs, other mechanisms have also been identified as intermediate scale routes to dissipation (McWilliams, 2016), such as spontaneous emission of inertia-gravity waves in the ocean interior (Ferrari and Wunsch, 2009; Thomas et al., 2013) or topographic generation of internal gravity waves (Nikurashin et al., 2013; Lamb, 2014), although their study is beyond our goals here.

1.3 Motivation

Beside their dynamical role in the general circulation and the consequences for transport, mixing and energy dissipation, submesoscale motions are crucial in the evolution and variability of biogeochemical processes. Modulation of mixed layer stratification by SMCs can affect the residence time of phytoplankton in the euphotic zone, affecting growth rates, biogeochemical fluxes and biomass community structure (Mahadevan, 2016; Lévy et al., 2018); they pose important implications for ocean carbon and heat storage (Omand et al., 2015) with subsequent impacts on marine ecosystems (Bracco et al., 2019) and climate (Su et al., 2018).

Given their major role in multiscale dynamics and their impact on life sciences, SMCs have become a primary target for the ocean research community, and substantial efforts are being made to improve research resources at a multidisciplinary level.

In recent decades, large-scale ocean processes down to the mesoscale have been comprehensively investigated using remote sensing techniques combined with *in situ* data, and today we can confidently assert that they are fairly well understood. In contrast, processes driving the energy transition from geostrophic motions towards dissipation occur at spatial and temporal scales which are difficult to detect by observations. Besides the great advances in satellite altimetry and the increasing deployment of *in situ* observational resources (*i.e.*, Argo floats, ship surveys, autonomous gliders, ...), SMCs involve not only the uppermost layers but the full water column and evolve over time scales which overcome our observation capabilities.

In order to fill this gap, the modeling community is making great progress in improving both model techniques and computational resources to produce highly realistic simulations covering mesoscale to submesoscale motions. In the absence of appropriate observational methods, models are the best available tool for exploring the subsurface ocean, providing enough data continuity and resolution in space and time.

1.4 Objectives and methods

In this Thesis we use a set of model simulations to investigate the mesoscale to submesoscale transition in the western Mediterranean Sea (WMed), exploring the role of SMCs in setting the energy pathways from geostrophically balanced dynamics towards

dissipation.

The research is structured in a series of sequential stages covering the mesoscale-to-submesoscale range, starting from a regional overview of the WMed ocean circulation and zooming in towards local processes. Thus, different datasets are needed to accurately reproduce the scales involved in the transition. A full description of the several model configurations performed and/or analyzed to carry out this research is presented in Chapter 2.

The connection between both ocean scales in the WMed is assessed in terms of the kinetic-potential energy exchanges through eddy-mean flow interactions. This is presented in Chapter 3, through an estimation of the LEC and the regional distribution of the principal energy conversion routes. Supported by the known local dynamical behavior, analysis of the spatial patterns of the energy routes helps to discern the character of the (submesoscale) processes presumably involved in the conversion.

From this point, we focus our submesoscale exploration on the most energetic spot within the analyzed domain: the Alboran Sea. The transition from mesoscale to submesoscale in this sub-basin is assessed in Chapter 4, from which we hypothesize that two dominant processes drive the energy conversion pathways in this region: (1) frontogenesis, a primary source of SMCs in the upper mixed layer, and (2) topographic vorticity generation at the bottom. These processes are explored in Chapter 5.

1.5 Analysis region

The western Mediterranean Sea

The Mediterranean Sea is a large semi-enclosed basin extending between 30°N and 45°N and between 6°W and 37°E (Fig. 1.1). It can be divided into two parts, the eastern and western sub-basins, separated by the Strait of Sicily, a channel about 145 km wide and with a maximum depth of 316 meters, which constrains the flow from one side to the other as well as water properties and dynamics. On the western edge, the Strait of Gibraltar (SoG) constitutes the unique gateway to the Atlantic Ocean through which water exchange between both basins takes place. The Strait's narrowest point is 14.3 km wide, while depth ranges between 300 and 900 meters (Fig. 1.2).

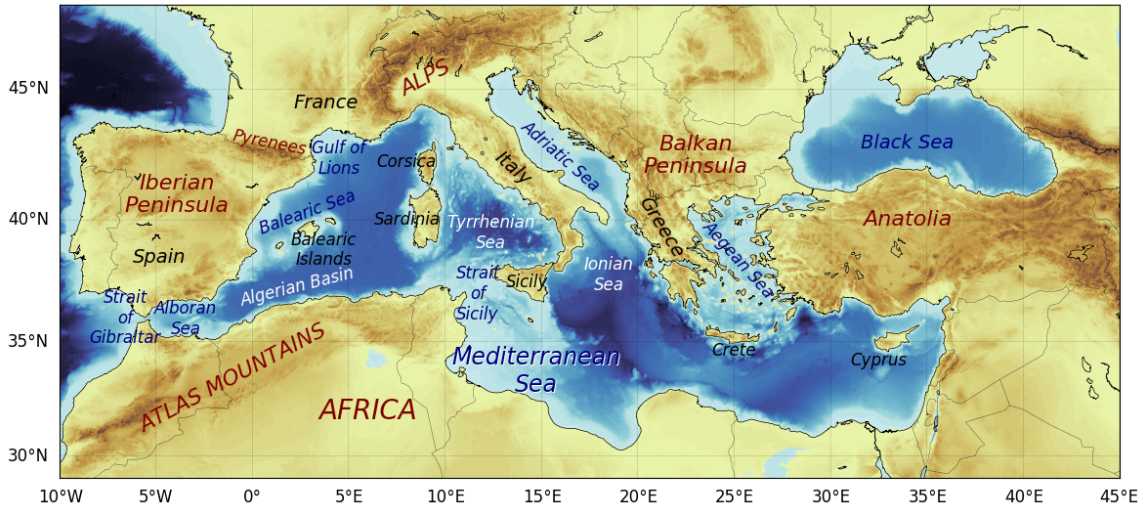


Figure 1.1: A general overview of the Mediterranean Sea with some locations of interest referred to in the text.

The region has complex topography including high mountains, numerous peninsulas, capes and a myriad of islands of many different shapes and sizes depicting a complicated bathymetry, which in conjunction with atmospheric and internal forcing (mainly wind stress and buoyancy fluxes driven by heat and freshwater fluxes at the surface) inevitably condition the dynamical behavior. As a result, circulation is characterized by processes covering a broad range of interacting spatial and temporal scales (Fig. 1.3).

The Mediterranean thermohaline circulation (THC) is the main large scale feature (Cacho et al., 2000; Robinson et al., 2001; Malanotte-Rizzoli et al., 2014). At the surface, the THC is forced by Atlantic Water (AW) inflow through the SoG and by buoyancy loss (enhanced salinity) experienced throughout the basin, due to an excess of evaporation over precipitation and river inflow. During winter, the cooling of the saltier surface water makes it sink, generating the Levantine intermediate water (LIW) in the eastern basin and, less frequently, the Mediterranean deep water in the western basin (mainly in the Gulf of Lions and in the Adriatic Sea, the regions most exposed to episodes of intense cold northerly winds). The LIW, occupying the intermediate layers (200-1000 m), is the main source of the Mediterranean outflow crossing the SoG towards the Atlantic, thus completing the THC. Moving to smaller scales (Figure 1.4) we find quasi-permanent boundary currents bounding the two large cyclonic gyres dominating the western and eastern sub-basins; intermittent currents; jets; meanders and ring vortices; permanent mesoscale cyclonic and anticyclonic gyres and energetic

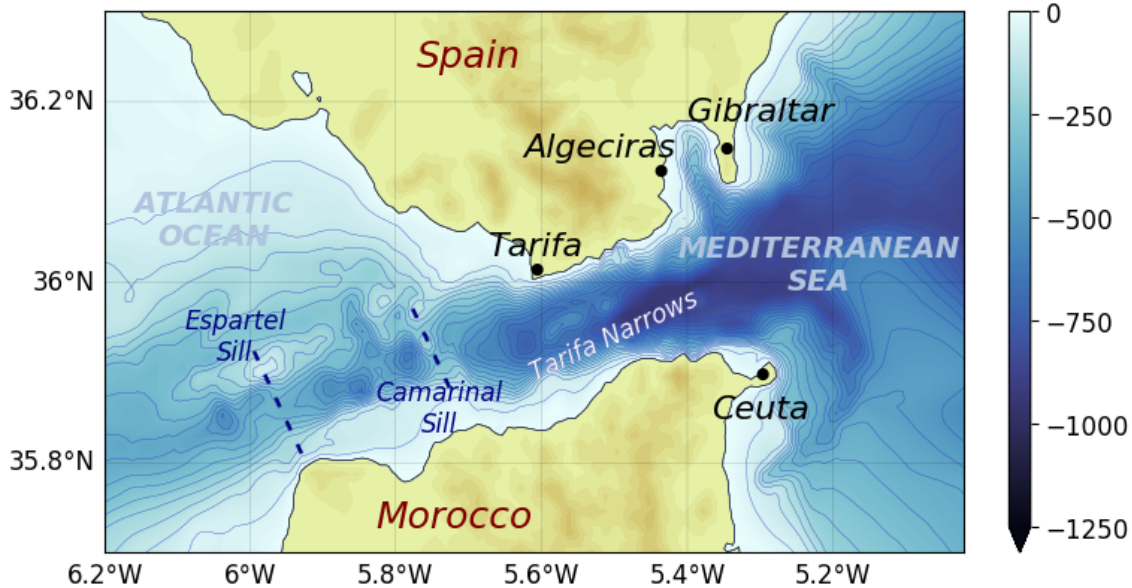


Figure 1.2: Bathymetry of the Strait of Gibraltar and locations of interest. Isobaths are plotted every 50 m. Dashed lines show the Espirail Sill and Camarinal Sill.

submesoscale eddies (Millot, 1999; Pinardi and Masetti, 2000; Robinson et al., 2001).

The upper limit for mesoscale processes cannot be accurately determined in this region so this is usually defined, in terms of temporal duration, to be smaller than the scale of the principal currents (Escudier, 2015). Focusing on the WMed region, the path of the large scale circulation is broadly delimited by three main boundary currents: east of the Alboran Sea, the Algerian current (AC) carries AW along the African coast towards Sicily; a branch of the AC continues southeast towards the eastern Mediterranean basin, and the rest flows along the western Italian coast crossing the Tyrrhenian Sea. When reaching the northern edge of the region, the water flows westward along the French and Spanish coast as the Northern Current (NC) and back towards the Alboran Sea, completing a cyclonic loop (Figure 1.4). Satellite observations have revealed interannual variability components in the mean currents as well as in the semi-permanent mesoscale structures which do not seem to correlate with external forcings but, rather, result from internal dynamics (Pinardi and Masetti, 2000; Pujol and Larnicol, 2005; Malanotte-Rizzoli et al., 2014).

The lower limit for the horizontal scales at which mesoscale processes occur in this region, estimated from R_1 , ranges between 5–15 km, depending on the location and the season (Beuvier et al., 2012; Escudier et al., 2016). Values derived from the

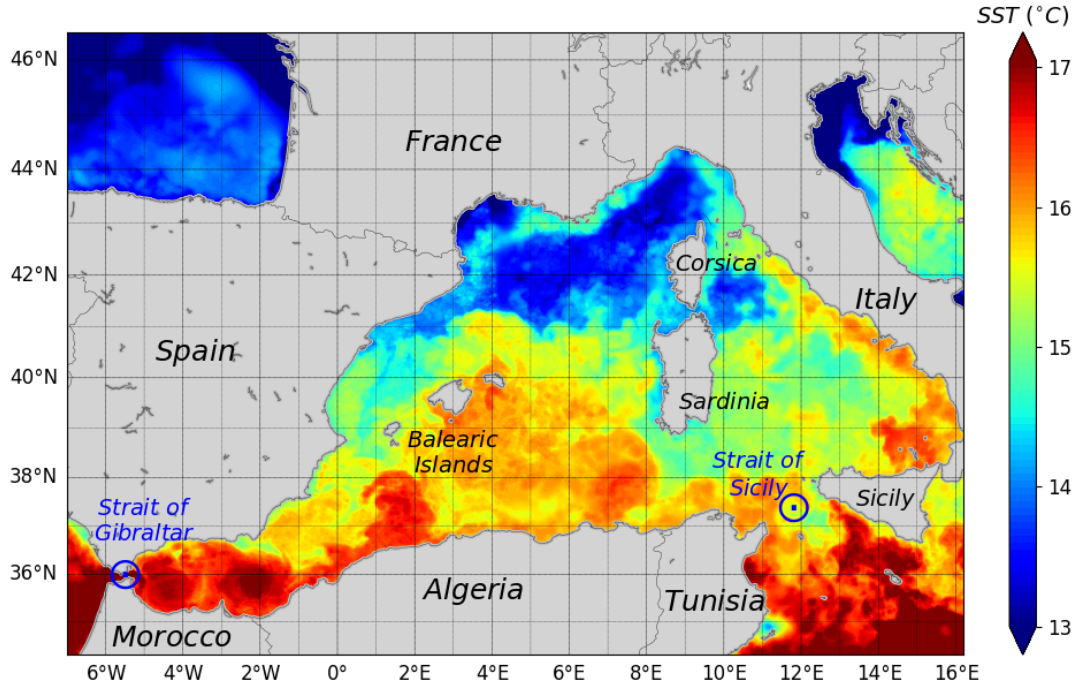


Figure 1.3: Snapshot of sea surface temperature on January 1, 2013 for the western Mediterranean Sea at 1 km resolution showing locations of interest. Source: L4 gridded product from GHRSSST.

statistical analysis of a 20-year mesoscale simulation (ROMSWMED32; Escudier, 2015, described in Chapter 2) show a marked seasonal variability for R_1 , with the minimum and maximum amounts recorded in February and August, respectively (Fig.1.5). The regional characterization displays the lowest values (4–9 km, from winter to summer) in the area of the Gulf of Lions, while the larger scales (13–17 km) are typical in the south. Besides the decrease of R_1 with latitude expected from its inverse proportionality with the Coriolis parameter, f , this north-south gradient is also consistent with the fact that stratification is much weaker in the northern regions (e.g., Gulf of Lions) that are affected by wind-induced mixing in winter.

Unraveling the (sub)mesoscale is a challenging task in this region, where the location, shape and bathymetric configuration of the basin appears to reduce the characteristic times and spatial scales which would be applicable in the larger oceans. Over the last several decades, much research has been done in the WMed to describe the multiscale circulation and its variability, from both observational techniques (Large et al., 1994; Millot, 1999; Ruiz et al., 2009; Renault et al., 2012; Mason and Pascual, 2013; Poulain et al., 2013; Pascual et al., 2017) and models (Molcard et al., 2002; Escudier



Figure 1.4: Schematic representation of the basin-scale surface circulation in the Mediterranean Sea, with the principal boundary currents and mesoscale gyres. Source: GRID Arendal www.grida.no/resources/5915.

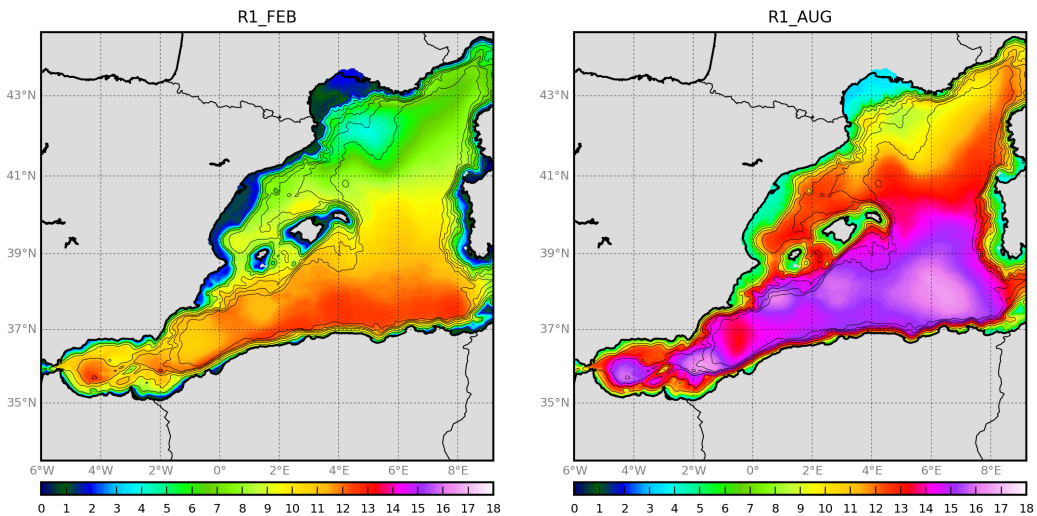


Figure 1.5: Regional characterization of the Rossby first radius of deformation, R_1 (km), in the western Mediterranean Sea for winter (February, left panel) and summer (August, right panel) obtained from the ROMSWMED32 simulation. Monthly averages are computed over the period 1995–2012. Black contours represent 250, 500, 1000, 1500, 2000 and 2500 m isobaths.

et al., 2016; Mason et al., 2019), with considerable success in the mesoscale range. Despite the significant advances in remote sensing and *in situ* observational resources, SMCs and their associated variability are still difficult to detect. Although some efforts have been made to this end, at the present time, the spatial and temporal resolution

required to explore the submesoscale can only be provided by models. Recently, numerics and infrastructure have evolved so that we can produce realistic representations of the WMed circulation at multiple scales, including multi-level nested configurations which provide insight into the connection between successive scales.

Several recent studies reveal a large occurrence of SMCs in the WMed in the uppermost layers to intermediate depths (Bosse et al., 2015; Bosse et al., 2016; Pascual et al., 2017; Troupin et al., 2019). At the bottom, understanding the role of the interaction of the mesoscale currents with topography in the generation of SMCs is still at early stages.

The Alboran Sea

Located in the westernmost region of the WMed, the Alboran Sea constitutes the transition area connecting the Mediterranean Sea with the Atlantic Ocean. This role entails significant implications on the dynamics in this area, promoted by the differing characteristics of the water masses at both sides of the region and by the different forcings to which they are exposed.

Bathymetry plays a determining role in steering the dynamics in the Alboran Sea. Steep slopes with deep canyons shape the north, south and west margins, with the latter connecting with the Atlantic Ocean through a narrow strait, while the eastern side offers a deep, wide open gate towards the Mediterranean Sea. The Alboran Ridge divides the basin in two deep bowls connected through the Alboran Trough in the northeast-to-southwest direction. Numerous seamounts complete this complex topographic scenario (Figure 1.6).

The main circulation of the Alboran Sea is driven by the incoming Atlantic Jet (AJ), a strong surface current composed of fresh AW with velocities up to 1 m s^{-1} . This jet feeds a quasi-permanent Western Anticyclonic Gyre (WAG) occupying the western half of the basin, and a less intense and more intermittent Eastern Anticyclonic Gyre (EAG) to the east (Viúdez et al., 1996; Vargas-Yáñez et al., 2002). In between these two main structures and also enabled by the shape of the basin, smaller cyclones along the northern and southern shores can also emerge (Heburn and La Violette, 1990; Peliz et al., 2013). The clash between the incoming AW with the resident Mediterranean water (MW) drives the generation of a strong density (mainly salinity) front, commonly named the Almeria-Oran (AO) front when it is located at the eastern edge of the EAG

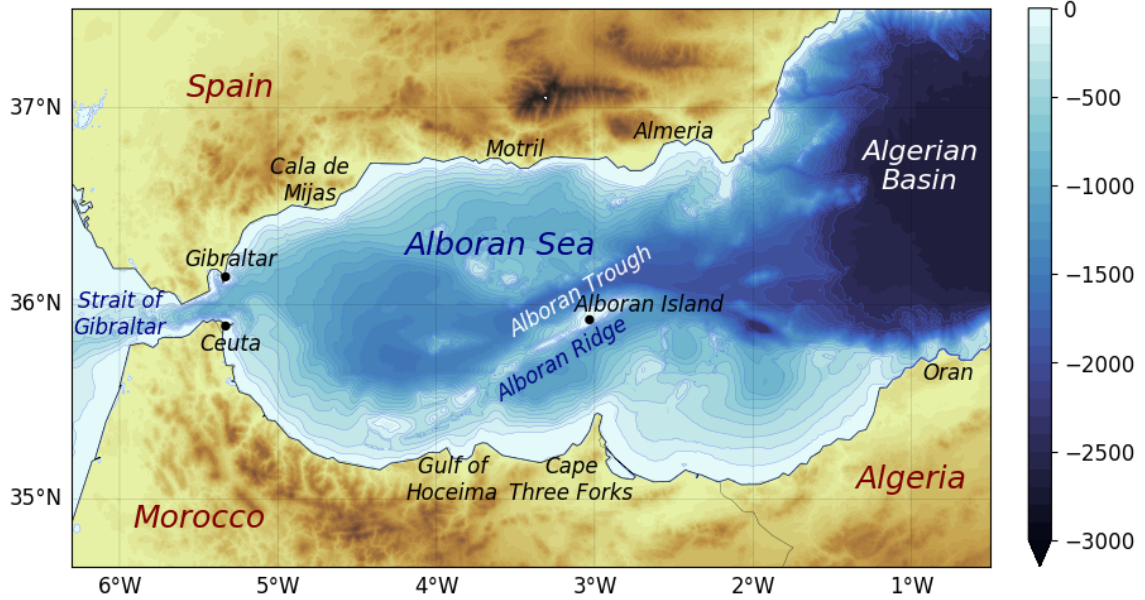


Figure 1.6: Alboran Sea, with locations of interest. Isobaths are contoured every 100 m.

(Tintoré et al., 1988; Allen et al., 2001).

The strong multiscale variability affecting the Alboran Sea dynamics starts at its western edge, where the SoG feeds the Mediterranean Sea basin with AW in the near-surface layer. The Mediterranean THC transforms this fresh water into saltier water, which leaves the basin back towards the Atlantic Ocean through the Strait in the near-bottom layers. This exchange flow, which can be coarsely described as a two layer system, is influenced by many processes at different timescales. Seasonal and interannual variability is promoted by the dynamical processes affecting the water masses at both sides of the Strait (Garrett et al., 1993; Candela, 2001; García Lafuente et al., 2007, 2009; Sánchez-Román et al., 2018) and, at smaller scales, the exchange can be affected by strong atmospheric pressure gradients between the Atlantic and the Mediterranean Sea or by the wind-induced currents (Menemenlis et al., 2007). Forced by the steep bathymetric configuration, these variations range between a maximal exchange regime, occurring when the flow is hydraulically controlled at the Camarinal Sill (CS) and Tarifa Narrows (TN), and a sub-maximal exchange, which is achieved when the TN control is suppressed (Figure 1.2; Garrett et al., 1990; Bryden and Kinder, 1991; Sannino et al., 2014). At the smallest scales, the most dominant processes are tidal currents (mainly the semidiurnal cycle) and internal waves (Ziegenbein, 1969; Vlasenko et al., 2009; Naranjo et al., 2014). The combination of tides with the topographic shape of the

SoG enforces the occurrence of a barotropic internal wave on the two-layer system, especially when the tidal currents flow over the CS (Ziegenbein, 1969; Sannino et al., 2014). This is commonly described as a tidal bore: an internal wave train propagating eastwards with an amplitude of around 100 m and 1 km wavelength (Sánchez Garrido et al., 2008). As it progresses towards the Mediterranean Sea, the tidal bore evolves into a packet of solitary internal waves, which interact with the complex bathymetric structure of the Alboran Sea and experience a combination of refraction, reflection, wave breaking and water mixing that leads to an intricate three-dimensional structure. The scales at which this phenomenon occurs overlaps with SMCs, and this must be taken into consideration when we attempt to identify SMCs from the vertical velocity field in our simulations.

Oscillations in the position of the AJ and the pre-existing circulation conditions in the Alboran basin promote fluctuations in the intensity and position of the WAG and, by extension, in the subsequent westward trajectory of the flow, which can either follow the path of the EAG or directly follow the African coast (Viúdez et al., 1998; Vargas-Yáñez et al., 2002; Renault et al., 2012). The presence of the one-gyre or two-gyre regime determines the intensity and position of the fronts generated in the region by the clash between the AJ and the resident water. Large vertical velocities have been found associated with these structures, especially at the northeastern edges of the gyres, where the currents and their associated fronts are more intense (Tintoré et al., 1988; Viúdez et al., 1996). The variability of the AJ not only affects the dynamical scenario in the Alboran Sea but also its biological productivity, promoting the onset of upwelling conditions in particular areas (*e.g.*, at the northwestern edge of the basin, aided by the presence of strong westerlies blowing from the Spanish coast) and increasing the primary production in these regions (Sarhan et al., 2000; Ruiz et al., 2001; Macias et al., 2016).

Although the physical oceanography in the Alboran Sea has been extensively explored and diagnosed at multiple scales, the sources of the large mesoscale variability are still not fully understood, and unraveling the roles of SMCs in this puzzling scenario is still an open issue.

Chapter 2

Model configuration and data

In this work we aim to develop a comprehensive strategy towards the detection and further analysis of submesoscale dynamics in the western Mediterranean Sea. First, an exhaustive mesoscale regional characterization of the energy conversion pathways between the mean and time-varying flow reveals the most active regions and the processes presumably responsible for maintaining the energy balance. Such processes will be subsequently assessed in the Alboran Sea, a very active, complex subregion in which motions below the mesoscale range are highly energetic and strongly influence the ocean circulation.

Ocean observations still remain too disperse in time and space, and available datasets cannot provide the level of duration, continuity and resolution required to achieve our objectives. Instead, recent advances in numerical modeling and computational resources allow performing realistic simulations at multiple scales, long enough to allow reliable statistics and with sufficient resolution to investigate the processes governing submesoscale dynamics.

At this point, we base our study on a set of simulations implemented with the Regional Ocean Modeling System (ROMS), widely used by the scientific community to perform regional realistic simulations. Its core structure and multiple customer-specific configuration possibilities make it most suitable for the purpose of our research (Shchepetkin and McWilliams, 2005, 2009b).

The different parts of our analysis strategy require specific model datasets adapted to each research subject. First, the LEC analysis demands a long simulation in order to reach a statistically stationary ocean state, and the resolution needed to perform such

an analysis should resolve the WMed dynamics in the mesoscale range. On the other hand, high resolution data in both time and space is a basic requirement for an effective exploration of the processes involved in the transition towards the submesoscale.

For this reason, the datasets that we use for each phase of the study have been obtained from two different ROMS configurations:

1. For the LEC analysis in Chapter 3, we use a pre-existing long mesoscale simulation (ROMSWMED32, developed by Escudier, 2015) which enables an accurate statistical analysis of the energy conversion routes in the western Mediterranean region.
2. The transition from mesoscale to submesoscale dynamics is assessed from a set of two nested, realistic simulations specifically developed for this work, with increasing horizontal resolutions ranging from 1.5 km for the parent grid (broadly covering the whole WMed region) to 0.5 km for the nested child. As will be detailed in the next sections, this nested approach has been designed to explicitly resolve dynamical processes over the full water column. This is achieved with a careful selection of model parameterizations, realistic external forcings and introducing enough vertical resolution, especially in the key surface and bottom layers. Because high resolution modeling is much more demanding in terms of computational time and storage capacity, the domain of the finer solution spans only over a selected subregion of the area explored in the LEC study: the Alboran Sea.

2.1 The ROMS model

ROMS is a split-explicit, 3D free-surface ocean model which solves the primitive equations for momentum, temperature and salinity using the Boussinesq approximation and hydrostatic vertical momentum balance (Shchepetkin and McWilliams, 2005). A multiple-time-level time stepping allows solving both barotropic and baroclinic dynamics at appropriate time intervals: free surface and barotropic momentum equations are advanced using a shorter time step than the tracers (temperature and salinity) and baroclinic momentum equations. The complete time stepping algorithm is described in Shchepetkin and McWilliams (2005, 2009b).

The model is discretized in terrain-following curvilinear σ -coordinates. Their major advantage against z-coordinates is that they can provide a better representation of flow-topography interactions and shelf dynamics in domains with complex bathymetry. In contrast, they entail two principal constraints: (1) the emergence of spurious diapycnal mixing, introduced by high-order diffusive advection schemes, and (2) pressure gradient errors (PGE). The former (1) is strongly reduced by applying a split version of the upstream third-order default advection scheme (known as TS_HADV_SUP3). This version, TS_HADV_RSUP3, is highly recommended in realistic applications to preserve water masses (Marchesiello et al., 2009; Lemarié et al., 2012a,b). It splits the UP3 scheme into a 4th-order centered advection and a rotated biharmonic diffusion with grid-dependent diffusivity satisfying the Peclet constraint (*i.e.*, the ratio of advection to diffusion must be lower than 2). However, TS_HADV_RSUP3 is expensive in terms of computational cost. Regarding (2), some smoothing is applied to realistic topography to prevent PGE: the slope of the σ -layers is controlled by the parameter $r = \nabla H / 2H$, where H is the sea floor depth. Empirical results have shown that errors are significantly reduced if r does not exceed 0.2. Another prevention tool is activating the SPLIT_EOS option, which splits the nonlinear equation of state into adiabatic and compressible parts for PGE reduction (Shchepetkin and McWilliams, 2003).

Horizontal advection is parameterized using the above mentioned split version of the upstream third-order advection scheme (TS_HADV_RSUP3), which allows the generation of steep gradients and is weakly dispersive and diffusive. Vertical advection of momentum is based on an algorithm which combines a high-order explicit scheme with an implicit one which mitigates vertical Courant-Friedrichs-Lowy (CFL) restriction and avoids numerical instabilities (Shchepetkin, 2015). For vertical advection of tracers we use a fourth order Akima scheme.

Because boundary layers are characterized by strong turbulent mixing, parameterization of vertical mixing of momentum and tracers is based on the nonlocal, K-profile parameterization (KPP) scheme by Large-McWilliams-Doney (LMD; Large et al., 1994). Under such a profile, the respective mixing coefficients reach maximum values in the interior of the surface (mixed) and bottom boundary layers, decreasing to minima within the intermediate depths.

All simulations were run in parallel on High Performance Computing (HPC) clusters using the Message Passing Interface (MPI). This option speeds up the simulations taking advantage of the power of all the processors and the available cluster memory.

Specific details for each of the ROMS configurations used in this study, such as the grid design, temporal discretization, topography, forcings or initial and boundary conditions are given in the next sections. A summary is provided in Table 2.1.

	ROMSWMED32	WMed1500	Alb500
ROMS version	ROMS-AGRIF 3.0	CROCO 1.0	CROCO 1.0
Horizontal grid	1/32° (3.5 km)	1/75° (1.5 km)	1/225° (500 m)
Vertical σ -levels (θ_s , θ_b)	32 (6.5, 1.5)	60 (7, 5)	70 (7, 5)
Boundary/Initial conditions	NEMOMED12	Mercator Global	WMed1500
Atmospheric forcing (period)	NCEP-CFSR (6-hourly)	NCEP-CFSR (1-hourly)	NCEP-CFSR (1-hourly)
Tidal forcing	No	No	OSU-TPX07
Topography	Smith and Sandwell (1997) & (Sanz, 1991)	SRTM30_PLUS_V11	SRTM30_PLUS_V11
Bottom drag (coefficient)	Linear (0,0003 m s ⁻¹)	Quadratic (von-Karman log-law)	Quadratic (von-Karman log-law)
Baroclinic Δt	240 s	200 s	27 s
Barotropic Δt	10 s	2 s	0.27 s
Period	1992-2012	2010-2013	2010-2013
Outputs	daily	daily	3-hourly

Table 2.1: Principal characteristics of the different ROMS configurations used in this study. θ_s , θ_b denote the stretching parameters at surface and bottom, respectively, and Δt refers to time-step.

2.1.1 The ROMSWMED32 simulation

As a first step, this study intends to provide an estimate of the Lorenz energy cycle in the WMed using a realistic ROMS simulation at mesoscale resolution. Because the LEC formulation is based on the analysis of a stationary ocean state, a principal model requirement is that the solution ensures reliable statistics, which can be achieved by running the model over a sufficiently long period. On the other hand, a realistic mesoscale characterization demands a reasonable grid size, enforced by the small Rossby deformation radius in the WMed region.

We found a suitable candidate in the ROMSWMED32 solution, developed in a previous work by Escudier (2015). This is a 20-year simulation implemented in the WMed region using ROMS in its AGRIF 3.0 version (Debreu et al., 2008). With this integration period, the condition of statistical stationarity is broadly satisfied.

This simulation also provides enough spatial resolution to resolve mesoscale dynamics in the area. The domain covers the western Mediterranean basin between $7.4^{\circ}\text{W} - 10^{\circ}\text{E}$ and $34.6^{\circ} - 44.7^{\circ}\text{N}$, spanning from the Gulf of Cadiz to Corsica and Sardinia with a horizontal grid resolution of $1/32^{\circ}$, about 3.5 km (Figure 2.1). The vertical grid is composed of 32 σ -levels using the vertical stretching function defined in Shchepetkin and McWilliams (2009b) with stretching parameters $\theta_s = 6.5$ and $\theta_b = 1.5$ at surface and bottom respectively, and a critical depth $h_c = 250$ m, which implies upper level sizes ranging from 2 to 7.5 m and from 4 to 280 m at the bottom. Bathymetry

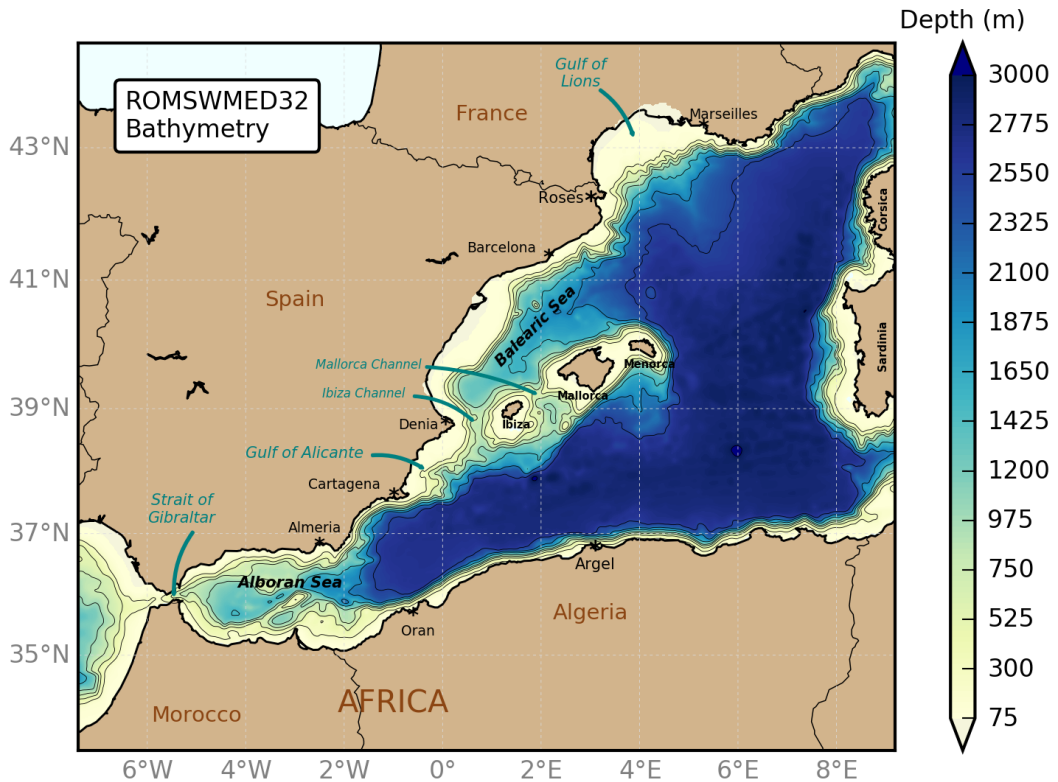


Figure 2.1: ROMSWMED32 simulation domain, bathymetry (colorbar) and locations of interest. Black contours represent 250, 500, 750, 1000, 1500, 2000, 2500 and 3000 m isobaths.

was obtained by combining the one developed by Smith and Sandwell (1997) with a more detailed representation for the Gibraltar region (Sanz, 1991).

A realistic initial state of the ocean interior and boundary conditions were derived using a NEMOMED12 55-year simulation over the period 1958–2013 covering the entire Mediterranean at $1/12^{\circ}$ resolution (about 9.25 km). The atmospheric forcing was obtained from the National Centers for Environmental Prediction (NCEP) Climate

Forecast System Reanalysis (CFSR) data set, with a 35 km spatial resolution and a time step of 6 hours, using a bulk formulation for fluxes. The model was run freely without data assimilation.

The reader is referred to Escudier (2015) for a full description of the model configuration and an exhaustive validation. We summarize some aspects from this validation in Appendix C (“Some validation aspects”), as we consider they can be relevant for the energy analysis.

The simulation spans from 1992 to 2012, although the dataset used in our analysis starts in 1995 for statistical stability confidence (see Section 3.1). Nearly two decades of daily averaged outputs enable reliable statistics for the prognostic variables and, together with the adequate spatial resolution, ensure an appropriate characterization of the mesoscale dynamics of the area.

2.1.2 WMed1500 and Alb500 nested simulations

Submesoscale processes in the Alboran Sea develop at relatively short time scales (from hours to several days or weeks) and extend over small spatial domains (from tens or hundreds of meters to a few kilometers). A model solution capable of simulating such dynamics must meet two principal conditions: (1) that the configuration be as realistic as possible (this implies the use of realistic atmospheric forcing, a suitable grid resolution, and an accurate selection of the model parameterizations), and (2) that it provides all the necessary fields at a resolution large enough to capture the submesoscale.

With this aim, we ran two realistic simulations using a one-way, off-line nesting procedure with increasing resolution using CROCO, a new oceanic modeling system built upon ROMS_AGRIF, with a numerical kernel close to the UCLA version of the ROMS model (Shchepetkin and McWilliams, 2009a, <http://www.croc-ocean.org>). In this nesting approach, the parent, coarser simulation provides initial and boundary conditions to the finer child, while there is no feedback in reverse (Marchesiello et al., 2001; Penven et al., 2006; Mason et al., 2010).

The parent solution (WMed1500) covers the Western Mediterranean Sea and part of the Atlantic Ocean, with a horizontal resolution of $\Delta x \approx 1.5$ km (Figure 2.2, top). It is discretized with 60 σ -levels in the vertical, with stretching parameters $\theta_s = 7$ and

$\theta_b = 5$ at surface and bottom, respectively, and a critical depth $h_c = 300$ m.

For the child simulation (Alb500), covering the Alboran Sea region, we apply a nesting refinement factor of 1:3 achieving a horizontal resolution of 500 m (Fig.2.2, bottom). The vertical discretization uses the same stretching parameters as WMed1500 and is increased to 70 σ -levels, which implies layer thicknesses ranging from 15 cm to 4 m at the surface and from 15 cm to 15 m at the bottom. This provides sufficient resolution to resolve submesoscale dynamics, with particular focus on those processes involving the surface and bottom layers (*e.g.*, frontogenesis and flow-topography interaction).

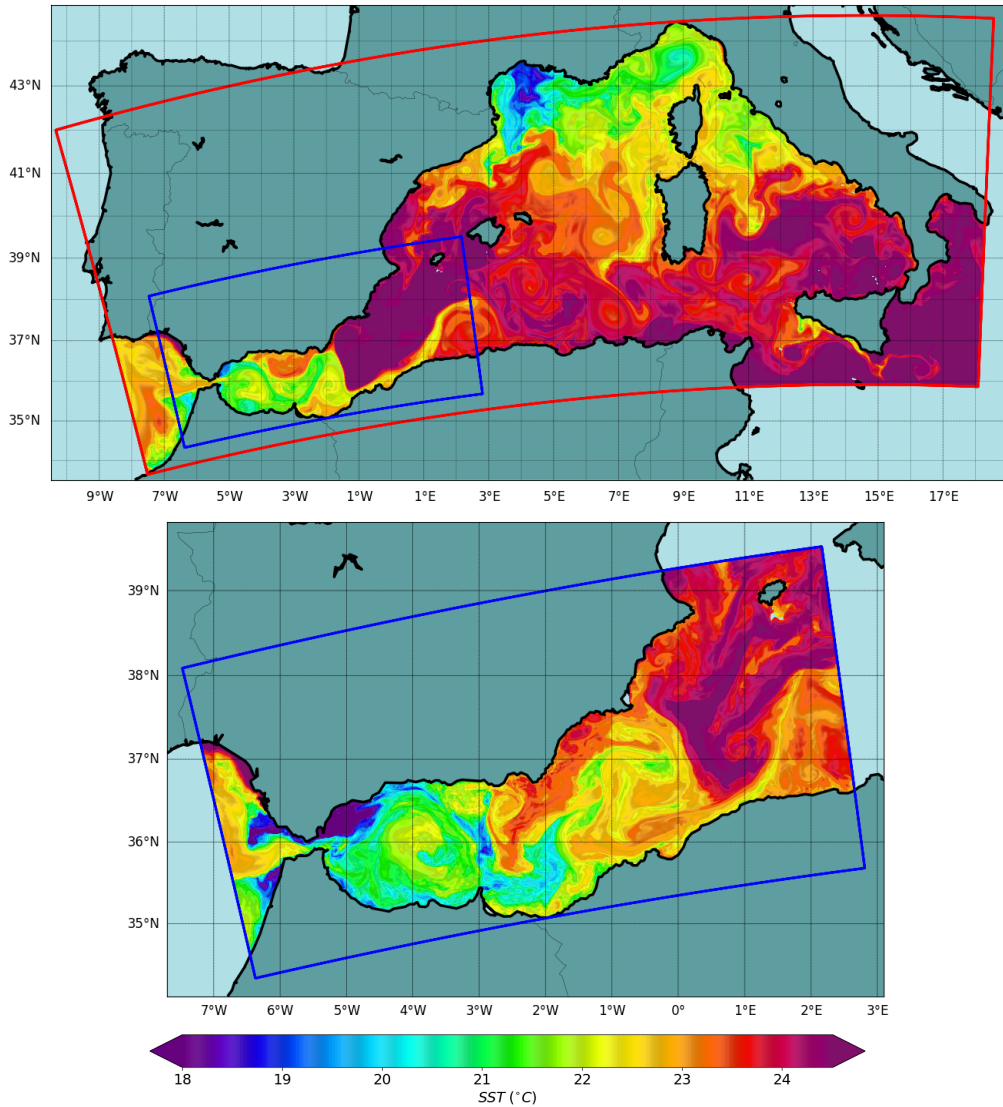


Figure 2.2: SST snapshots from the WMed1500 (top) and the Alb500 (bottom) solutions showing their corresponding spatial domains. Data corresponds to September 25, 2013 in both figures.

Bottom stress in both simulations is parameterized using the quadratic law $\tau = \rho_0 C_D \|\mathbf{u}_b\| \mathbf{u}_b$, where ρ_0 is the reference density, \mathbf{u}_b is the horizontal velocity in the bottom layer and C_D is a drag coefficient. We use the von Karman logarithmic formulation for $C_D = [\kappa / \log(\Delta z_b / z_r)]^2$, where $\kappa = 0.41$ is the von Karman constant, Δz_b is the thickness of the bottom layer and z_r the roughness scale, set to 0.1 cm.

Atmospheric forcing is derived from the NCEP-CFSR data set at hourly time steps (versions *ds093.1* and *ds094.1*) and with spatial resolutions ranging from 0.2° to 0.5° (20 to 50 km approx.) depending on the variable, using a bulk formulation for fluxes. The use of realistic atmospheric forcing translates into a more realistic representation of the dynamics in the WMed. In this regard, even though it may seem paradoxical, it is essential that no data is assimilated during the integration of the simulation: while data assimilation makes a model solution converge towards the real state of the ocean, this method entails a continued input of renewed initial conditions into the model equations, and their subsequent numerical readjustments, thus interrupting the continuous, natural evolution of the dynamical equations that describe the physical processes which we intend to identify.

Alb500 is also forced at the boundaries with tides (barotropic currents and surface elevation). Tidal forcing is interpolated from the OSU-TOPEX/Poseidon Global Inverse solution database (version TPX0.7), using 10 tidal constituents.

Bathymetry is obtained from the SRTM30_PLUS_V11 global dataset (Becker et al., 2009). In the child solution, the Atlantic section is strongly affected by tidal forcing and, together with the steep bathymetric slopes in the Strait of Gibraltar, spurious pressure gradients can develop inducing model blow ups. To prevent these, we apply additional smoothing in the Atlantic side for the child grid using a smoothing radius corresponding to 8 grid points (4 km halfwidth) to prevent numerical instabilities during the model run. A transition area of 50 grid points leads to a finer Mediterranean Sea bathymetry, where the smoothing radius is set to 4 grid points.

Realistic initial and boundary conditions for the parent WMed1500 solution were interpolated from the Mercator Global Ocean forecasting system (Lelloche et al., 2018) which provides a realistic representation of the dynamics in the WMed (and the Alboran Sea, in particular) in the mesoscale range (Mason et al., 2019). This model has a $1/12^\circ$ (about 9.25 km) horizontal resolution and 50 z -levels in the vertical, ranging from 0 to 5500 m, and a temporal coverage starting in 2006 to the present.

The product feeds WMed1500 with daily mean two-dimensional fields of temperature, salinity and currents, and sea level height. Following the nesting procedure described in Mason et al. (2010), WMed1500 provides the initial state and boundary conditions for the implementation of Alb500.

Time-stepping for the baroclinic momentum equations and tracers in the WMed1500 configuration was set to 200 s, with 100 barotropic time steps within each 3D step. Finding the optimal baroclinic time step for the Alb500 solution was a trickier task. The main complication in finding an optimal time-stepping that respects the vertical CFL condition comes from the fact that increasing grid resolution means a less smoothed topography, leading to unrealistic larger vertical velocities near the bottom (Shchepetkin, 2015). The steep, complex bathymetry along the Strait of Gibraltar, together with the effect of tides, led to numerous model blow-ups during the testing phase of the model. The baroclinic time step was finally set to 27 s, and to 0.27 s for the barotropic mode.

WMed1500 was integrated over 4 years (2010–2013). Variables were stored once per day as daily averages, while instantaneous fields were saved once per month. Alb500 spans the same period and output variables were stored 8 times every day as 3-hourly averages, while instantaneous fields were recorded once per day.

Computational resources

WMed1500 was run at FONER, a computing cluster at the Universitat de les Illes Balears (UIB). The run required 140 cores and was completed in 10 days. The outputs size (four years of daily averages plus one restart file per month) is around 700 GB.

The integration of the Alb500 solution was performed at TRUENO, a computing cluster owned by the Spanish Research Council (CSIC) in Madrid. The integration of 4 model years required nearly 4 months, at a mean output rate of 13 model days per running day. This was due to the large grid resolution and to the complexity of the dynamics at the Strait of Gibraltar, which forced a dramatic reduction of the model time stepping to avoid model blow ups in this region. Outputs, composed of four years of 3-hourly averages plus one restart file per day, require a storage capacity of 7.1 TB.

Model spin up

In order to determine the time needed for the simulations to stabilize, we compute time series of surface kinetic energy averaged over the whole domain for both solutions.

In WMed1500, surface KE reaches its maximum about 3 months after the model is initialized (Figure 2.3, top). Then it starts fluctuating, showing a seasonal cycle along the running period with energy maxima in winter, decreasing towards minimum values at the beginning of the fall season. We can therefore consider a spin up period of three months for the parent simulation.

Alb500 is implemented over the same period (Fig.2.3, bottom), along which surface KE displays a seasonal variability similar to WMed1500, but with larger amplitudes per unit area presumably due to the reduced domain of the finer grid. For reliability, we choose a reasonable spin up period of one year for the child simulation.

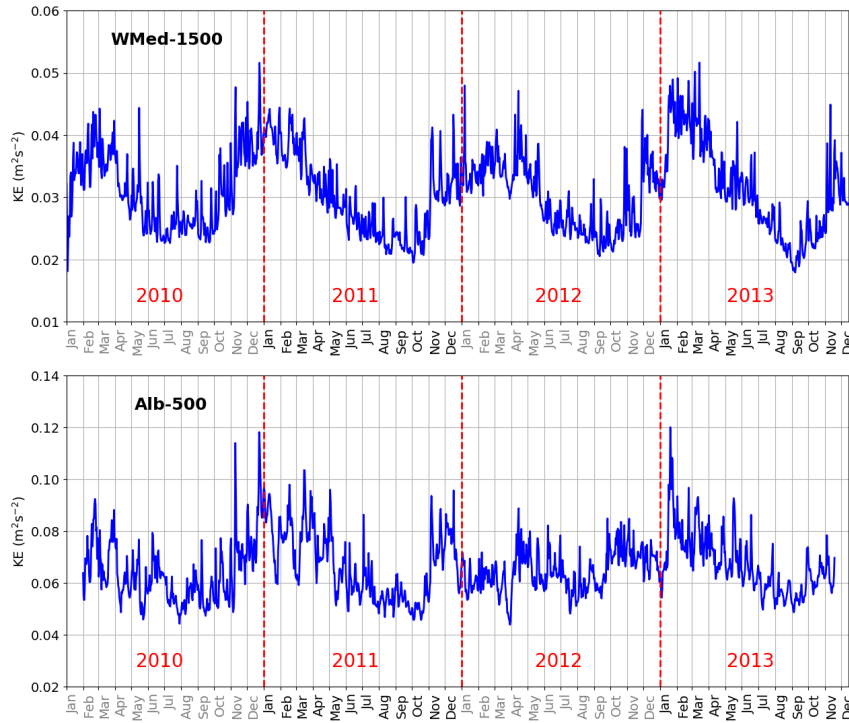


Figure 2.3: Time series of daily mean surface KE from the WMed1500 (top) and the Alb500 (bottom) solutions spatially averaged over the full respective domains.

Considering a reduced domain over the Alboran Sea region, Fig.2.4 compares surface KE from both models averaged over the same domain, displaying similar ranges and variability.

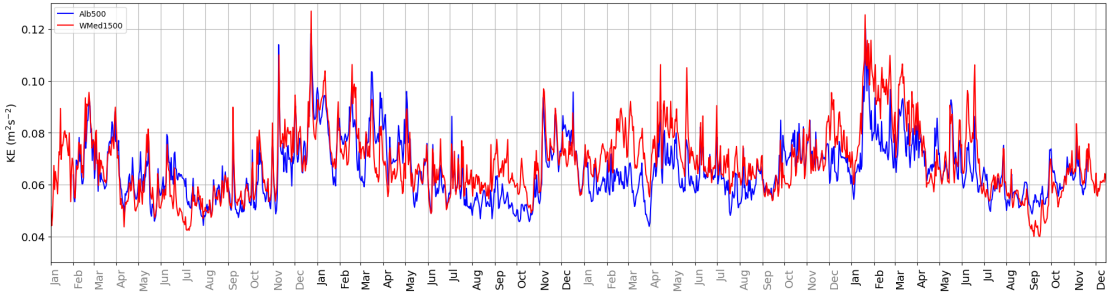


Figure 2.4: Time series of daily averaged surface KE from the WMed1500 (red) and the Alb500 (blue) solutions spatially averaged over a reduced domain covering the Alboran Sea region.

Model validation

Even though our nested simulations do not attempt to reflect the instant real state of the ocean, some validation is needed in order to show that they are representative of the Alboran Sea dynamics with some confidence.

At the largest scale, surface mesoscale circulation from the WMed1500 solution is compared with AVISO products for the Alboran Sea. Figure 2.5 shows the surface KE averaged over year 2013 from WMed1500 (top), and the corresponding AVISO mean KE pattern for the same period (bottom). Daily fields from WMed1500 are smoothed with a Gaussian kernel of 13 km halfwidth to match the AVISO spatial resolution. Despite the filtering, larger values are obtained in the modeled pattern, as expected from its higher resolution, on the one hand, and also because modeled KE is computed from the total velocity components, while AVISO KE is obtained from the geostrophic velocity derived from the sea surface height (SSH) field. Even though both maps show similarities in the position and shape of the WAG, the mean spatial characterization from AVISO more closely reflects a double-gyre configuration, while in the WMed1500 figure the signature of the EAG is much weaker, with the Atlantic residual inflow preferably flowing along the African coast. A more detailed analysis from monthly averages reflects in both cases the stability of the WAG against the large KE variability along the eastern half of the basin (Figure 2.6).

To evaluate the effect of tidal forcing in the child solution, time series of SSH at several sampling points were compared to the time series from the nearest tide gauge. Hourly datasets for the tide gauges were obtained from the Instituto Español de Oceanografía (IEO) and 3-hourly averaged to compare them with the model outputs.

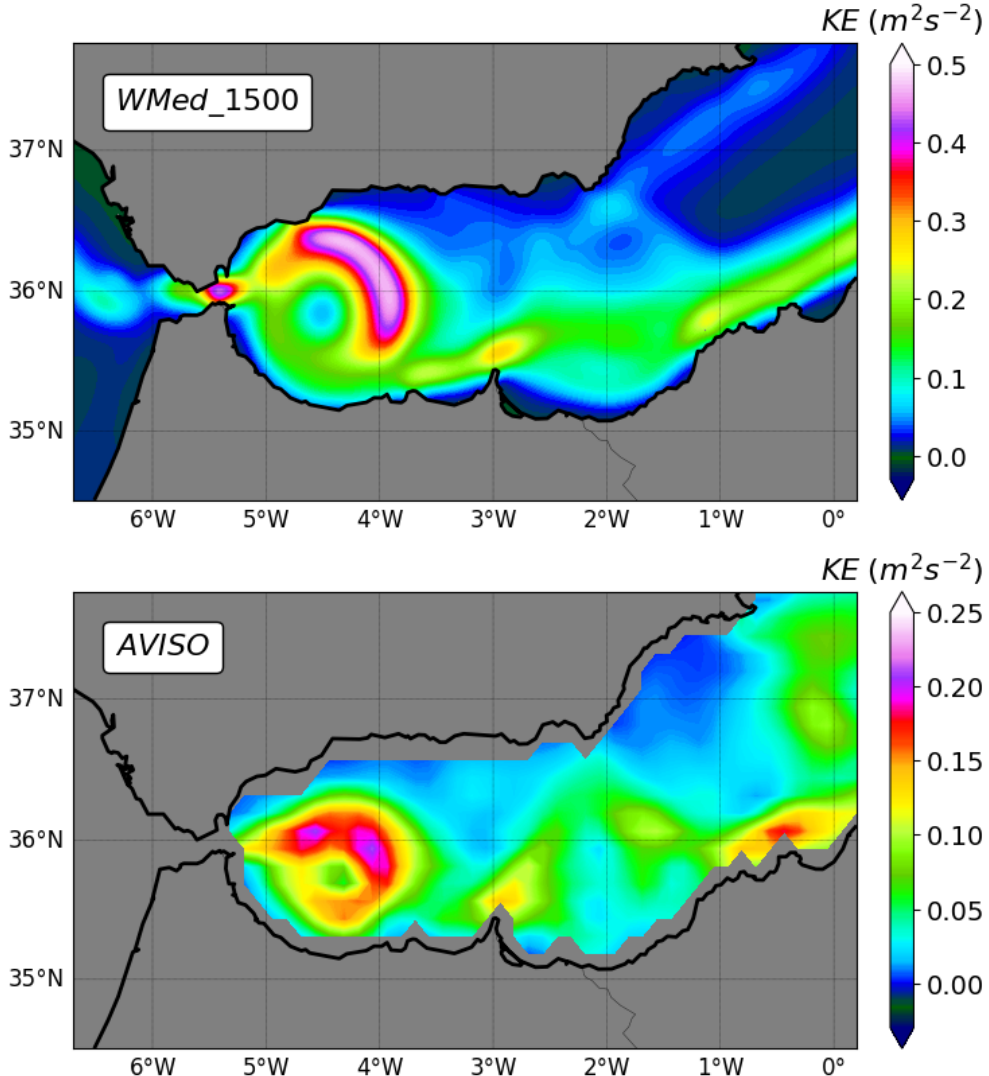


Figure 2.5: Mean KE over year 2013 from the WMed1500 solution, obtained from daily velocity fields smoothed with a Gaussian kernel of 13 km halfwidth (top) and geostrophic KE for the same period obtained from AVISO SSH data (bottom).

Figure 2.7 shows a subset of the modeled SSH time series (black) at a point located near the Atlantic boundary of the Alb500 domain, compared to the values recorded by the nearest tide gauge (red). As observed, the model reproduces the tidal oscillations accurately, and the slight differences in amplitude lie within reasonable ranges.

Water exchange through the Strait of Gibraltar was computed from both parent and child simulations over the last two years of available data. Time series of daily averaged net transports show similar values in both simulations (Figure 2.8, bottom panel). When considering inflow/outflow transports separately, high variability (mainly

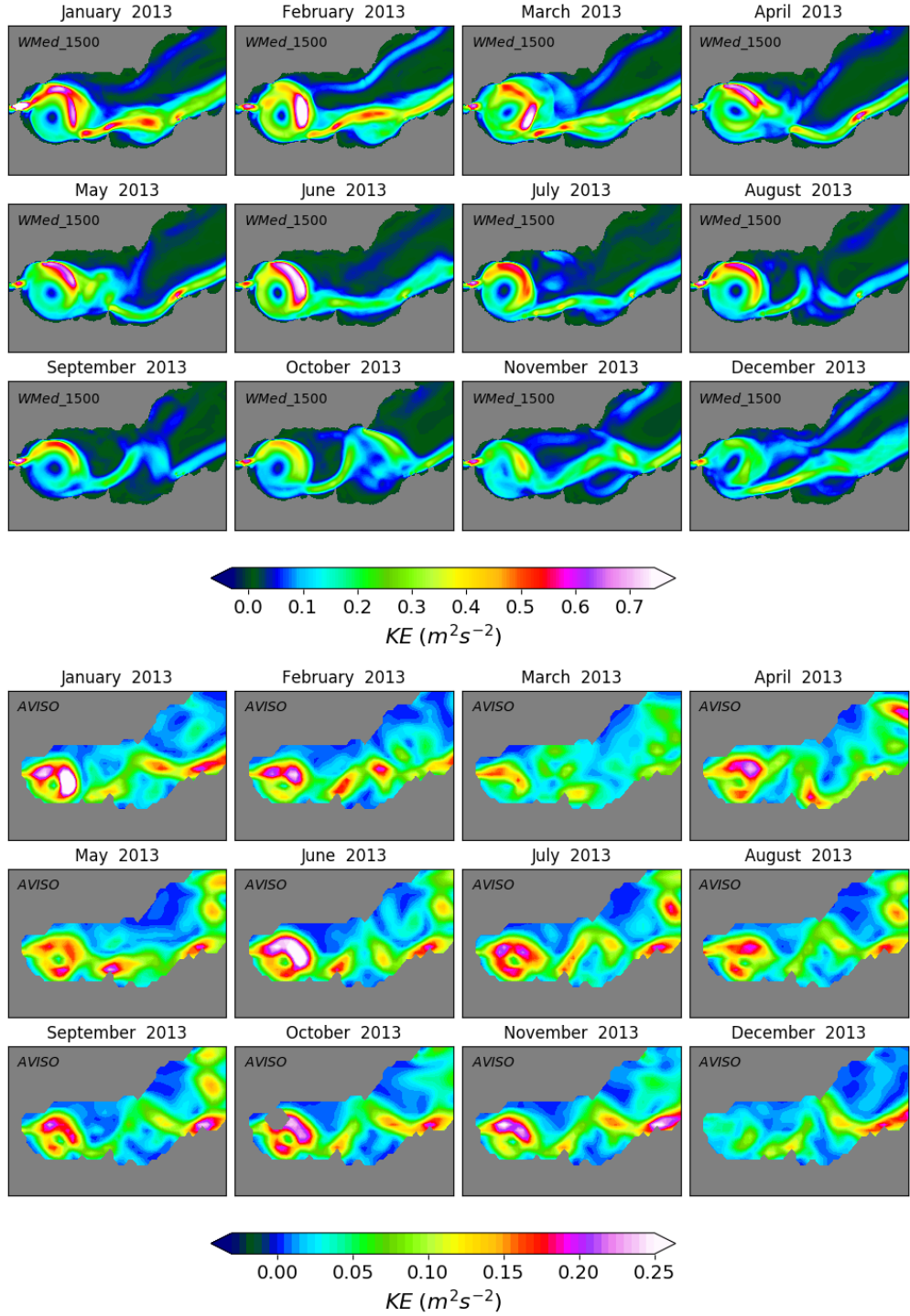


Figure 2.6: Monthly averaged KE fields for year 2013 from the WMed1500 solution, obtained from non-smoothed daily velocity fields (top) and geostrophic KE for the same period from AVISO SSH data (bottom).

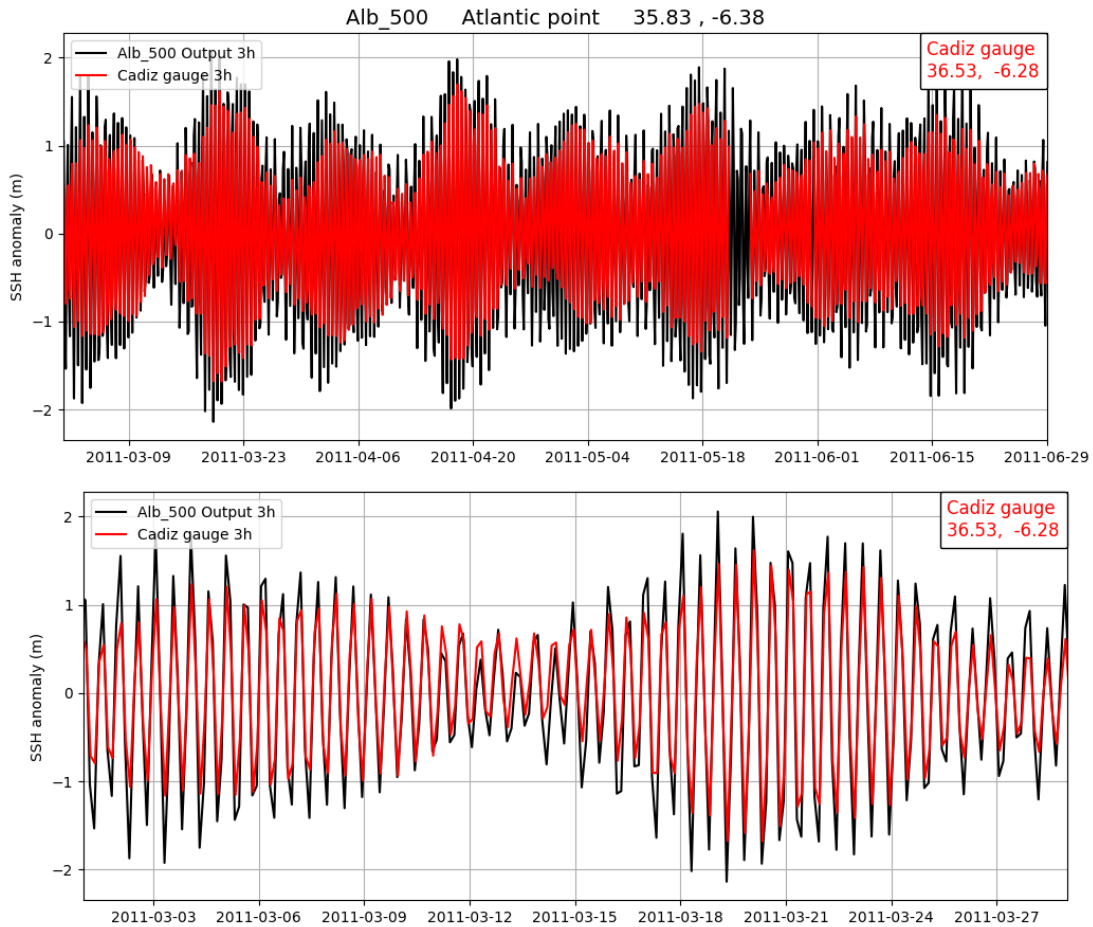


Figure 2.7: Top: time series of 3-hourly averaged SSH from Alb500 at a point located near the Atlantic boundary of the domain (black), compared to the values recorded by nearest tide gauge, Cadiz (red). The data spans the period March-June 2011. Bottom: a subset corresponding to the first month from the upper panel (March 2011).

in amplitude) is displayed in the Alb500 solution, probably due to a combination of higher model resolution and the effect of tidal-induced oscillations in the transports on both directions.

While modeled values ranges are consistent with available estimates from different authors (Sánchez-Román et al., 2009; Soto-Navarro et al., 2010), the time-mean net transports obtained from our simulations are negative: Alb500 gives -0.15 Sv ($+0.43$ inflow, -0.59 Sv outflow), and WMed1500 gives -0.18 Sv ($+0.77$ inflow, -0.95 outflow), in contrast to the slightly positive observed values (around $+0.05$ Sv). Possible reasons for these differences are discussed in section 2.2. However, a realistic representation of the Strait of Gibraltar dynamics and the multi-scale variability of the water

exchange requires long term and high-resolution simulations specifically designed for that purpose, far beyond the scope of this Thesis.

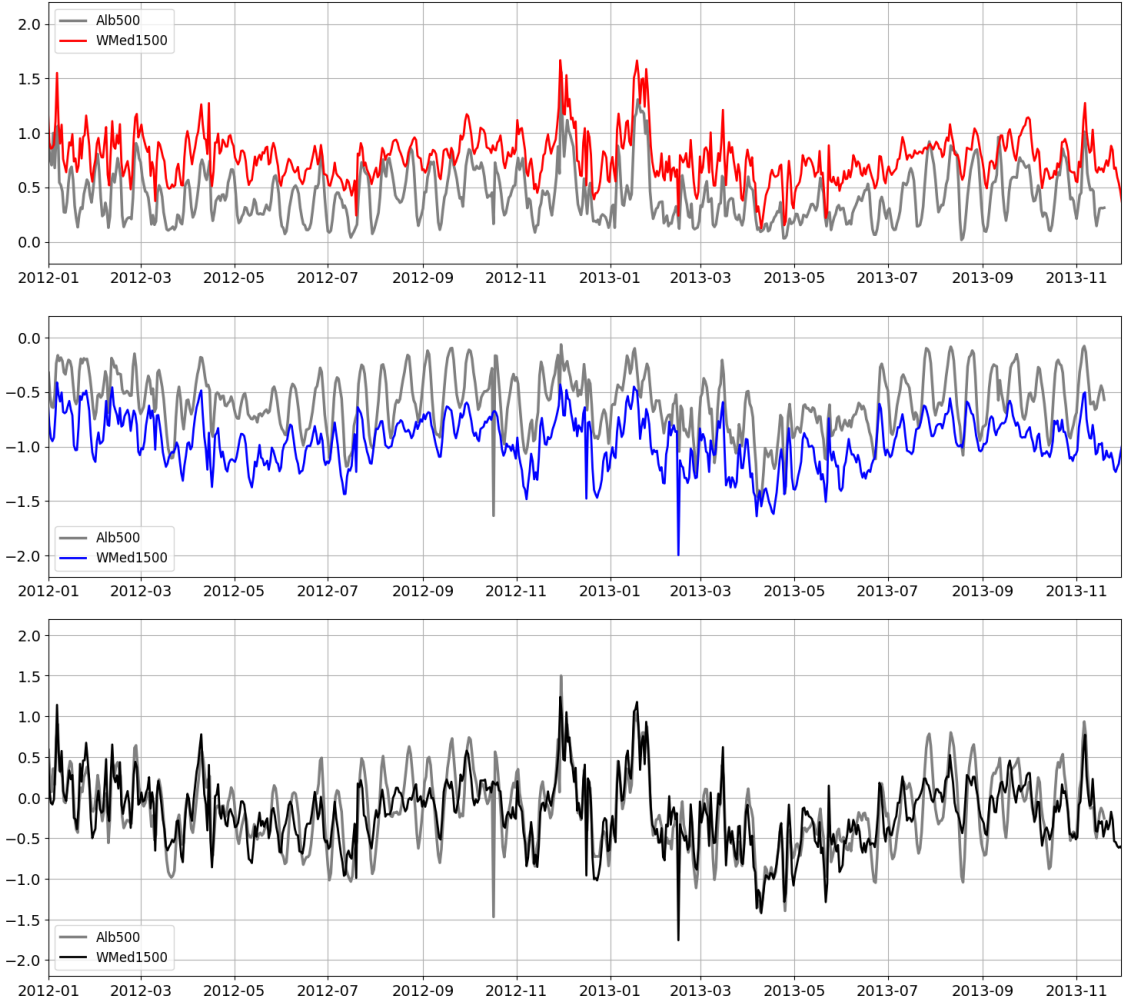


Figure 2.8: Time series (2012–2013) of daily averaged transports (inflow, outflow and net, from top to bottom) across the Strait of Gibraltar from WMed1500 and Alb500 solutions. Volume fluxes are computed across a section located near the Camarinal Sill (around 5.75°W).

2.2 Discussion

Two different simulations developed with the ROMS model provide specific datasets suitable for the different objectives of this study. First, a pre-existing long mesoscale simulation, ROMSWMED32, developed by Escudier (2015) ensures reliable statistics to perform an estimate of the Lorenz energy cycle in the WMed. On the other hand,

exploring the submesoscale in Alboran Sea demands much larger resolution in both time and space, together with a specific model configuration specially designed to resolve those processes in such a complex region. This is achieved by means of a set of two nested, realistic simulations specifically developed for this work, with successively finer resolutions ranging from 1.5 km for the parent grid (WMed1500) to 0.5 km for the nested child (Alb500). These simulations have been implemented using CROCO, the new modeling system built upon ROMS_AGRIF.

In addressing the transition towards the submesoscale, the principal adjustments incorporated into the new set of CROCO nested configurations, in relation to the mesoscale-resolving ROMSWMED32 solution, include: (1) enhancement of the grid resolution by using an improved topography dataset and performing a finer vertical discretization which better resolves the surface and bottom layers, given their major role in the submesoscale processes in which we are currently interested; (2) improved model parameterizations, *e.g.*, the use of a quadratic formulation for the bottom drag against a linear coefficient; and (3) introducing more realistic external forcing by incorporating tides into the finest solution. Furthermore, the data averaging/storing rates (3-hourly averages in the finest solution) allow the detection of small scale processes (*e.g.*, tides, internal waves, transient eddies, downwelling events in frontal processes, etc.) which are most probably overlooked with shorter recording frequencies.

Some validation was performed in order to asses the reliability of our simulations to reproduce the Alboran Sea dynamics. Surface mesoscale circulation patterns from the WMed1500 solution are consistent with those derived with AVISO SSH products for the Mediterranean Sea. In this regard, even though the values of the modeled variables lie in the observed ranges, instantaneous model fields and their variability patterns do not necessarily reproduce the observations. This is mainly because no data is assimilated during the integration of our simulations, so that the dynamical equations can freely evolve. A faithful representation of Alboran Sea dynamics involves a realistic depiction of the water transports through the Strait of Gibraltar. Modeling the Strait's dynamics demands an accurate, particular model configuration specifically designed for that purpose (Baschek et al., 2001; Peliz et al., 2013; Sannino et al., 2014). For example, the observed positive net transport towards Alboran Sea is the result of an excess of evaporation against fresh water inflow in the Mediterranean basin, which must be compensated by a net water input from the Atlantic Ocean through the Strait. In ROMS, evaporation translates into an increase of salinity, while

water volume doesn't change. If needed, this water deficit between the Atlantic and the WMed must be further (manually) added to the model configuration. This can be implemented in the form of specific volume conservation conditions, for example, as done in Peliz et al. (2013). Another constraint comes from the method used for estimating the transports in both directions, which depends on many factors: the location of the section crossing the Strait (Spartel Sill, Camarinal Sill, Tarifa Narrows, etc.), the definition of the interface between Atlantic inflow and Mediterranean outflow (a zero velocity layer, an isohaline or a combination of both), or whether tidal forcing is considered (Sannino et al., 2014). Besides the limitations of our model in providing an exhaustive reproduction of the Strait's dynamics, which goes beyond the scope of this Thesis, the transports obtained from our set of simulations show reasonable behavior for both Atlantic inflow and Mediterranean outflow.

The model requirements to perform the submesoscale inquiry in the Alboran Sea involve certain constraints to the analysis capabilities of our set of CROCO nested solutions. The completion of suitable simulations was achieved at the expense of a large computational cost in terms of running time and storage capacity. This involves relatively short integration periods for the solutions (3 years) and the "short" length of the simulations (in addition to the use of realistic rather than climatological atmospheric forcing; Marchesiello et al., 2003; Mason et al., 2011) reduces the possibility of achieving a stationary state of the ocean from the evolution of the model itself. Hence, analysis based on statistical diagnosis of the full solution must be handled and interpreted with care (*e.g.*, the mean characterization of the ocean submesoscale dynamics and processes, their seasonal and interannual variability, etc.). Nevertheless, our submesoscale research does not aim for a general overall survey, but rather a more specific exploration of the dominant dynamical processes.

In conclusion, our set of nested model solutions constitute an effective tool to investigate ocean dynamics in the Alboran Sea. It provides a starting point for the development of a comprehensive strategy for the analysis of submesoscale processes in this area, which can be also extrapolated to other regions in the Mediterranean Sea.

Chapter 3

The Lorenz energy cycle: estimation of the energy conversion routes in the western Mediterranean Sea.

The goal of this study is to estimate the LEC in the WMed from the ROM-SWMED32 solution presented in Chapter 2 and use it to identify the physical mechanisms responsible for maintaining the energy balance (Marchesiello et al., 2003; Sorgente et al., 2011; Renault et al., 2016; Wu et al., 2017).

The terms and formulations required to perform our energy analysis are summarized below. First, Section 3.1 introduces simplified formulations for the mean kinetic energy (MKE) and eddy kinetic energy (EKE), and for the mean available potential energy (MAPE) and eddy available potential energy (EAPE). The Lorenz energy cycle is presented and its application to ocean dynamics is considered and discussed. Derivation of the energy balance equations involved in the LEC formulation is summarized, and the terms responsible for EKE production are identified for further analysis. Results are presented in Section 3.2, where the seasonal and regional characterization of the mean (mesoscale) circulation is supported by the analysis of EKE variability, and an estimate of the LEC and the spatial distribution of the conversion rates among different forms of energy is assessed in three subregions of the domain. The results are summarized and discussed in Section 3.3.

3.1 Energy analysis

Energy analysis is based on the concepts of mean and eddy flow KE and PE budgets. Here, mean flow is defined as the local time average over the 18-year period of the model solution (see Appendix C, “Assessment of statistical equilibrium and model spin-up”), while the term *eddy* refers to the deviation from the long-term mean. This definition of eddy includes many sources of variability within a wide spectrum of scales, from the small scale fluctuations emerging from local dynamics, to the long-term tendencies arising from the non-stationary atmospheric and boundary forcings. However, this formulation is statistically consistent for the derivation of the energy balance equations and suitable for the study of the eddy-mean flow interaction.

3.1.1 Kinetic energy and available potential energy

According to the theory of random processes for turbulent flows, we assume the flow to be statistically stationary (Pope, 2001). In this regard, after the model has been initialized, the flow field passes through a transient spin up period until it reaches a statistically stationary state. This means that while the prognostic variables vary in time, their statistics (mean and variance) are time independent. Under such assumptions, the components of the flow field $\mathbf{u}(t)$ can be written as the sum of their temporal mean $\bar{\mathbf{u}}$ and a time-varying fluctuation $\mathbf{u}'(t)$. If we denote the zonal, meridional and vertical velocity components at a given time as u , v , w , respectively, we can write:

$$u = \bar{u} + u', \quad v = \bar{v} + v', \quad w = \bar{w} + w' \quad (3.1)$$

where overbars represent the time-mean over the 18 years of simulation and primes denote the time-dependent fluctuating part (the eddy component of the flow). From the previous formulation, the time averaged KE of the flow at a given location can be decomposed into the sum of an MKE and a time-averaged EKE. These terms, per unit volume, are defined as:

$$K_m = \frac{1}{2} \rho_0 (\bar{u}^2 + \bar{v}^2), \quad (3.2)$$

$$K_e = \frac{1}{2} \rho_0 \overline{(u'^2 + v'^2)} \quad (3.3)$$

The contribution of the vertical component of the velocity field w is not considered here as it is one or two orders of magnitude lower than the horizontal components.

The total KE can be readily obtained from Equations (3.1) - (3.3) as:

$$K = \frac{1}{2} \rho_0 \left(\bar{u}^2 + \bar{v}^2 + (\bar{u}'^2 + \bar{v}'^2) + 2\bar{u}\bar{u}' + 2\bar{v}\bar{v}' \right) = K_m + K_e \quad (3.4)$$

since $\bar{u}\bar{u}' + \bar{v}\bar{v}' = 0$, by definition. The reader is referred to Appendix D for further details on EKE derivation from the Reynolds Averaged Navier-Stokes (RANS) equations.

On the other hand, the available potential energy (APE) of a fluid at a given state represents the amount of PE which can be converted into KE during an adiabatic rearrangement of the fluid. In a broad sense, it can be defined as the difference between the PE for a given state of the fluid and a hydrostatic, stable reference state in which isentropic surfaces are horizontal and thus the PE is minimal (Reid et al., 1981). Quoting this work, although the elastic internal energy also supplies PE to the fluid, the APE of the ocean is dominated by the gravitational PE. Given the complexity of the calculation of the internal energy, this analysis is restricted to the gravitational contribution to APE, for which we adopt a commonly used definition for the ocean based on the quasigeostrophic approximation (Huang, 2005; Storch et al., 2012; Chen et al., 2014). As in the case of KE, the APE per unit volume at a given location can be divided into a time MAPE, P_m , and an EAPE, P_e :

$$P_m = -\frac{g}{2n_0} \bar{\rho}^{*2}, \quad (3.5)$$

$$P_e = -\frac{g}{2n_0} \bar{\rho}^{*r2}, \quad (3.6)$$

where n_0 is the vertical gradient of the local potential density averaged in time and over the study area (assumed constant at each vertical level). The density anomaly $\rho^* = \rho - \rho_r$ is the deviation of the local density from that of a predefined reference state ρ_r chosen to be the area-averaged time-mean density, thus constant at each level. While the APE of the mean flow (MAPE) is determined by the time mean of the density anomalies, $\bar{\rho}^*$, the available potential energy of the eddy flow (EAPE) is given by its variance, since $\bar{\rho}^{*r2} = (\bar{\rho}^* - \bar{\rho}^*)^2$.

Equations (3.2) and (3.3) and (3.5) and (3.6) are used in the next section to obtain the energy equations involved in the LEC. Definitions of P_m and P_e are strongly affected by the choice of the reference density and, further, several assumptions regarding the equation of state have to be adopted in order to obtain their respective energy equations. Although this constrains the interpretation of the APE in a quantitative

sense, these approximations provide manageable expressions for their derivation and are suitable for analysis of the mean-eddy flow energy transfers involving the LEC (Storch et al., 2012).

3.1.2 The Lorenz Energy Cycle

Lorenz (1955) developed a formulation for the energy cycle in the atmosphere based on considering the fluid as a heat engine: "the incoming solar radiation generates potential energy that is transferred to kinetic energy and is finally lost to frictional dissipation" (Li et al., 2007). In particular, the LEC describes the steady-state balance of four energy reservoirs: the MKE and the MAPE, K_m and P_m , respectively; and the time-averaged EKE and EAPE from the time-varying circulation, K_e and P_e , respectively.

Storch et al. (2012) provide an estimation of the LEC for the world ocean derived from numerical simulation. This study, however, warns about the application of the LEC to ocean dynamics for different reasons: from the initial hypothesis (the ocean cannot be considered as a heat engine since the energy is mainly driven by air-sea interactions) to the fact that determining the amount of APE to be converted into KE is a complex issue in weakly stratified regions with complex topography (Wu et al., 2017). However, the LEC is a valuable tool for studying the energy balance and the transfer between the different energy forms (Marchesiello et al., 2003; Sorgente et al., 2011; Renault et al., 2016). The major constraint is the selection of appropriate analysis regions since, as stated by Harrison and Robinson (1978): "because the terms of the LEC imply volume integration of the energy terms, it is desirable that the analysis regions be a quasi-homogeneous part of the flow, kinematically and dynamically distinct from the surroundings".

Complete derivations of the four energy balance equations involved in the LEC can be found in Storch et al. (2012) (see also Appendix E). Because our study region is a semi-enclosed domain, we adopt a simplified notation for the governing equations derived in Chen et al. (2014) as far as they permit to identify whether eddy-mean flow interactions are local or nonlocal, as will be explained below.

The four energy components satisfy the balance equations:

$$\frac{\partial K_m}{\partial t} + \nabla \cdot (\bar{\mathbf{u}} K_m) + \nabla \cdot (\bar{\mathbf{u}} \bar{p}) = -D(K_m) + M(K_m) + X(K_m) \quad (3.7)$$

$$\frac{\partial K_e}{\partial t} + \nabla \cdot [\overline{\mathbf{u}\rho_0(u'^2 + v'^2)/2}] + \nabla \cdot (\overline{\mathbf{u}'p'}) = D(K_e) + M(K_e) + X(K_e) \quad (3.8)$$

$$\frac{\partial P_m}{\partial t} + \nabla \cdot (\overline{\mathbf{u}}P_m) = D(P_m) + D(K_m) + X(P_m) + R(P_m) \quad (3.9)$$

$$\frac{\partial P_e}{\partial t} + \nabla \cdot [-\overline{\mathbf{u}g\rho'^2/(2n_0)}] = D(P_e) - D(K_e) + X(P_e) + R(P_e), \quad (3.10)$$

where $D(\cdot)$ and $M(\cdot)$ denote the rate of change of the energy form given in parentheses resulting from eddy density fluxes and eddy momentum fluxes, respectively; $X(P_m)$ and $X(P_e)$ involve rates of change related to vertical mixing, heat and fresh-water fluxes; and $X(K_m)$ and $X(K_e)$ are related to wind-stress, friction and bottom drag. The $R(\cdot)$ terms represent higher-order quantities which can be neglected in the adopted quasigeostrophic framework. The terms on the lhs in Equations (3.7) - (3.10) represent the corresponding energy rates of change due to temporal variations, advection and pressure work, respectively. Neglecting the temporal rates of change, since we are considering a statistically steady state, the oceanic LEC is summarized in Figure 3.1.

With the aim to investigate the possible physical mechanisms behind perturbation growth and their spatial distribution along the WMed domain, this study is focused on the mean-eddy flow interaction terms that involve EKE production. More specifically,

$$D(P_m) = \frac{g}{n_0} \overline{\rho^*} \nabla_h \cdot (\overline{\mathbf{u}'_h \rho'}) \quad (3.11)$$

represents the energy released from the unstable mean flow resulting from horizontal density fluxes. The corresponding eddy energy gain is

$$D(P_e) = \frac{g}{n_0} \overline{\rho' \mathbf{u}'_h} \cdot \nabla_h \overline{\rho^*}, \quad (3.12)$$

from which eddy growth implies that both the horizontal eddy density flux and the mean horizontal density gradient point in the same direction.

Conversion from EAPE to EKE is driven by eddy buoyancy work and is defined as

$$D(K_e) = -g \overline{\rho' w'} \quad (3.13)$$

The sinking of denser water masses and the upwelling of lighter ones involves a reduction of the PE of the system offset by an increase of KE, resulting in positive values of $D(K_e)$. This is also referred to as the baroclinic conversion term.

The rate of change of MKE caused by eddy momentum fluxes is defined as

$$M(K_m) = -\rho_0 [\overline{u} \nabla \cdot (\overline{u' \mathbf{u'}}) + \overline{v} \nabla \cdot (\overline{v' \mathbf{u'}})], \quad (3.14)$$

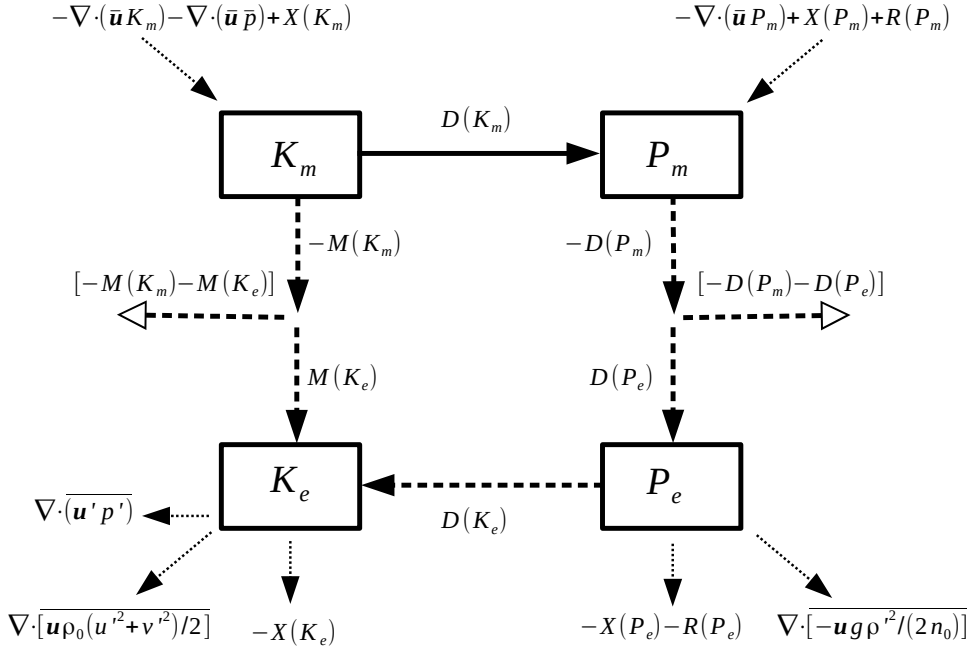


Figure 3.1: Oceanic LEC showing the transfers among the four energy reservoirs. The amounts correspond to the same terms in equations (3.7) - (3.10) integrated over the considered ocean volume. Dashed arrows depict the possible routes for eddy-mean flow interaction through eddy momentum fluxes (M) and through eddy density fluxes (D). When mean-eddy flow interactions are local, the terms in brackets are negligible and all the energy released from the mean flow is transferred to the local eddies. The other terms involved in the energy budget equations but not considered in this analysis are represented by dotted arrows. Adapted from Chen et al. (2014).

while the gain in EKE results from interaction of the horizontal Reynolds stress field with the mean flow shear:

$$M(K_e) = -\rho_0(\bar{u}'\bar{u}' \cdot \nabla \bar{u} + \bar{v}'\bar{u}' \cdot \nabla \bar{v}), \quad (3.15)$$

From the pairs of Equations (3.11) and (3.12) and (3.14) and (3.15), a local eddy-mean flow interaction implies that all the energy released from the mean flow is transferred to the eddy flow in the same region. In this case, the quantities $-D(P_m)$ and $-M(K_m)$ amount exactly to $D(P_e)$ and $M(K_e)$, respectively, when integrated over the region volume. On the other hand, the interaction is considered nonlocal when part of the energy released from the mean flow is conveyed to other regions. Following the formulation derived in Chen et al. (2014), the eddy-mean flow interaction is of a local

nature if the volume integrals of the divergence forms

$$\int_V [D(P_m) + D(P_e)] dV = \int_V \nabla_h \cdot \left(\overline{\mathbf{u}'_h \rho'} \frac{g}{n_0} \overline{\rho^*} \right) dV, \quad \text{and} \quad (3.16)$$

$$\int_V [M(K_m) + M(K_e)] dV = -\rho_0 \int_V [\nabla \cdot (\overline{u u' \mathbf{u}'}) + \nabla \cdot (\overline{v v' \mathbf{u}'})] dV \quad (3.17)$$

are negligible (see Figure 3.1).

From Equations (3.7) - (3.10) and the simplified LEC schematized in Figure 3.1, a regional characterization of the sources of eddy-mean flow interactions can be depicted by checking the local predominance of any of these terms among the others, as will be described in section 3.2. In fact, baroclinic instabilities set the conditions for MAPE conversion into EKE through the pathway $-D(P_m) \rightarrow D(P_e) \rightarrow D(K_e)$, while barotropic instabilities, reflecting the interaction of the mean flow with horizontal Reynolds stresses, result in a KE exchange from the mean to the eddy flow via $-M(K_m) \rightarrow M(K_e)$.

Besides the mean-eddy flow energy routes, the role of the mean and time-varying winds in generation of MKE and EKE (considered in terms $X(K_m)$ and $X(K_e)$ in Equations (3.7) and (3.8), respectively) is also analyzed, given the known strong influence of surface winds in driving ocean dynamics in key areas of the domain, such as the Gulf of Lions and Alboran Sea. At a given location, KE inputs from the mean and time-varying winds to the mean and eddy flows, respectively, are defined as:

$$f_m k_m = \overline{\tau_{x,s}} \overline{u} + \overline{\tau_{y,s}} \overline{v}, \quad (3.18)$$

$$f_e k_e = \overline{\tau'_{x,s} u} + \overline{\tau'_{y,s} v}, \quad (3.19)$$

where $\overline{\tau_{x,s}}$ and $\overline{\tau_{y,s}}$ represent the zonal and meridional components of the time-averaged surface wind stress, respectively, and $\tau'_{x,s}$ and $\tau'_{y,s}$ their corresponding fluctuations. The global contribution of surface winds to the MKE and EKE budgets can be obtained by integrating the aforementioned quantities over the domain area.

Energy transfer from the mean surface winds to the mean flow ($f_m k_m$) can also indirectly result in EKE production, following a conversion path which involves, first, a transformation from K_m into P_m through buoyancy flux, represented by the $D(K_m)$ term in Equations (3.7),(3.9) and defined as

$$D(K_m) = -g \overline{\rho^*} \overline{w}, \quad (3.20)$$

followed by the conversion route $P_m \rightarrow P_e \rightarrow K_e$ driven by baroclinic instabilities (Marchesiello et al., 2003).

3.2 Results

To further characterize the mesoscale dynamics of the western Mediterranean region, we carry out a statistical analysis of KE budgets and their spatial variability. As a start, the mean circulation patterns derived from the model are analyzed and linked to the KE budgets for the mean and time-varying flows.

3.2.1 Surface mean currents

Permanent large scale currents in the WMed region are well reproduced in the simulation, averaged over the whole 18-yr period (Figure 3.2, top). Incoming AW through the SoG first follows the permanent WAG followed by the weaker and quasi-permanent EAG south of the Gulf of Almeria. Seasonal analysis (Figure 3.2, bottom) reveals that both structures appear more intense and well defined in summer, with mean speeds reaching more than 90 cm s^{-1} , while the strength of the currents decay towards the winter season. The EAG shows higher variability in both size and position which, in turn, modulates the size and strength of the AO front, where the first major clash between incoming fresh AW and MW occurs.

From this point, most of the flow continues along the African coast, forming the AC. It is especially strong and narrow between 1°W and 1°E , but then starts meandering and generating short-lived mesoscale eddies which detach northwards from the main current, spreading AW into the interior of the basin. This behavior is more pronounced during the warmer seasons, while in autumn and winter the AC flows eastwards, mostly concentrated along the coast. The spreading of this current can be first detected around 2°E , where it draws a cyclonic deflection towards the Gulf of Alicante. When facing the coast, this branch forms an anticyclonic gyre with significant intensity on its northern flank.

The intensity and variability of this northward current in the Gulf of Alicante strongly affects the water transport through the Ibiza Channel and, by extension, the circulation patterns within the Balearic Sea, a semienclosed subbasin embedded between the Catalonian coast and the Balearic archipelago. Two principal inputs feed this area: across its northern edge the well defined NC advects cooler MW, while in the south the narrow Ibiza Channel receives warmer waters from the Gulf of Alicante. The main permanent structure is the Balearic Current (BC), which flows northeastwards

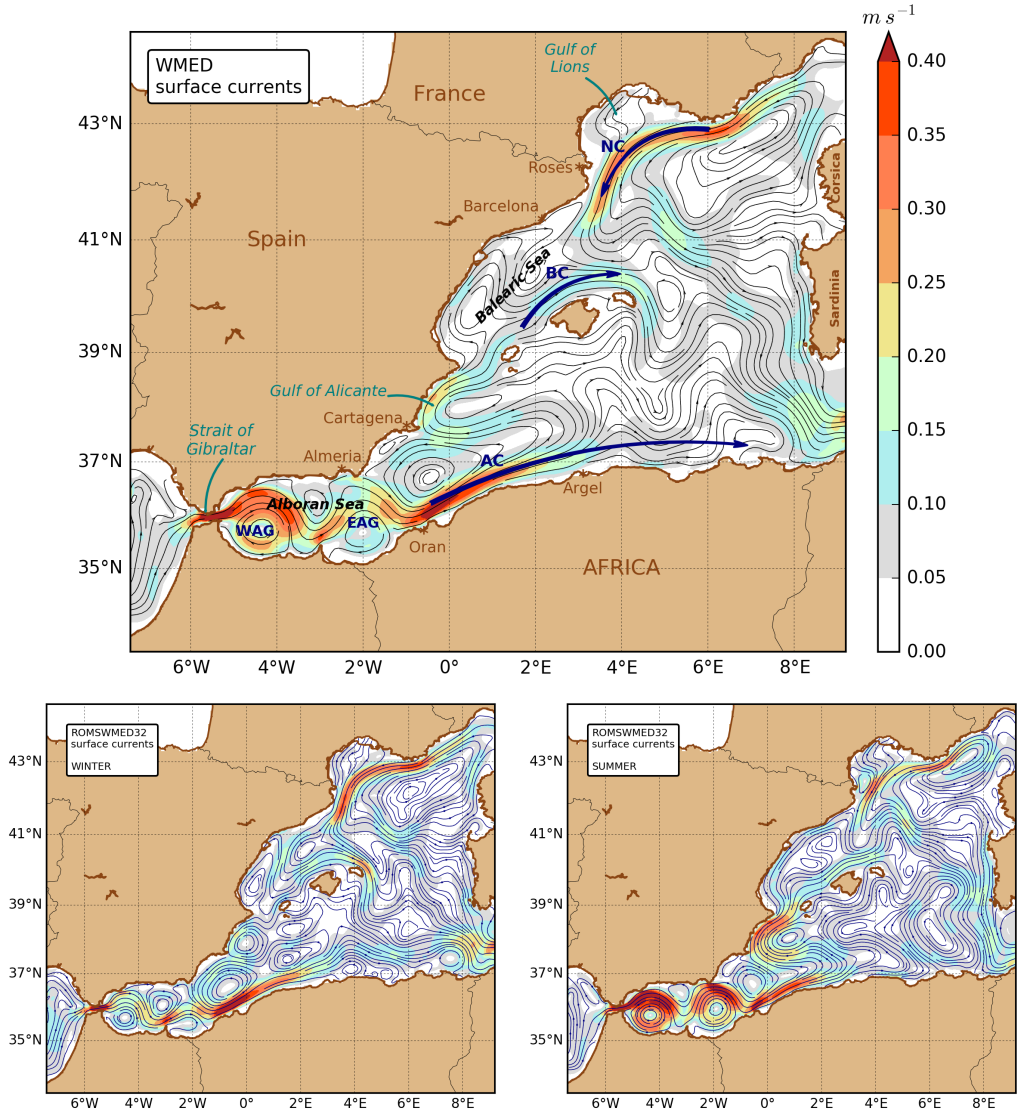


Figure 3.2: Top: Averaged surface velocity for the 1995 – 2012 period from the model output. Streamlines are depicted in black, while dark blue arrows show the main paths of the principal currents: NC, BC and AC. Although the colorbar range for surface speeds is restricted to 0.40 ms^{-1} , maximum values up to 0.90 ms^{-1} are registered through the Strait of Gibraltar and around 0.5°W within the AC. Bottom: The surface velocity fields averaged over the winter (December–February, left) and summer (July–September, right) months, respectively.

from the Ibiza Channel along the northern edges of the three main islands. Initially fed by the southern warm waters, it is reinforced along its trajectory by occasional currents derived from interior meanders and small eddies and eventually by incoming waters crossing the Mallorca Channel. At the northern edge, a significant contribution

from colder waters apparently detached from the original NC helps to enhance the BC in the last part of its journey towards Menorca.

A strong signature of the NC is seen in the area of the Gulf of Lions, with a noticeable weakening in summer. North of the Balearic Islands, this current undergoes a marked deflection and divides into two main branches: the first branch starts to detach south-eastward along the gulf path, merging with the BC north of Menorca. Part of this flow completes a cyclonic gyre covering the northern half of the basin, while the rest keeps flowing south-eastwards and joins the remnants of the AC toward the Tyrrhenian Sea. The second branch of the NC keeps flowing along the continental shelf, entering the Balearic Sea. Given the complex topographic configuration of this area, the weakened residual branch of the NC can occasionally keep flowing southwards along the Spanish coast crossing the Ibiza Channel or, mostly, undergo a major cyclonic deflection around 40°N and join the BC in front of Mallorca coast, as depicted from the time-averaged pattern in Figure 3.2.

3.2.2 Kinetic Energy analysis

Mesoscale features derived from the simulation are analyzed on the basis of KE budgets and their spatial variability. Following the definitions given in Equations (3.2) and (3.3), maps of surface MKE and time-averaged EKE for the period 1995–2012 in the WMed are shown in Figure 3.3.

Spatial distributions of both MKE and EKE present significant differences. The highest MKE is concentrated along the paths of the main currents: the Alboran system, AC, NC, and, with less intensity, along the BC and the Cartagena current. By contrast, the EKE distribution presents a very disperse pattern, with a strong signal throughout the Alboran region (reaching nearly $1300 \text{ cm}^2\text{s}^{-2}$) and along and offshore of the AC. Notable but less intense is the signal along the BC, while the track of the NC is barely noticeable. The scattered distribution of EKE reveals high variability in the position and intensity of these structures over time; in this regard, the AC is known to display a narrow and well defined pathway at the beginning, also depicted in the MKE map, while showing increasing instabilities as it advances eastward, in the form of meanders and eddies which detach from the initial along-coast current toward the center of the basin, as revealed by the high values of EKE covering the southern half of the domain. The opposite situation is found along the track of the NC, where the negligible EKE

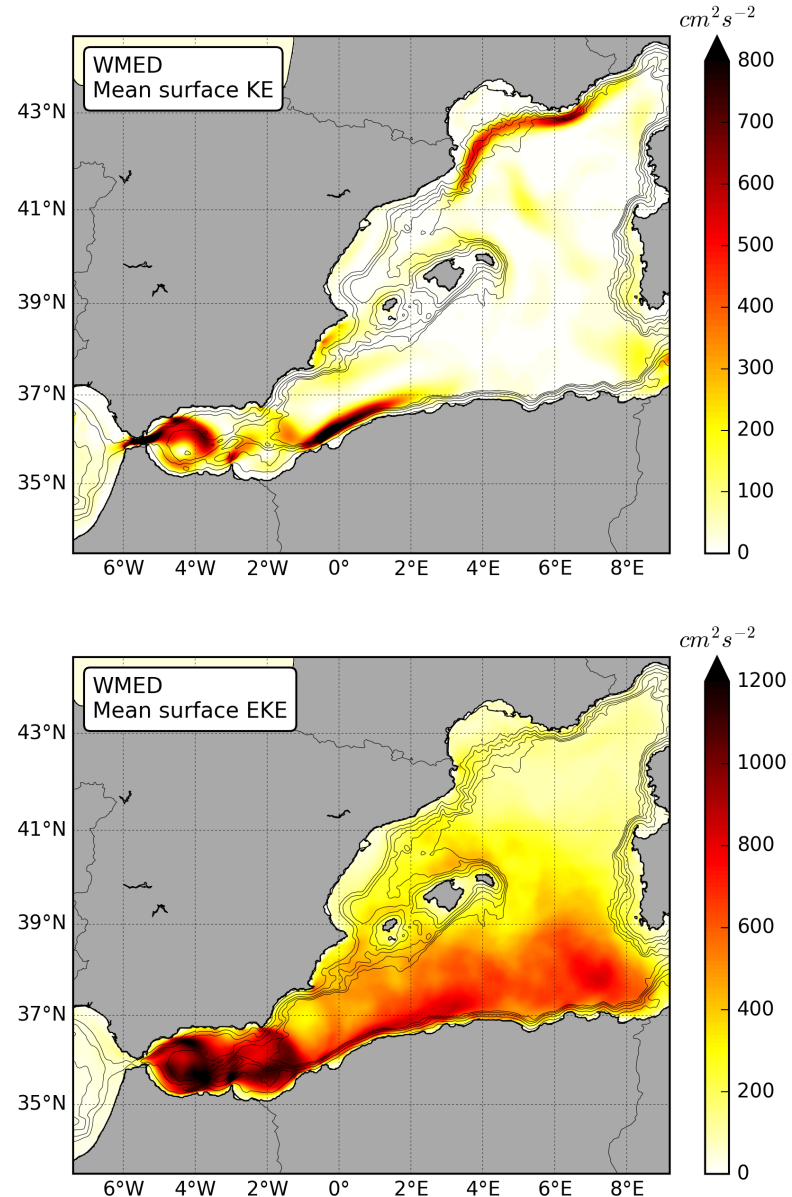


Figure 3.3: Top: Surface MKE (in $\text{cm}^2 \text{s}^{-2}$) computed from mean surface velocity components, \bar{u} , \bar{v} for the period 1995 -2012 following (3.2) and dividing by ρ_0 . Values above $800 \text{ cm}^2 \text{s}^{-2}$ reach up to $3660 \text{ cm}^2 \text{s}^{-2}$ within the SoG and up to $1300 \text{ cm}^2 \text{s}^{-2}$ around 0.5°W in the AC. Bottom: Surface mean EKE (in $\text{cm}^2 \text{s}^{-2}$) computed by time-averaging EKE daily values, obtained from daily surface eddy velocity components, u' , v' , using (3.3) divided by ρ_0 . Within the Alboran gyres, mean EKE values reach up to $1300 \text{ cm}^2 \text{s}^{-2}$. In both figures black contour lines represent 200, 500, 1000, 1500 and 2000 m isobaths.

signal contrasts with the large MKE, revealing the steady position and intensity of the main stream.

3.2.3 Energy budgets

KE budgets have been calculated by integrating the corresponding time-averaged quantities for the period 1995 - 2012 over the entire WMed domain. While MKE amounts to 0.6 PJ, the volume integrated EKE reaches 2.3 PJ, more than three times the MKE budget. Both magnitudes are mostly concentrated in the upper 100 meters and remain virtually negligible deeper than 300 meters. In general, KE generation and conversion rates display a seasonal nature.

From the area integral of the $f_e k_e$ term in Equation (3.19), time-varying winds supply a total amount of 2.7 GW of KE to the time-varying circulation. The spatial distribution in Figure 3.4 (left) reveals a noticeable increase during winter, according to the enhancement of the wind regime during the cold season. In contrast, the mean wind work budget given by the area integral of the $f_m k_m$ term in Equation (3.18) accounts for only 685 MW, around 25% of the total $f_e k_e$ contribution.

Larger inputs to the $f_e k_e$ budget come from the Alboran Sea and Gulf of Lions, the areas most affected by the strongest winds. In contrast, the regional $f_m k_m$ displays a more complicated pattern for which several aspects are worth highlighting: first, in the Gulf of Lions, the inverted-V shape of positive KE generation near Cape Roses reflects the deflection of the NC into two main branches, one following the Spanish coast and the other directed offshore towards the SE. The interaction with the southeastward branch extends to the southeastern extreme of the domain, south of Sardinia, especially in winter. On the other hand, where the NC enters the Gulf of Lions, a marked negative contribution is reflected along both seasons, meaning that in this region the main current flows against the mean winds. The positive contribution detected in winter north of Menorca is especially strong along the last stretch of the BC, an area that is known to be specially affected by northerly winds. During this season, the AC is also propelled eastward by following mean winds. Conversely, in summer, $f_m k_m$ (Figure 3.4, bottom right) it displays a much more variable pattern, with dipoles of positive and negative $f_m k_m$ which, when integrated over the whole domain, explain the minor contribution of $f_m k_m$ to the domain-integrated budget.

Regarding potential energy, as explained in Section 3.1, the APE budgets for mean and eddy flows, P_m and P_e , are quantitatively meaningless since their formulations are based on an ideal, predefined minimum energy state of the ocean which strongly depends on the choice of the reference density ρ_r and is highly affected by the accuracy,

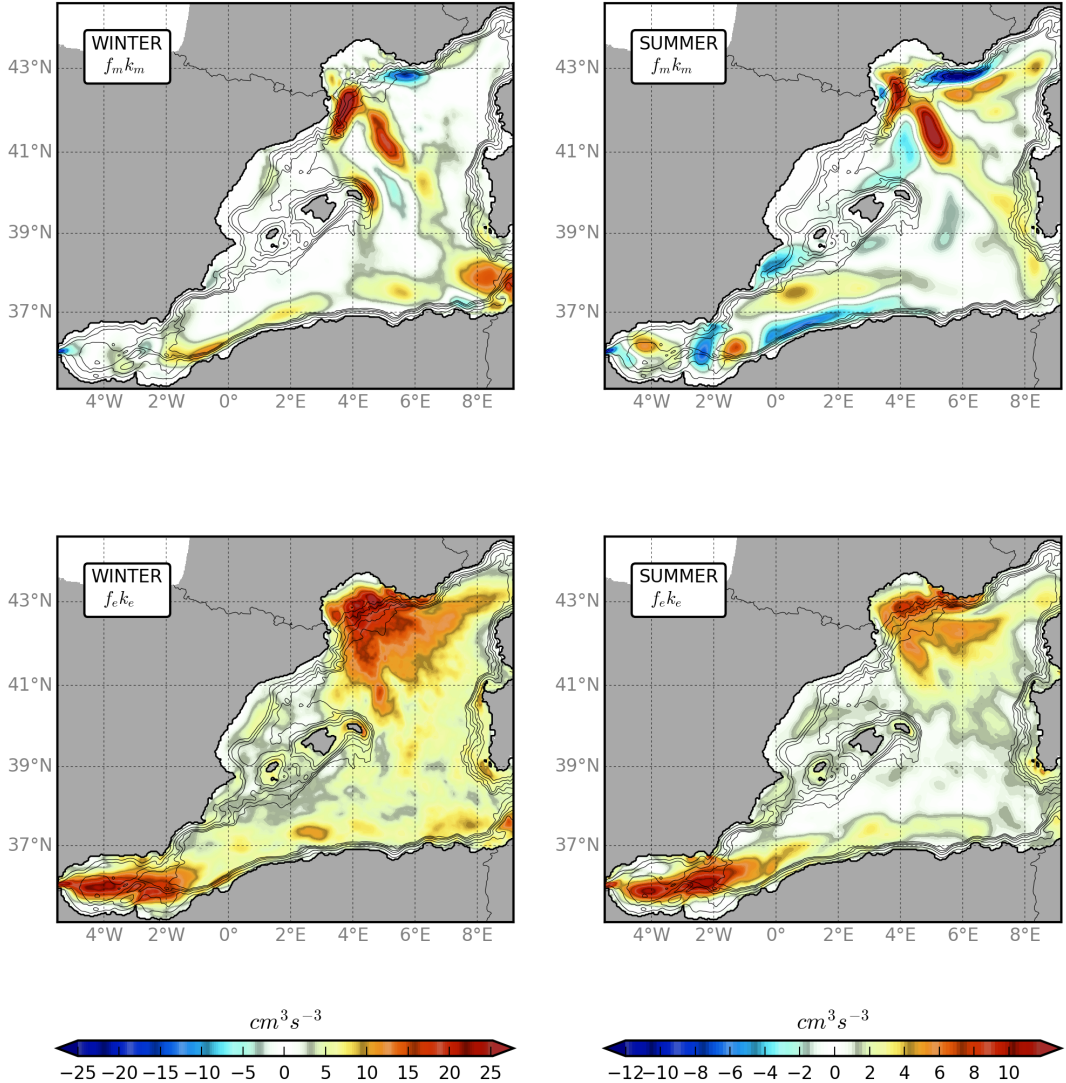


Figure 3.4: Kinetic energy generation from windwork for winter (left) and summer (right). Note that colorbar ranges are different for each season. Top panels depict local MKE transfer from mean surface winds to the mean flow, while bottom figures show EKE generation by windwork anomalies. Black contour lines represent 200, 500, 1000, 1500 and 2000 m isobaths.

the resolution of the model, and the processes solved. For this reason, its application is reserved to the analysis of the mean-eddy flow interactions.

3.2.4 Regional LEC and mean-eddy flow interactions

Considering the whole WMed domain, the principal routes for eddy-mean flow interaction are displayed in the simplified LEC in Figure 3.5. The rates of change of the terms involving EKE conversion are obtained integrating Equations (3.11) - (3.15) over the domain volume. The diagram shows that baroclinic instability drives most of the EKE production via $P_m \rightarrow P_e \rightarrow K_e$ conversion. The values of $-D(P_m)$ and $D(K_e)$ suggest that most of the MAPE released from the mean flow is converted into EKE in the same region, while the non-zero divergence term (Equation (3.16)), negative in sign, reveals that certain amount of EAPE is also injected through the boundaries into the WMed domain. By contrast, the amount of EKE gained through eddy momentum fluxes via the path $K_m \rightarrow K_e$ is less than one-fourth of the baroclinic production. In this case, the external contribution represents about 15% of the $M(K_e)$ input; this energy route is therefore mainly driven by barotropic instabilities of local nature.

Based on the mean currents and KE regional distributions described in previous sections and schematized in Figures 3.2 and 3.3, respectively, the WMed domain can be divided into three main sub-regions that are more or less dynamically distinct from each other, although continuously interacting between them as well as with the surrounding waters (Figure 3.6): The Alboran Sea, interacting with the Atlantic ocean through the Strait of Gibraltar and bounded by the Algerian Basin to the east; the Algerian Basin, also bounded by the Tyrrhenian Sea to the east and by the Balearic Islands to the north; and the Northern Basin, covering the northernmost sector of the domain. WMed mean-eddy flow interactions have also been considered separately in these sub-regions in order to analyze, first, the dominant energy routes in each sector (by means of regional LECs) and, second, the spatial distributions of the energy conversion terms in Equations (3.11) - (3.17).

Regional LECs corresponding to the three WMed sectors are illustrated in Figure 3.6 (left) and spatial representations of the energy conversion terms enable identifying the areas where those transformations take place (Figures 3.7 - 3.9).

In the Alboran Sea (Figure 3.6, top) EKE production via barotropic and baroclinic instabilities are comparable, although the APE divergence term reveals that nearly half of the EAPE is injected from the surroundings, while the $K_m \rightarrow K_e$ transformation results mainly from local processes. A certain amount of K_m is also transported out of this area, presumably towards the Algerian Basin, as expected from the dynamics

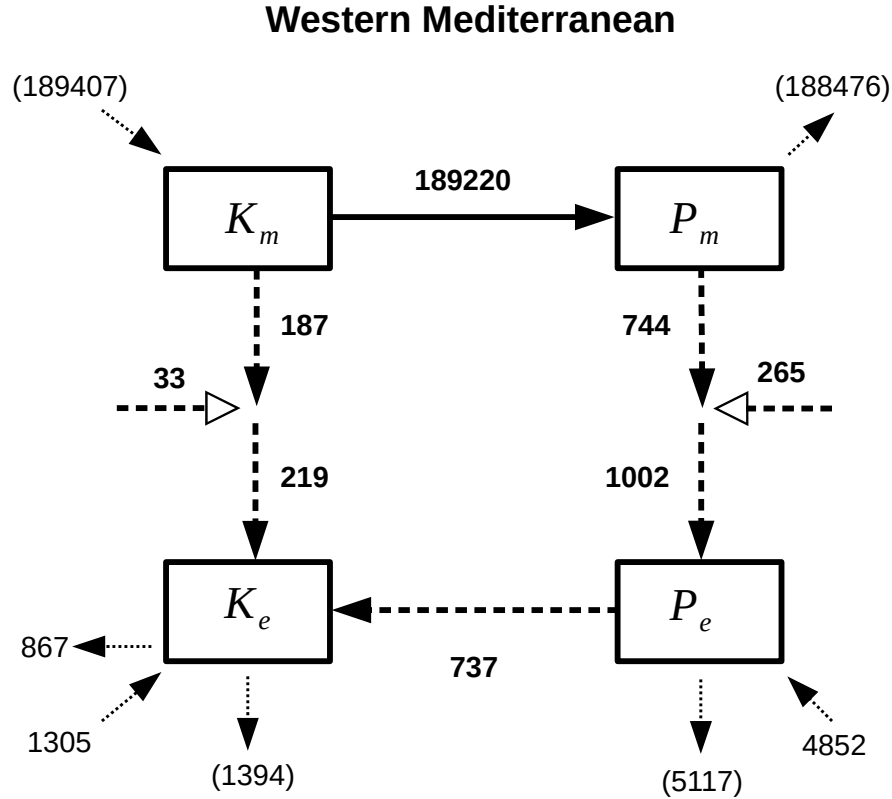


Figure 3.5: Simplified LEC in MW for the WMed region following the scheme in Figure 3.1 and balance equations (3.7) - (3.10). The time rates of change of the energy components are neglected since we are considering a statistically stationary state. Amounts have been computed from time-averaged model data along the 1995-2012 period and integrating over the domain volume. The terms in brackets are obtained from residuals. Adapted from Chen et al. (2014)

in this region. From Figure 3.7, Alboran Sea displays the strongest $D(P_e)$ signature, showing a marked and alternating dipole pattern of positive and negative values. Red (blue) areas reveal that the eddy flow gains (releases) APE from (to) the mean flow. This is consistent with the $D(P_m)$ mapping, which displays a similar distribution with opposite sign although much lower amounts. The $D(K_e)$ pannel reflects two different patterns of $P_e \rightarrow K_e$ conversion which might respond to different sources of instabilities. First, at the exit of the SoG and south of the Almeria cape we find two broad positive regions. In these areas, where the AW usually meets with resident MW – in the form of a fresh incoming jet (the AJ) or a strong front (the AO front) – the clash of the two water masses could be mostly responsible for the baroclinic instabilities driving the $P_e \rightarrow K_e$ conversion. On the other hand, the spotty blue/red pattern along some steep

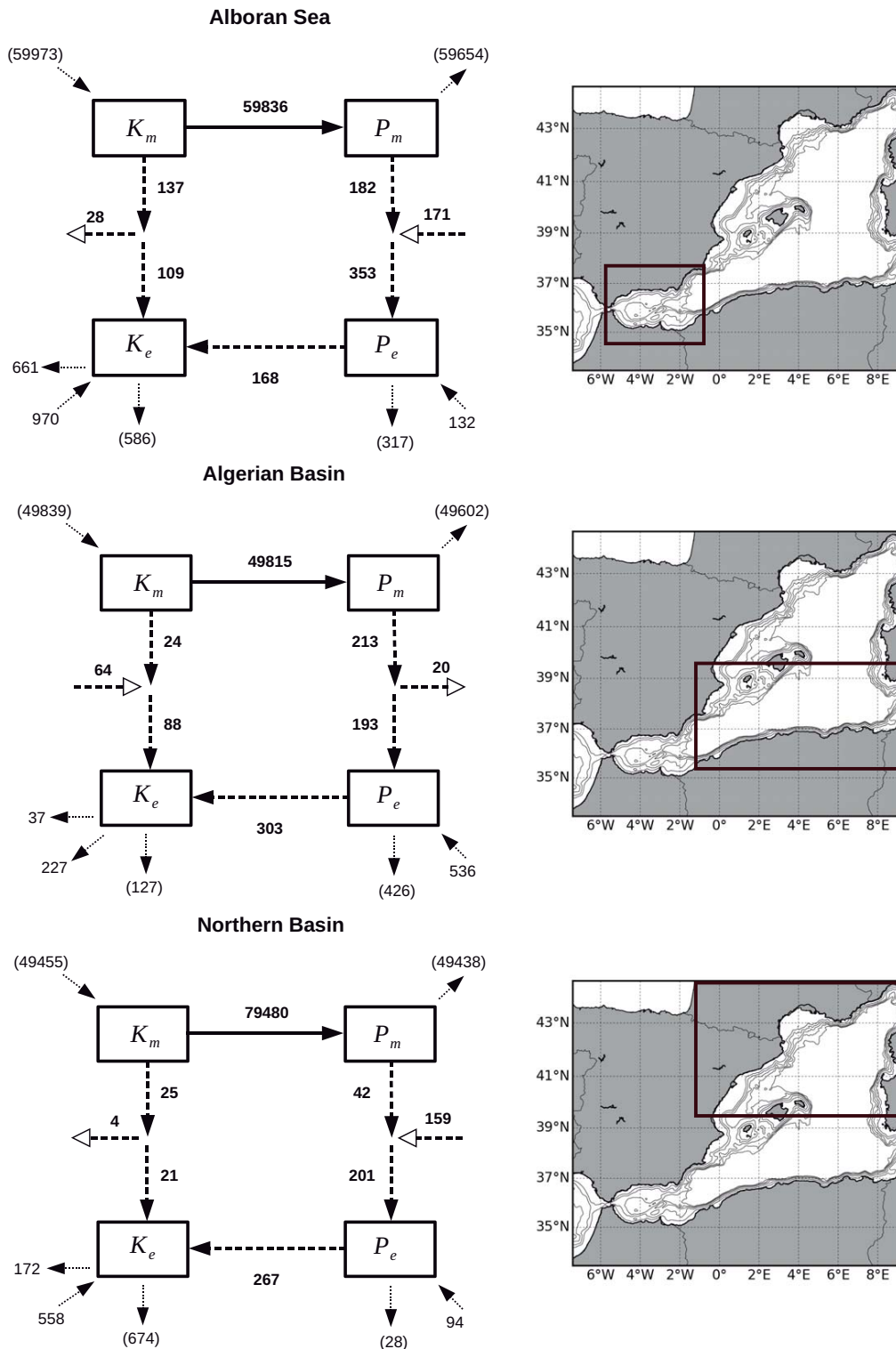


Figure 3.6: Simplified LEC in MW for the three sectors (right figures) in the WMed region following the scheme in Figure 3.1 and Equations (3.7) - (3.10), as in Figure 3.5.

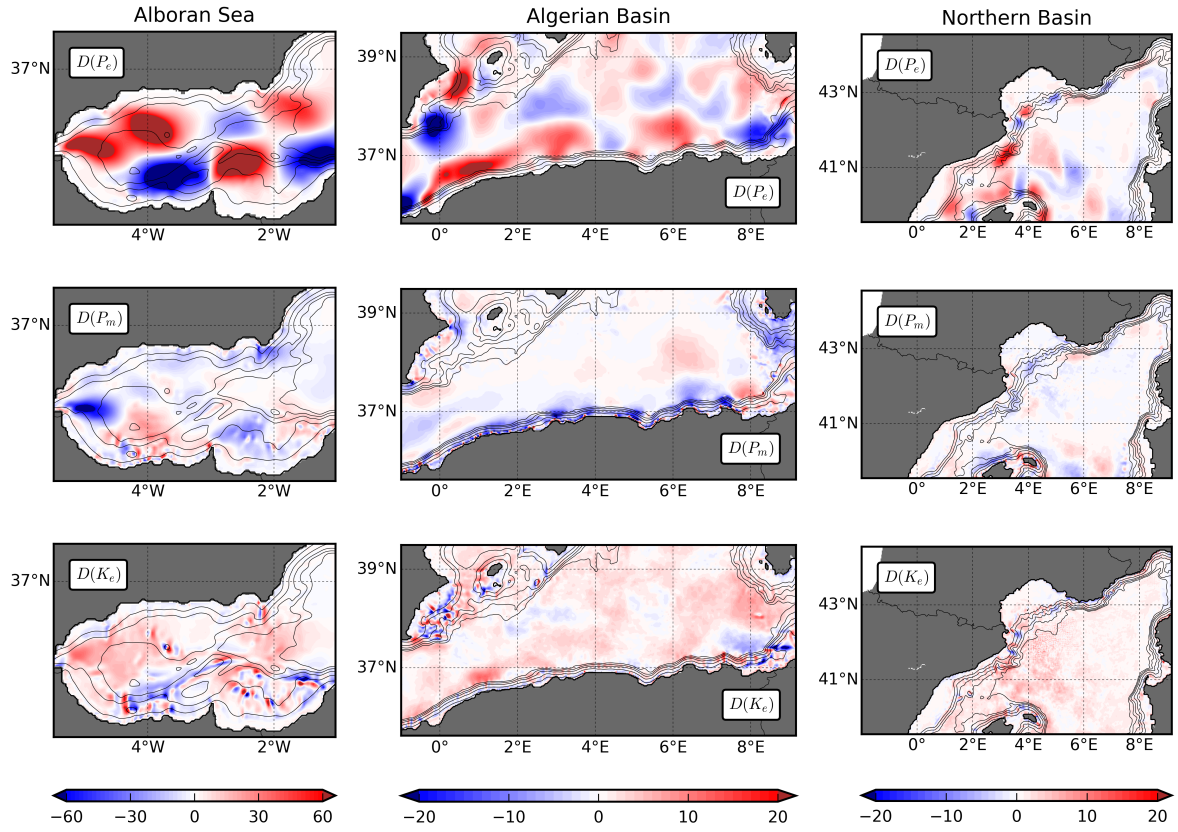


Figure 3.7: Regional distribution for Alboran Sea (left), Algerian Basin (middle) and Northern Basin (right) of the mean-eddy flow interaction terms (in cm^3s^{-3}) driven by eddy density fluxes $D(P_e)$ (top), $D(P_m)$ (center) and $D(K_e)$ (bottom), from top to bottom respectively. Note that colorbar limits are larger in Alboran region. Black contour lines represent 200, 500, 1000, 1500 and 2000 m isobaths.

bathymetric features reveal a topographic origin of such instabilities. The mismatch between the $D(P_e)$ and $D(P_m)$ signatures, as already revealed by the LEC scheme, arise from the non-locality of the EAPE production, represented by the divergence term $[-D(P_m) - D(P_e)]$ in Figure 3.9. The amounts are much significant in this area, and the red and blue patterns indicate whether the energy is leaving or entering the site. Conversion between MKE and EKE in Alboran Sea is dominated by horizontal shear instabilities; in those areas where the flow interacts with topographic features, the barotropic conversion term displays a strong double signal: conversion is from EKE to MKE on the upstream side of the obstacle, where intensified horizontal shear inhibits perturbation growth; on the downstream side, the current becomes unstable and perturbations extract KE from the mean flow. The non-locality of such transformations represented in Figure 3.9 displays a mixed pattern, although the integrated amounts

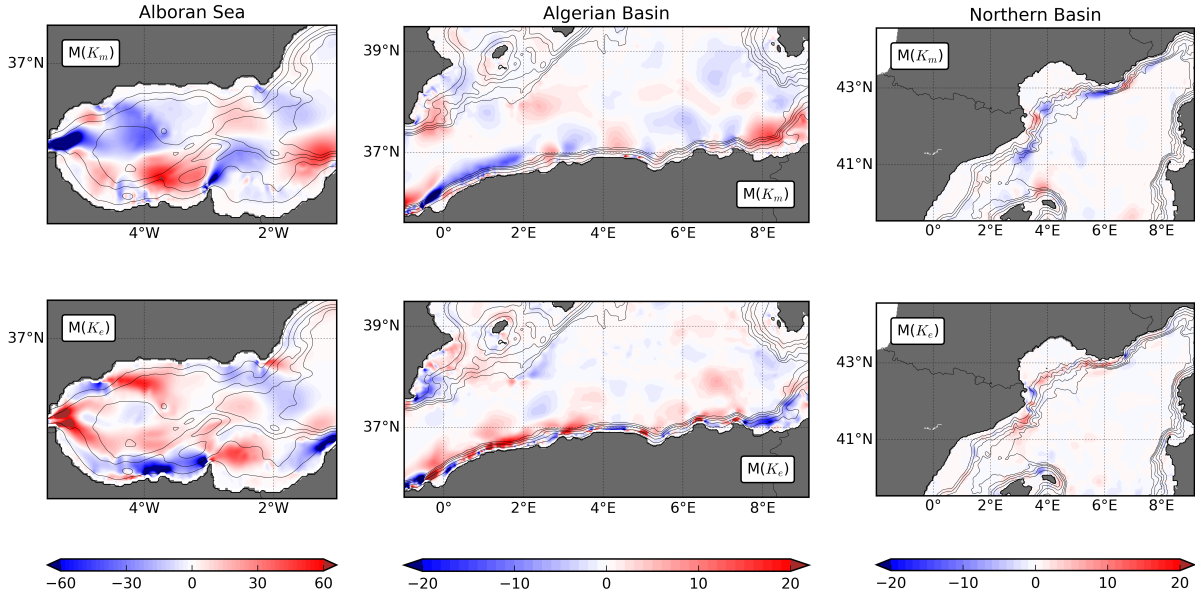


Figure 3.8: Regional distribution for Alboran Sea (left), Algerian Basin (middle) and Northern Basin (right) of the mean-eddy flow interaction terms driven by eddy momentum fluxes, $M(K_M)$ (top) and $M(K_E)$ (bottom), in cm^3s^{-3} . Note that colorbar limits are larger in Alboran region. Black contour lines represent 200, 500, 1000, 1500 and 2000 m isobaths.

showed in the LEC reveal a net outward transport of MKE.

In the Algerian Basin (Figure 3.6, middle), the nonlocality of the barotropic conversion route is much more evident. The divergence terms reveal that half of the EKE generation through eddy momentum fluxes is injected from other regions, while a small amount of the APE released from the mean flow is transported outside. The largest rates of EKE production derive from EAPE transformation. The spatial distributions of $D(P_m)$ and $D(K_e)$ shown in Figure 3.7 reveal such baroclinic conversion, displaying similar patterns of inverse sign.

The non-locality of the APE transformations is particularly apparent in the Northern Basin (Figure 3.6, bottom), since a considerable amount of P_e converted into K_e is supplied from adjacent regions. Barotropic instabilities are mostly local and the related EKE production via $K_m \rightarrow K_e$ results in less than a 10% of the $P_e \rightarrow K_e$ contribution.

An overview of the regional patterns of $P_e \rightarrow K_e$ conversion shows that baroclinic instabilities occur with more intensity along the paths of the principal currents. MLIs (mainly in winter) and frontal processes could be principal processes driving EKE

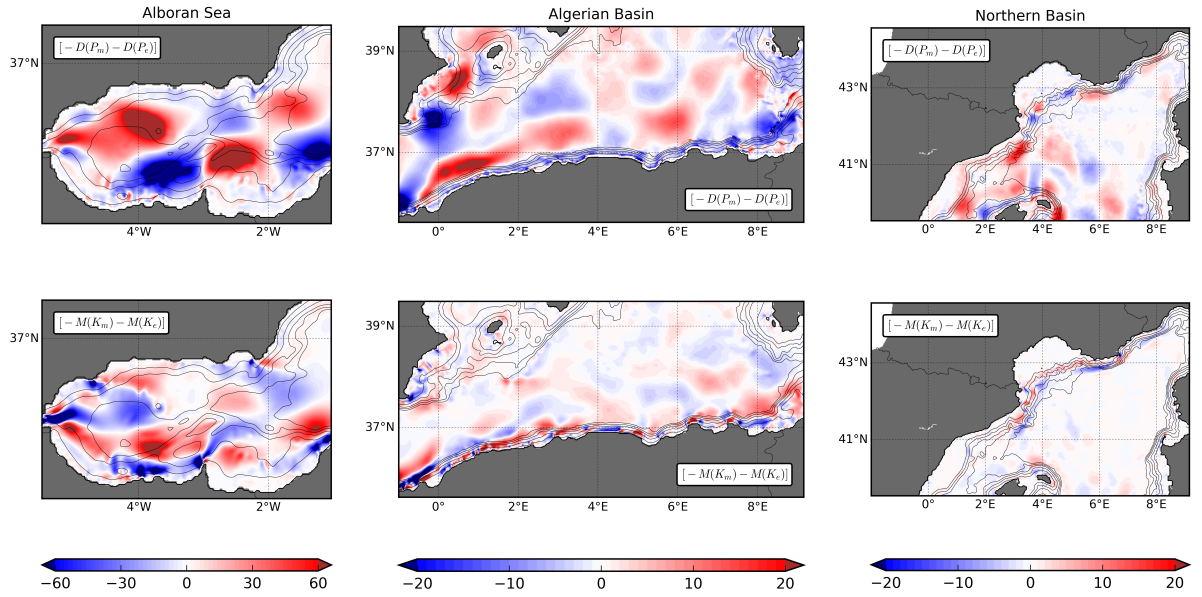


Figure 3.9: Regional distribution for Alboran Sea (left), Algerian Basin (middle) and Northern Basin (right) of the divergence terms $[-D(P_m) - D(P_e)]$ (top) and $[-M(K_m) - M(K_e)]$ (bottom), in cm^3s^{-3} . According to the corresponding LEC schemes from Figure 3.6, these amounts reflect the non-locality of mean-eddy flow transformations. Note that colorbar limits are larger in Alboran region. Black contour lines represent 200, 500, 1000, 1500 and 2000 m. isobaths.

production. Around the areas where along-coast currents flow over sharp bathymetric profiles and impact against rough, winding topographic features, a sequence of positive-negative dipoles are a common feature. This pattern frequently appears around the Balearic islands, in the Gulf of Alicante, south of Sardinia near the African coast, around the southern ridges of both Alboran anticyclonic gyres or along the path of the NC when crossing the Gulf of Lions. Supported by the known local dynamical behavior, the spatial characterization of the energy routes suggests that bathymetry plays a crucial role in driving the physical processes associated with EKE production. This will be discussed in next section.

3.3 Discussion

We consider a formulation of the Lorenz energy cycle for the western Mediterranean Sea, focusing on the eddy kinetic energy component, as a tool for analyzing the possible physical mechanisms providing the pathways from energy generation towards

dissipation. Eighteen years of daily data from a model simulation at $1/32^\circ$ resolution enable considering a statistically stationary state of the ocean, a necessary condition to obtain the energy balance equations involved in the LEC.

Mesoscale characterization

A regional characterization of the WMed within the mesoscale range is provided by analyzing the mean surface circulation patterns and their seasonal variability.

Mean large scale currents and their seasonal variability are well reproduced from the simulation: in the Alboran Sea, the incoming AW follows the permanent WAG and the quasi-permanent EAG, both being more intense and stable in summer. This can be linked to previous studies like Vargas-Yáñez et al. (2002), who show that summer months are characterized by the stability of the two-gyre system and associated fronts (*i.e.*, the AO front), and Renault et al. (2012) who confirm this stable double gyre system circulation for summer and autumn from the analysis of altimetry data. The model dynamics of the Algerian Current is consistent with the behavior reported in earlier studies: Millot (1985) describes the AC as a near-coastal steady flow which becomes unstable around $1 - 2^\circ\text{E}$, generating eddies of both signs although only the anticyclonic ones evolve into mesoscale structures that can detach northwards and remain in the basin for several weeks. This activity decays during the cold seasons, when the AC flows mostly concentrated along the African coast. A recurrent cyclonic deflection is observed in the AC near 2°E , giving rise to an anticyclonic gyre in the Gulf of Alicante and an associated front (less defined than AO) between Cartagena and the Afrian coast, around $37^\circ\text{N} - 0.5^\circ\text{E}$. Recent studies by Mason and Pascual (2013); Pascual et al. (2017); Hernández-Carrasco and Orfila (2018) have reported evidence of this secondary front. In the northern half of the domain, the water transports through the Ibiza and Malloca Channels are strongly affected by the circulation patterns within the Algerian Basin, as already reported by Pinot et al. (2002) and Heslop et al. (2012). By extension, this also conditions the circulation in the Balearic Sea, characterized by the Balearic Current, flowing northeastwards along the Balearic archipelago, and a branch of the Northern Current, which flows southwestwards along the Spanish coast. Results show that this branch mostly deflects cyclonically, joins the BC in front of the Mallorca coast, and occasionally crosses the Ibiza Channel; conversely, the cited work by Pinot et al. (2002) argues that the water transport through the channel is dominated by the southward flow of the NC.

Mean circulation patterns are also reflected in the spatial distribution of surface MKE, which is concentrated along the paths of the principal currents. The Alboran system and around 0.5°W , where the AC emerges, show the highest energy amounts exceeding $800 \text{ cm}^2\text{s}^{-2}$ at certain points of the route; the NC is quite well defined (between $400 - 600 \text{ cm}^2\text{s}^{-2}$) and, with less intensity, the Cartagena and Balearic currents, showing around 300 and $200 \text{ cm}^2\text{s}^{-2}$, respectively.

The variability in the position and occurrence of mesoscale structures is reflected in the time-averaged EKE distribution, which presents a very diffuse pattern. The strongest signal is registered throughout the Alboran region and along the AC system, extending over the southern half of the domain, while in the north, the stability of the NC is reflected by the negligible EKE signal. A qualitative comparison with a previous work by Pujol and Larnicol (2005) based on the analysis of eleven years of altimetric data for the entire Mediterranean Basin shows that EKE regional distribution displays similar patterns in key areas such as the Alboran Sea and south of Sardinia, although our study depicts a wider domain of relevant activity, presumably not detected from satellite measurements. The validation of the ROMSWMED32 solution carried out by Escudier (2015) shows additional comparisons with estimations derived from altimetry, drifters trajectories and the parent NEMOMED12. Although the values are quite lower for altimetry and NEMOMED12, the spatial distributions from the considered data sets also show similar patterns to those from ROMSWMED32.

Simplified LEC and EKE production

The LEC, focused on the KE components of the energy balance equations, first provides a hint at the amounts of KE of the mean and eddy flows respectively stored within the WMed region.

While the volume integrated MKE values are around 0.6 PJ , the total EKE amounts to 2.2 PJ , more than three times the former. These results can be qualitatively compared to those obtained from Storch et al. (2012), who present an estimate of the LEC for the world ocean from a multidecadal simulation at $1/10^{\circ}$ resolution: 1.3 EJ of MKE against 3.5 EJ of EKE. Bridging the gap between the considered domains, resolution and model specifications, the ratio between the amounts of both forms of energy throws a similar result in the WMed region. Another common feature is the regional distribution, showing a MKE concentrated along the main currents, in contrast to the spread

distribution of EKE.

Regarding potential energy, the APE budgets are not considered here, since their formulations strongly depend on the choice of a minimum energy reference state of the ocean, which is highly affected by the accuracy of stored data and model resolution. Its application is reserved to the analysis of the mean-eddy flow interactions.

Besides providing an idea of the quantification of the ocean's KE, the LEC equations include energy generation, conversion and dissipation terms which can be used as a tool for analyzing the physical mechanisms responsible for maintaining the balance in the WMed and, in particular, in the three subregions: Alboran Sea, Algerian Basin and Northern Basin. Most of the power input to the time-varying circulation stems from the time-varying winds ($f_e k_e$), which are especially strong during the cold season in the Alboran Sea and in the Gulf of Lions (Northern Basin). By contrast, the energy transfer from mean winds to MKE ($f_m k_m$) displays a dipole pattern combining areas of positive and negative wind work contributions, which, when integrated over the whole domain, result in a minor contribution from the mean winds.

In general, baroclinic instability is the principal conversion pathway, subtracting EKE from eddy buoyancy work. Higher activity is found around most energetic regions dominated by strong currents and frequent mesoscale activity: north of the Balearic Sea, in front of the African coast, and particularly in both Alboran anticyclonic gyres, showing strong baroclinic conversion on their northern ridges in contrast with the opposite situation found at their southern edges, where EKE is converted into EAPE. This sequence of positive-negative dipoles is also found along other currents flowing over sharp bathymetric profiles: around the Balearic Islands, south of Sardinia in front of the African coast, in the Gulf of Alicante, or along the path of the NC when crossing the Gulf of Lions. Therefore, besides the role of frontal processes and MLIs known to drive baroclinic instabilities in specific sites of the WMed, interaction with abrupt topography might be an additional important source of energy conversion.

The results of the LEC analysis suggest that topographic features interact with the flow and induce a dynamical response to restore equilibrium in the form of a conversion between kinetic and potential energy and between the mean and eddy flow. This is noticeable in certain areas (*e.g.*, the Alboran Sea; the Algerian Current; the Balearic Archipelago; the the Gulf of Alicante or the Northern Current) which are characterized by more or less strong currents flowing along sharp bathymetric slopes, ridges, and

other topographic features. On this basis, Molemaker et al. (2015) suggest a mechanism by means of which energy is cascaded from the geostrophic flow into submesoscale structures via topographic vorticity generation. Although the ROMSWMED32 solution used in this study shows evidence of the occurrence of such process in this region, it reproduces very weakly the intermediate stages.

The analysis developed in this chapter constitutes the first step toward a submesoscale characterization of the western Mediterranean Sea, which we will undertake in the next chapters through a set of nested ROMS simulations focused in the Alboran Sea.

The results obtained in this Chapter are published in Capó et al. (2019).

Chapter 4

Mesoscale to submesoscale transition in the Alboran Sea

The second part of this study aims at identifying the submesoscale processes governing ocean dynamics in the Alboran Sea and at developing new strategies for their detection and further analysis.

Several reasons have led to the choice of this region to undertake the submesoscale exploration, for example:

- Results from the LEC analysis carried out in Chapter 3 reveal that the Alboran Sea is the most energetic region in the WMed, showing the largest eddy momentum and density fluxes resulting from eddy-mean flow interactions (Figures 3.7 and 3.8). Patterns of mean surface KE and EKE also reveal the strong variability governing the mesoscale circulation in this area (Figure 3.3).
- Endorsed by a large number of studies carried out over recent decades (see Section 1.5), this region exhibits a large variety of recurrent (sub)mesoscale processes promoted by the confluence of several factors: from the location and topographic shape of the basin, to the contrast between the water masses residing at both sides (AW and MW) and the different forcings to which they are exposed.
- Despite the extensive research that has been done in the Alboran Sea, the sources of the mesoscale variability are still not fully understood, and unraveling the role of the submesoscale processes in this region is still at a very early stage.

In this chapter we explore the transition from mesoscale to submesoscale dynamics in the Alboran basin from a set of two nested, realistic simulations specifically developed to this aim, WMed1500 and Alb500 (see Table 2.1 and Section 2.1.2).

While mesoscale eddies dominate both SSH and surface KE variability, ageostrophic motions appear at lower scales in the shape of SMCs (*e.g.*, fronts, filaments, SCVs), internal waves, etc. Figure 4.1 shows snapshots of surface relative vorticity normalized by the Coriolis parameter, ζ/f , from our parent and child simulations. While WMed1500 is dominated by mesoscale eddies (the two-gyre system is the most visible pattern) the vorticity field in Alb500 is characterized by a *submesoscale soup*, exhibiting submesoscale structures in the vicinity of frontal regions and along topographic features.

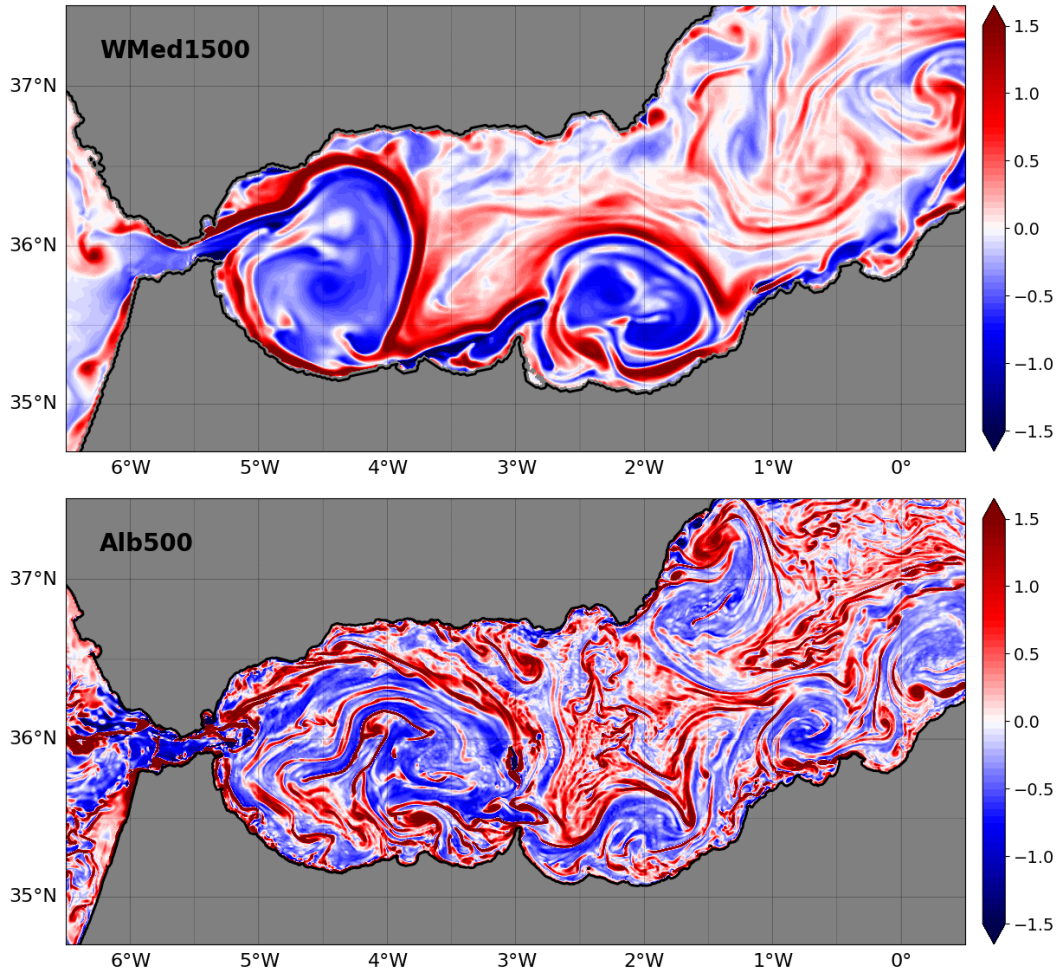


Figure 4.1: Snapshots of surface relative vorticity normalized by the Coriolis parameter, ζ/f , for the parent WMed1500 solution (top) and the nested child Alb500 (bottom) in November 11, 2013.

Throughout the next sections we use our set of nested simulations to, first, provide an overview of the main patterns governing the mesoscale circulation in the Alboran Sea over the analyzed period and, secondly, show the transition towards non-balanced submesoscale dynamics that emerge as the model resolution is increased.

4.1 Data

The nested WMed1500 and Alb500 solutions span from years 2010 to 2013. For confidence in the achievement of numerical stability, the spin up period is extended to one year in both solutions (see Section 2.1.2), therefore the dataset used for this study is reduced to the last three years. Data analysis is performed from two different perspectives:

- First, we use the last year of daily averaged data from the parent and/or child solutions to provide an overview (a mean characterization) of the main circulation patterns in the Alboran Sea, although interannual and seasonal variability over the full 3-year period is also briefly analyzed and discussed.
- Secondly, the transition towards the submesoscale is explored through the analysis of specific statistics using the Alb500 solution.

These are the subject matters of the current chapter. Following this, a selection of submesoscale events is further studied in Chapter 5.

4.2 Mean circulation

As a first step, we use the first baroclinic Rossby radius, R_1 , as an estimate of the lower limit for mesoscale motions in the Alboran Sea provided by our model (see Appendix A). From the monthly means of R_1 computed from the WMed1500 simulation, the regional characterizations over two representative months of the winter (February) and the summer (August) seasons, during which the minimum and maximum values of R_1 are obtained, is shown in Figure 4.2. Because R_1 is proportional to the depth of the water column, the low values in shallow waters near coastal shelves are to be expected, as well as the largest radii encountered in the deepest regions of the domain. Besides

the spatial variability associated with changes in water depth, the largest values in both seasons are centered around 36°N , 4.5°W , showing the signature of the WAG. As will be shown in the next sections, this gyre displays a strongly stratified structure, trapping fresh AW coming directly from the AJ in the upper layers (0-150 m) and much denser MW below, down to 700 m or deeper. Strong vertical density gradients are thus to be expected in the pycnocline, resulting in large R_1 values in this area. The same argument applies for the high values observed around 35.7°N , 2°W during August (reflecting the AW trapped inside a transient and less intense eastern gyre) or along the path of the Algerian Current (starting in front of the coast of Oran, at 35.7°N , 1°W). Seasonal variability is also evident, with a widespread increase over the summer, as expected from the fact that stratification is reduced in winter by wind-induced mixing.

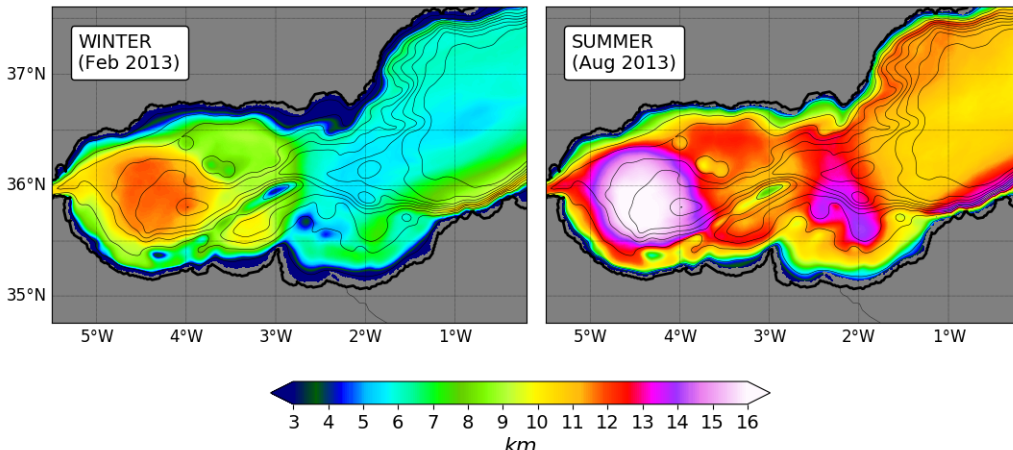


Figure 4.2: Regional characterization of the Rossby first radius of deformation, R_1 , in the Alboran Sea for winter (February 2013, left panel) and summer (August 2013, right panel) obtained from the WMed1500 simulation. Bathymetry lines are contoured in black every 300 m.

Notwithstanding the different model configurations, R_1 values in the Alboran Sea from the WMed1500 simulation are consistent with those obtained from the ROM-SWMED32 solution (see Section 1.5 and Figure 1.5).

In the following sections, the coarser WMed1500 solution provides an overview of the surface mesoscale circulation in the Alboran Sea and its variability over the integration period of the model. The vertical structure of variables involving 3D fields (*e.g.*, vertical velocities, energy fluxes) are obtained using the finer Alb500 simulation, constituting a preliminary step towards an extensive analysis of the submesoscale processes

which is carried out in Chapter 5.

4.2.1 Surface mesoscale circulation

Figure 4.3 shows SSH (top), the derived surface geostrophic velocity field (middle) and surface salinity (bottom) averaged over year 2013 from the WMed1500 solution. The WAG is the main pattern, with large SSH values persisting over the full period. The SSH gradient coincides with an analogous salinity gradient, showing the transition (around 37.0) between incoming fresh AW that flows eastward along the African coast and resident MW to the north. This is the most common surface pattern over the model period, as seen from the monthly-averaged SSH series over years 2011–2013 shown in Figure 4.4. The double gyre system, with the signature of both the WAG and the EAG, is only present in this solution ON two occasions over the full sequence: from early summer to early autumn in 2011 (June–October) and during autumn 2013 (September–November). In both events, a well defined and strong AO front separates the fresh AW from the much denser MW, with an especially sharp contrast from early autumn, when the surface MW shows its highest salinity levels due to large summertime evaporation rates (Figures 4.5 and 4.6).

Monthly patterns of surface KE in 2013 are shown in Figure 4.7. While KE is mostly concentrated in the WAG during the summer season, there is a widespread energy increase in the cold months that leads to a more variable pattern: the branch of the Atlantic inflow that flows towards the Algerian Basin intensifies, sometimes closer to the African coast and evolving into the Algerian current or, in other cases, following a more or less intense EAG (*i.e.*, during the autumn 2013 two-gyre event). This behavior agrees with the time evolution of the area averaged KE in Figure 2.3 with peak values in winter, coinciding with a more general pattern, and then decreasing towards minimum energy levels in summer.

4.2.2 3D structure

The 3-dimensional structure of the Alboran Sea circulation is described using the last year of available data from the Alb500 solution (December 2012 to November 2013). This characterization includes maps at several representative depths and vertical sections at key locations (indicated in Figure 4.8), setting the background for

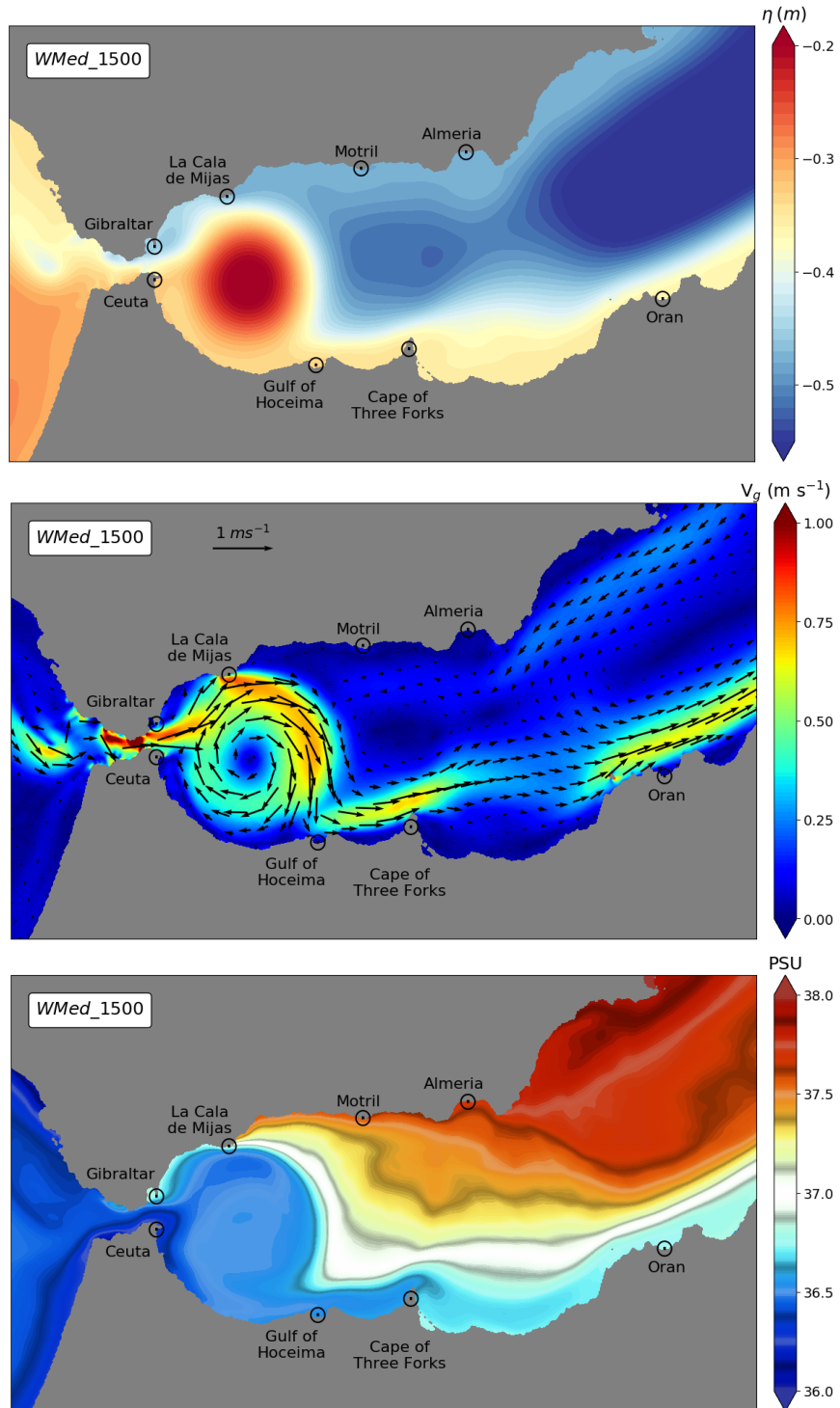


Figure 4.3: Mean SSH (top), geostrophic velocity (middle) and surface salinity (bottom) averaged from the WMed1500 solution for year 2013.

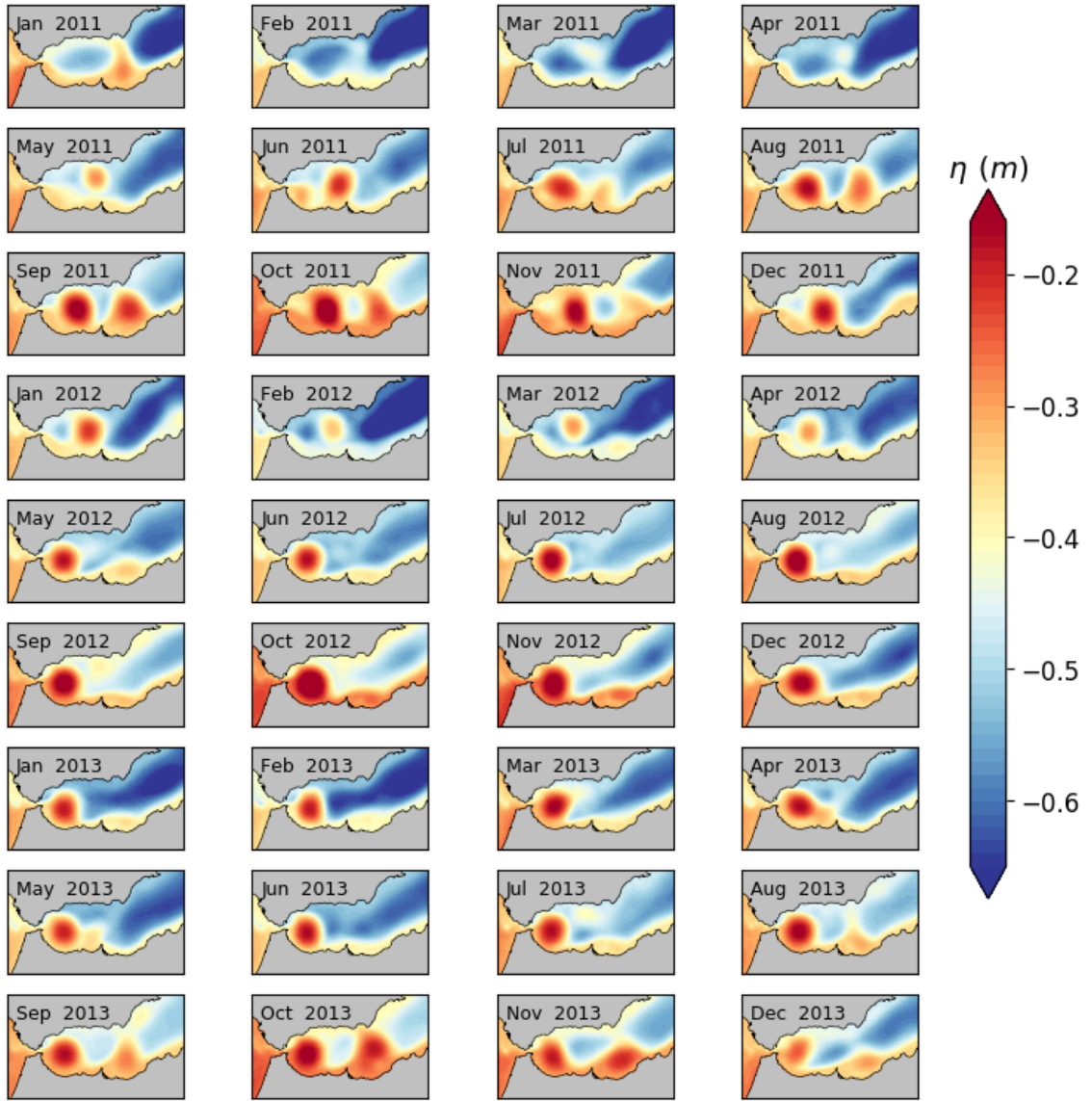


Figure 4.4: Monthly averaged SSH for years 2011 to 2013 from WMed1500.

understanding the potential SMCs generation mechanisms in this region.

As stated in Section 1.5, 3D dynamics in the Alboran Sea can be roughly interpreted as a two layer system, composed of two principal water masses: the incoming surface fresh AW and the underlying dense Mediterranean outflow. Figure 4.8 shows the time averaged salinity structure at the surface (top) and in a vertical zonal section crossing the basin at 36°N (bottom). The salinity pattern is dominated by the presence of the WAG and by the effect of the salinity jump at the eastern side of the SoG. There is no signature of the EAG in this yearly averaged structure, as this was only perceptible

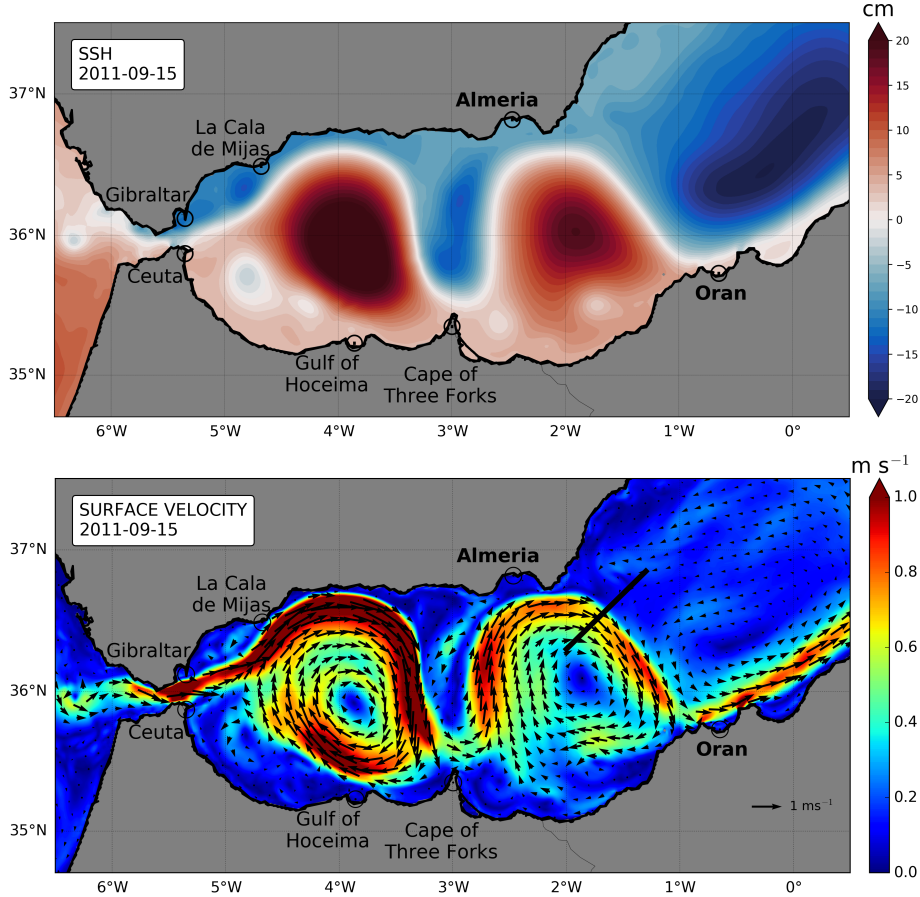


Figure 4.5: Daily averaged SSH (top) and surface velocity (bottom) during a "two-gyre event" detected in summer-autumn 2011. The black thick line crossing the AO front corresponds to the salinity section shown in Figure 4.6. Data correspond to September 15, 2011 from the WMed1500 solution.

during the first month of the sequence (December 2012). The salinity profile along this section averaged for this month, shows the presence of both gyres (Figure 4.9).

The mean circulation is represented in Figure 4.10, showing vertical profiles of the zonal velocity component in the downstream (mainly eastward) direction (top panels) and their corresponding salinity distributions (bottom panels). These sections correspond to meridional slices at key locations in the route of the Atlantic and Mediterranean waters across the Alboran Sea (indicated in Figure 4.10, top): Strait of Gibraltar (left); the center of the WAG (middle); and a section near the Almeria headland (right):

- The Strait of Gibraltar section reveals a strong incoming Atlantic Jet, flowing

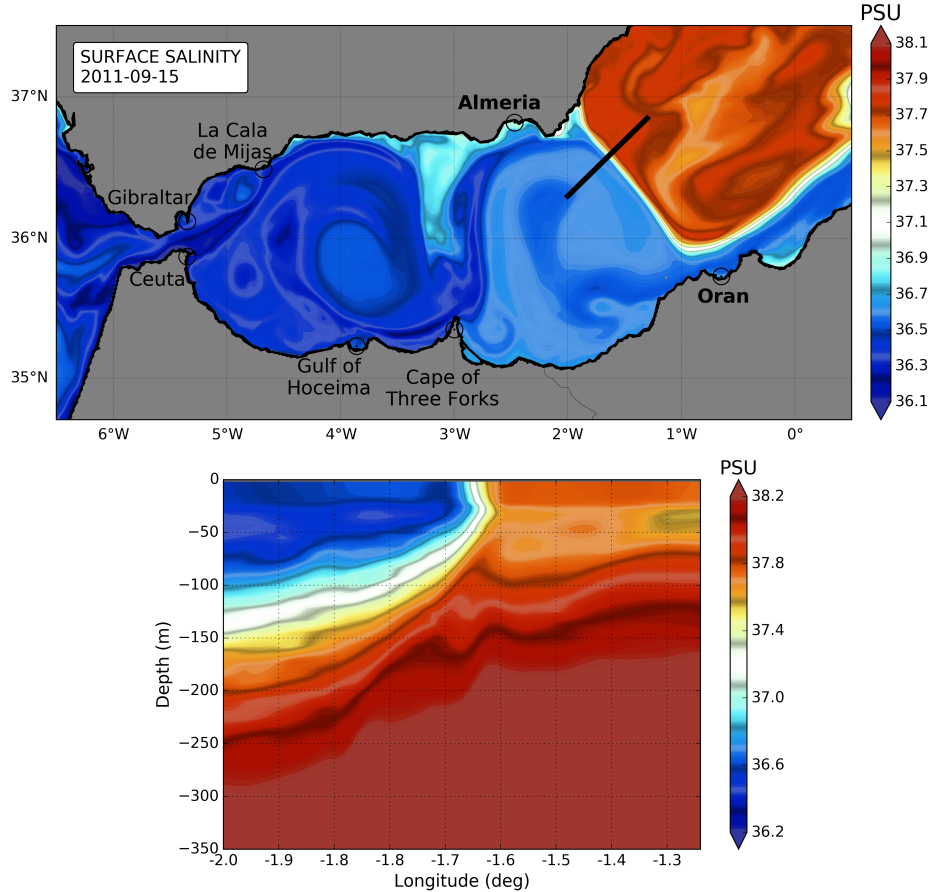


Figure 4.6: Daily averaged surface salinity (top panel) during a "two-gyre event" detected in summer-autumn 2011. The black thick line crossing the AO front corresponds to the salinity section shown in the bottom panel. Data correspond to September 15, 2011 from the WMed1500 solution.

close to the African coast and extending down to 150 m depth (red area). The zero velocity contour (white region) represents the transition between the fresh Atlantic inflow (eastward) and the denser Mediterranean outflow (westward), located around the 38.2 isopycnal surface (marked with a thick black line). The salinity profile confirms the vertical distribution of the two water masses.

- The transition between the two water masses is still noticeable in the meridional section crossing the WAG. Here, the velocity dipole does not correspond to an inflow/outflow pattern: it reveals the presence of a strong, deep anticyclonic gyre trapping the fresh Atlantic waters in the upper 200 m and also the denser Mediterranean waters down to 700 m or deeper. In this figure, the Mediterranean outflow traveling westward towards the Strait corresponds to the light blue area

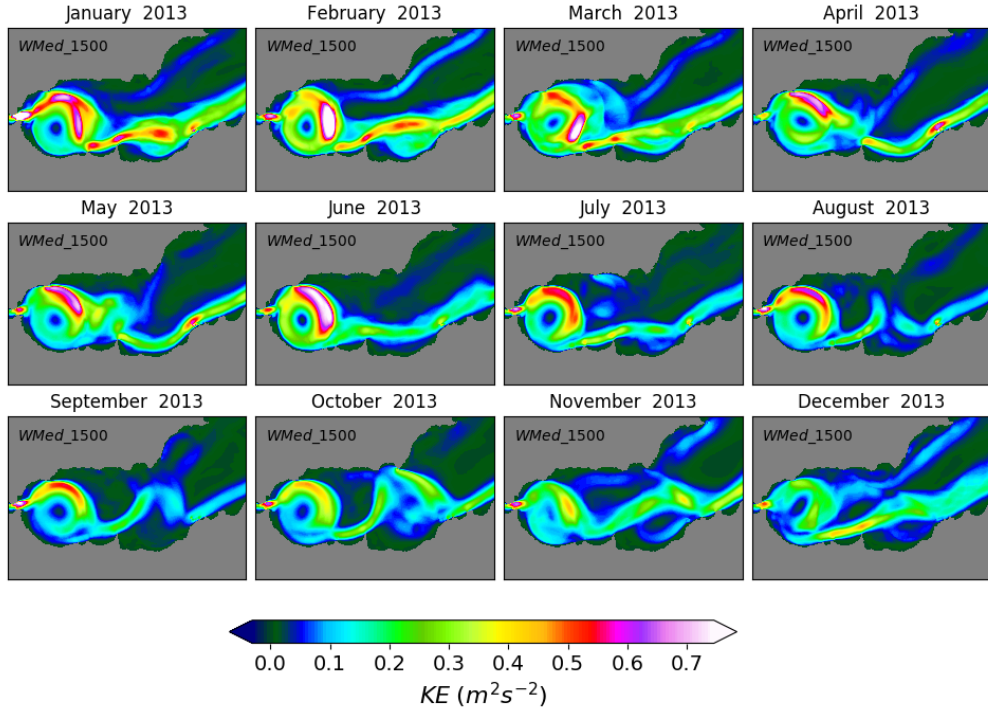


Figure 4.7: Monthly averaged surface KE for year 2013 from WMed1500.

depicted close to the Spanish coast (around 36.4°N) and centered at 400 m depth. An extended analysis considering monthly averages of 3D velocity and salinity fields (not shown) reveals the prevalence of this structure, with the WAG mostly present throughout the year. The main difference over the monthly sequence lies in the stratification pattern (reflected in the pycnocline profile) showing enhanced surface mixing during the winter months and strong stratification over the summer and early autumn seasons.

- In the easternmost section, the salinity contours reveal a region dominated by modified (saltier) AW. The low mean velocity values are a reflection of the seasonal variability in the circulation: while the EAG is present during early winter, from early spring the situation turns into a winding "near-coastal current regime" in which the residual of the incoming Atlantic current flows eastwards along the African coast (the red area in the velocity profile). The presence of this near-coastal jet is also revealed by the marked tilting of the isopycnals in the upper 200 m, around 35.5°N. The MW circulates westward along the northern half of the region, with the main current located around 250 m depth and 36.5°N. Monthly means in this section (not shown) also reveal strong surface mixing in winter

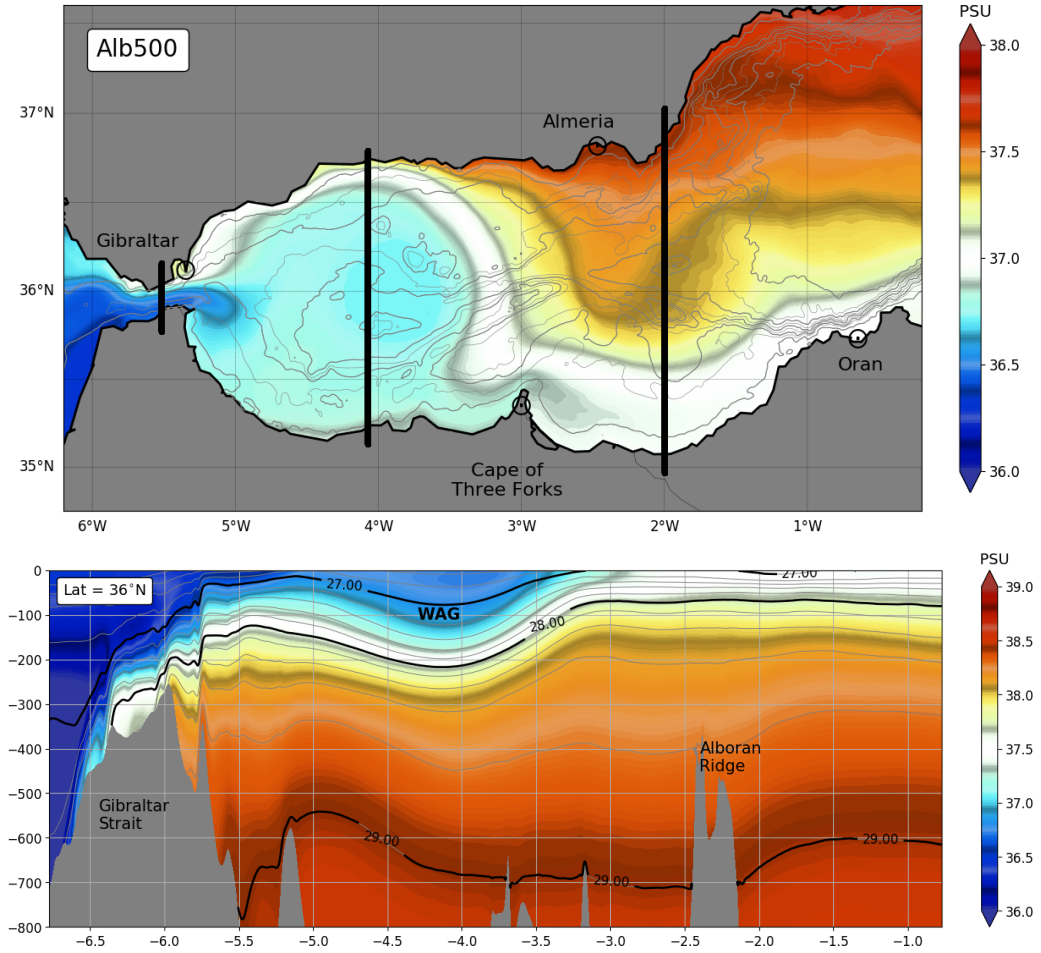


Figure 4.8: Top: Surface salinity averaged over the last year of data from Alb500 (December 2012 - November 2013). Black vertical lines correspond to the vertical sections depicted in Figure 4.10. Bottom: A zonal vertical salinity section along latitude 36°N averaged over the same period. Contours of potential density are spaced every 0.2 kg m⁻³.

against a marked stratification within the uppermost layers over the summer and early autumn months.

From the vertical distributions depicted in Figure 4.10, the paths followed by the Atlantic inflow and the Mediterranean outflow over this period are characterized at key depths of 20, 150 and 400 m and along the representative months of December, April and August (Figure 4.11).

- Circulation in the upper layers ($z = -20$ m) is dominated by the presence of fresh AW, which can extend down to a mean depth of 150 m, just above the

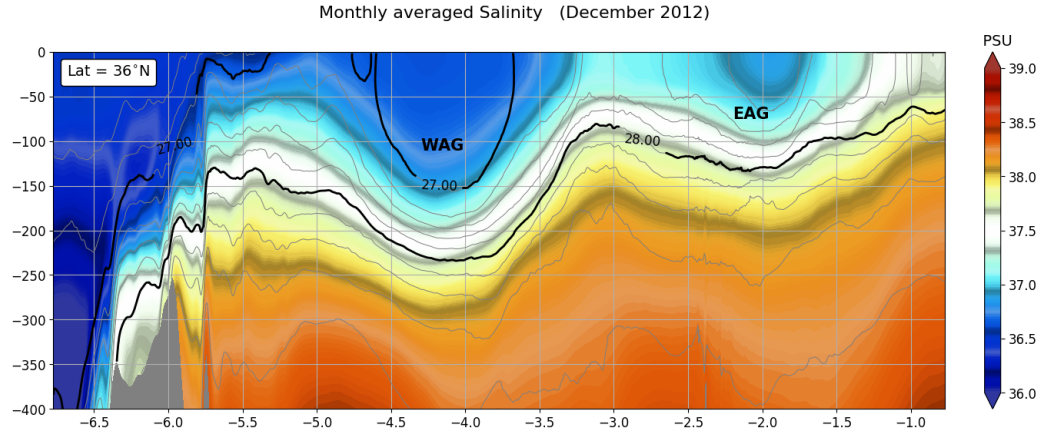


Figure 4.9: Monthly averaged salinity in a zonal vertical section for December 2012 at 36°N from Alb500. Contours of potential density are spaced every 0.2 kg m⁻³.

transition layer (marked by the 28.2 isopycnal in Figure 4.10) or even deeper in the center of the WAG. The main circulation patterns are: (1) the strong AJ, with surface velocity maxima exceeding 1 m s⁻¹ throughout the year; (2) a persistent WAG, with surface velocity enhanced at the NE edge, just after the main stream detaches from the Spanish coast; (3) the residual African branch of the Atlantic inflow, depicting a more complex route, sometimes flowing eastward along the African coast and merging into the AC, and other times forming a meandering pattern or even a closed gyre (the marked EAG along December 2012). (4) The weak flow entering the domain from the NE corner shown in April 2013 (and also, although much less intense, in August) corresponds to a residual branch of the NC after crossing the Ibiza Channel.

- At the representative depth of $z = -150$ m the circulation is slightly different than the patterns observed in the top layer: the salinity fields show a major abundance of MW, although the AW remains trapped in the still strong WAG (and in the EAG, when present). In the velocity maps we find a weak AJ signal, while the intensity of the two gyres persists and the signature of the NC (center and right panels) is more intense.
- As shown in Figure 4.10, the main current of the Mediterranean outflow flows at a mean depth of $z = -400$ m. Salinity at these levels is above 38.0, and the circulation patterns differ considerably from the upper layers. What we see here is the circulation of the Mediterranean outflow. The connection with the velocity fields from the upper layers is (1) the anticyclonic circulation in the two gyres,

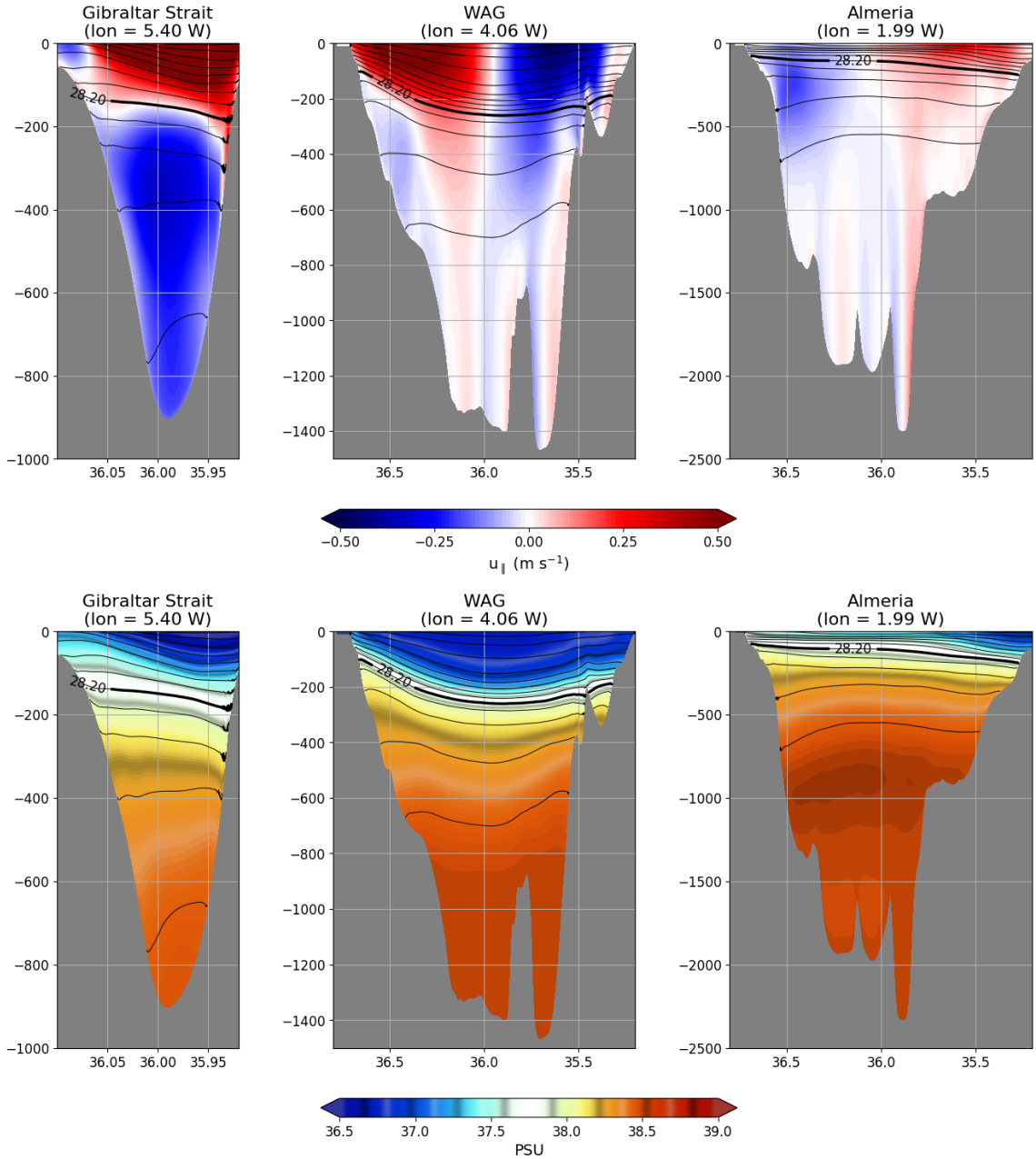


Figure 4.10: Vertical sections along the longitude lines indicated in the top panel in Figure 4.8 of zonal velocity (top) and salinity (bottom) obtained from Alb500 yearly averaged data (December 2012 - November 2013). Contours of potential density are spaced every 0.2 kg m^{-3} . The thick black line corresponds to the 28.2 isopycnal.

and (2) the strengthening of the NC with depth (carrying the MW and LIW from the North). In contrast, the AJ has been replaced by a relatively strong outflow of dense MW (with mean speeds up to 30 cm s^{-1}) flowing along a preferred path near the NW Spanish coast.

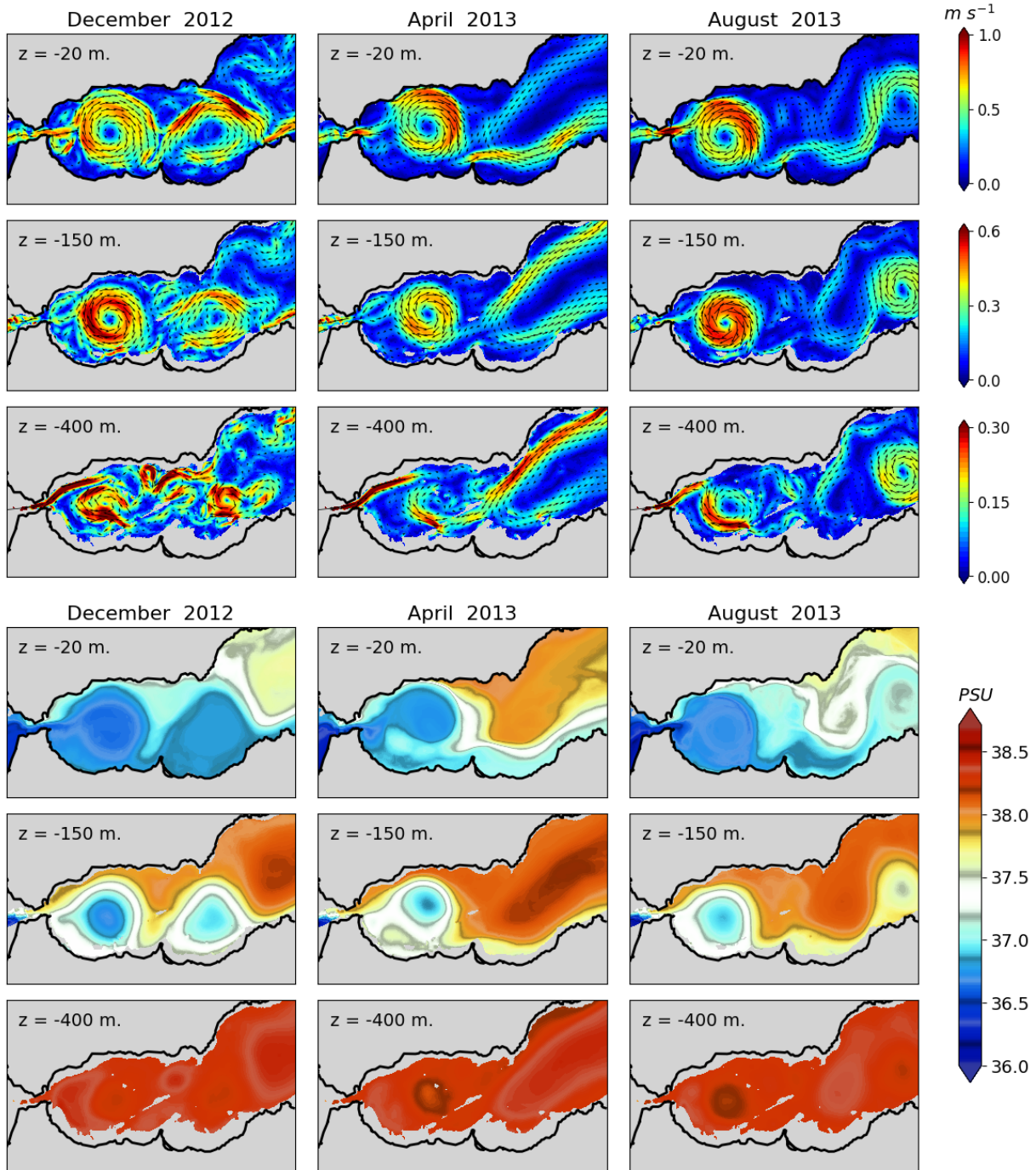


Figure 4.11: Top: Monthly averages of model velocity from Alb500 at selected depths: 20, 150 and 400 m. Note that color bar ranges are different for each depth. Bottom: Salinity patterns corresponding to the velocity maps above.

These results highlight the significant role of the "two-layer" arrangement, in combination with the complicated bathymetry, in the Alboran Sea dynamics.

4.3 The submesoscale transition

Although the instantaneous surface vorticity fields from the WMed1500 solution can achieve Ro numbers of $\mathcal{O}(1)$ in specific regions (Figure 4.1), the *submesoscale soup* only emerges in the nested Alb500 simulation, where the spatial and temporal resolution of the output fields is increased up to 500 m and 3-hourly averages, respectively. Figure 4.12 shows examples of the surface vorticity fields obtained from our three available datasets: WMed1500 daily averages (top), Alb500 daily averages (middle) and Alb500 3-hourly averages (bottom). Besides the improvement of the spatial characterization with increasing Δx (top and middle panels), the availability of a time resolution of several hours against daily averages significantly enhances the detection of SMCs (bottom panel) and, furthermore, allows the tracking of their evolution (as shown in Chapter 5).

4.3.1 The surface signature of SMCs

KE and EKE

The first signs of submesoscale activity in the Alboran Sea appear in the mean surface KE and EKE fields depicted in Figure 4.13, averaged over the last two years of the simulated period. While the KE map (top) shows a well defined WAG and a less intense signature of the EAG, the EKE characterization (bottom) reveals the large variability of both structures: the fluctuations in the incoming direction of the AJ, alternating from NE to SE; the variable size and position of the WAG; or the path followed the Atlantic current from Cape Three Forks, flowing northeastward towards Almeria (forming the EAG), or flowing eastward along the African coast. From the EKE seasonal averages in Figure 4.14, winter and spring show the largest EKE values, revealing large submesoscale activity over the cold seasons (presumably reinforced by enhancement of surface mixing).

Vorticity statistics

While in quasigeostrophic (QG) dynamics a cyclonic-anticyclonic symmetry is expected in the mesoscale vorticity field (Chelton et al., 1998), the enhancement of horizontal buoyancy gradients and the dominating turbulent thermal wind balance in the

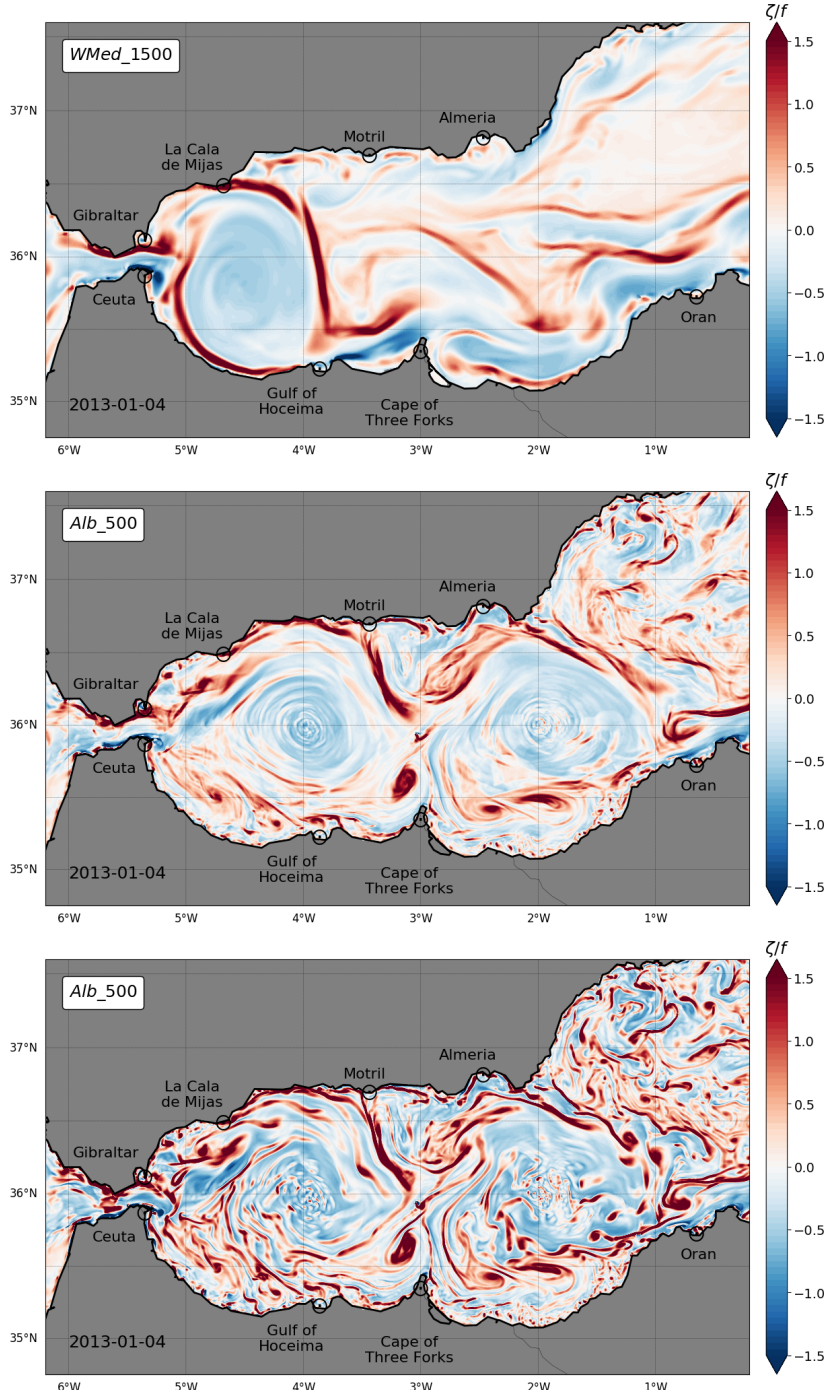


Figure 4.12: Maps of surface ζ/f for different available spatial and temporal resolutions: daily averaged WMed1500 (top), daily averaged Alb500 (middle) and 3-hourly averaged Alb500 (bottom). The *submesoscale soup* can only be observed in the highest resolution combination. Maps correspond to January 4, 2013, when both the WAG and EAG were present in the Alb500 solution, while not in WMed1500.

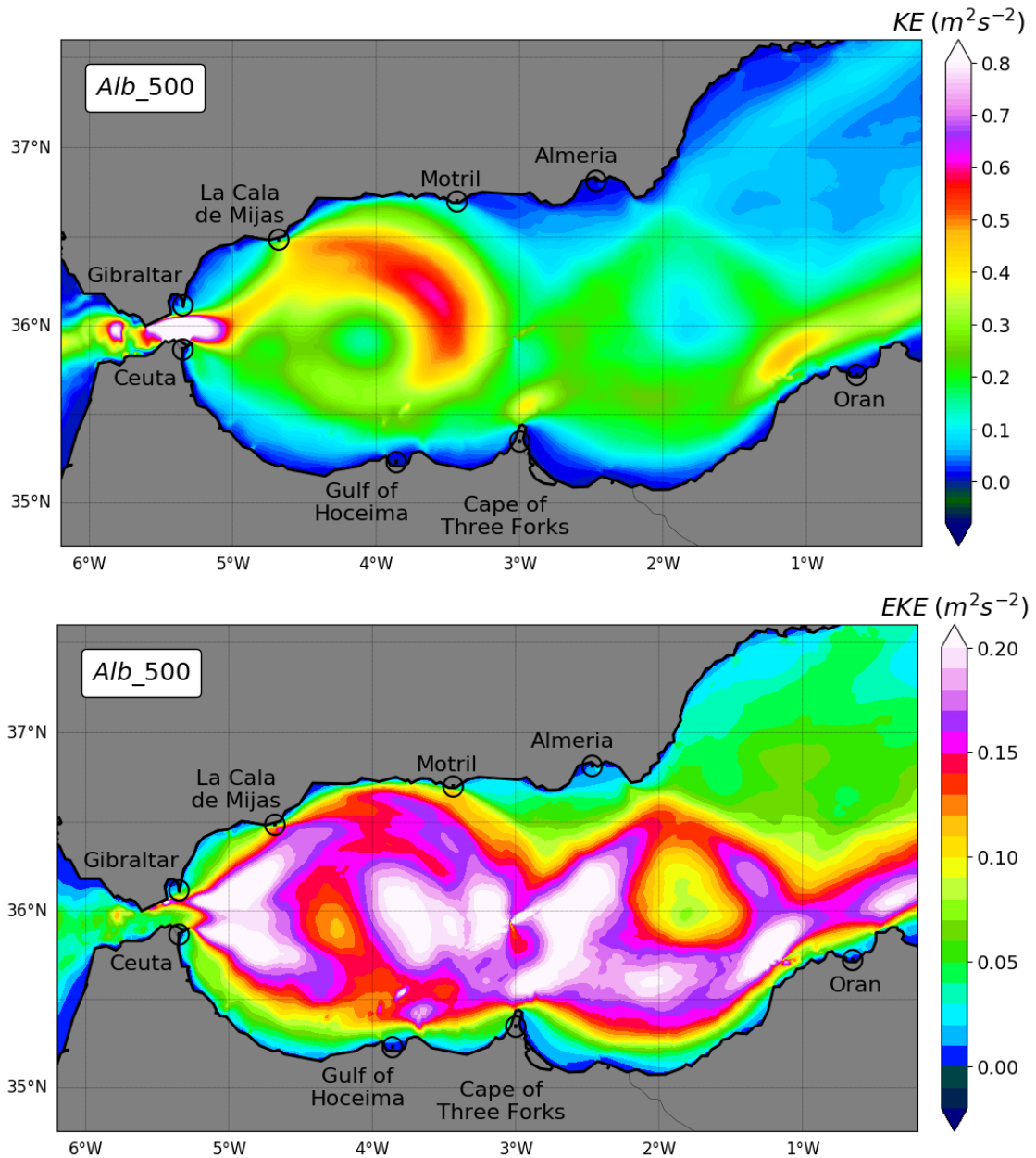


Figure 4.13: Mean KE (top) and EKE (bottom) from the last 2 years of the Alb500 solution (in $m^2 s^{-2}$). EKE is computed from anomalies of the horizontal velocity components (u' and v') with respect to their corresponding time means over the full analyzed period (\bar{u} and \bar{v}).

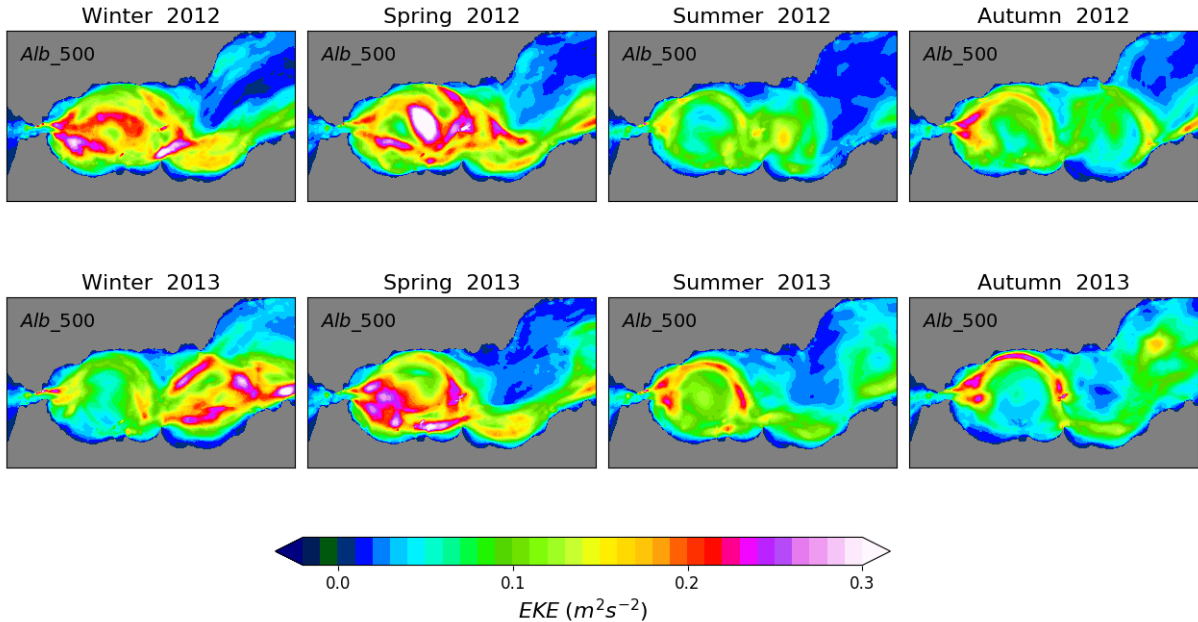


Figure 4.14: Seasonal averages of surface EKE for years 2012–2013 from Alb500 (in $m^2 s^{-2}$). EKE is computed from anomalies of the horizontal velocity components (u' and v') with respect to their corresponding time means computed over each season (\bar{u} and \bar{v}).

SMCs (see Section 1.2) distorts these metrics.

Ertel's potential vorticity (PV; Hoskins, 1974), defined as the dot product between the absolute vorticity (see Appendix B) and the density (or buoyancy) gradient, is a useful magnitude used to quantify the role of relative vorticity in the stability of a current. Ertel's PV conservation theorem states that, in adiabatic motions, water parcels flowing along isentropic surfaces conserve Ertel's PV. Considering the vertical component of PV,

$$q = \frac{1}{\rho_0} \frac{\partial \rho}{\partial z} (\zeta + f), \quad (4.1)$$

in rapidly rotating fluids with $|\zeta| \approx f$, conservation of PV entails that cyclonic vorticity is preferred (Hoskins and Bretherton, 1972). According to Equation (4.1), if we assume an initial state with symmetric stability and negligible ζ , the condition $\zeta > f$ must be accomplished so that absolute vorticity remains positive (Rudnick, 2001; Shcherbina et al., 2013). This is generally observed in the upper ocean, where there is greater occurrence of currents with $\zeta/f \sim \mathcal{O}(1)$. In deeper layers, where usually $|\zeta| < f$, vorticity skewness has no preferred sign (*e.g.*, in a submesoscale model approach of the California Undercurrent, Molemaker et al. (2015) find greater abundance of anticyclones with

a peak amplitude of $\zeta \approx -0.7f$ at $z = 150$ m).

Temporal statistics of the surface vorticity from our Alb500 simulation at seasonal scale are displayed in Figures 4.15. The vorticity field reveals the persistence of the WAG dominating the western half of the basin (Figure 4.15, top). The largest $|\zeta|/f$ values are seen along the path followed by the Atlantic inflow, especially when the current interacts with topographic obstacles: both sides at the exit of the SoG, at the northern edge of the WAG along the Spanish coast (generating cyclonic vorticity) or when impacting against the African coast (*e.g.*, the negative vorticity generated downstream of Cape Three Forks and the Oran headland). Large vorticity amounts persist around the gyres in the open ocean, mainly associated with frontal regions, suggesting enhancement of the strain field as an onset of frontogenesis. As in the previously analyzed KE/EKE fields, the larger rms variability is found during the cold seasons (Figure 4.15, middle). The skewness patterns reveal a predominance of cyclonic vorticity generation, as expected from PV conservation, with a spatial distribution that reinforces the theory for topographic and frontogenetic origin (Figure 4.15, bottom).

4.3.2 Energy fluxes

The nature of submesoscale instabilities can be examined by looking at the sources of the eddy energy, in a similar way as in the LEC analysis carried out in Chapter 3.

MLI and frontogenesis are recurrent submesoscale processes in the Alboran Sea. Their associated perturbations act to restratify the mixed layer, and are mediated by a conversion from eddy potential to eddy kinetic energy through vertical buoyancy fluxes ($P_e \rightarrow K_e$, or baroclinic instabilities). On the other hand, enhancement of horizontal shear in the mean current is a principal energy source in the topographic vorticity generation mechanism (barotropic instabilities). The interaction with a topographic obstacle decelerates the flow and kinetic energy is transferred to the eddy field with the subsequent perturbation growth. Then, eddies are diluted by the background shear (Orr, 1907) and return the energy to the mean flow ($K_m \rightarrow K_e$; Gula et al., 2015b).

The complicated dynamics in the Alboran Sea, with strong currents confined within a relatively small basin with complex bathymetry, suggest that eddy generation mechanisms in this region can not be considered separately, but rather involve a mixed

baroclinic and barotropic origin.

In order to identify the regions affected by any of these instability types and to analyze their seasonal variability, we compute an estimation of the energy conversion terms $D(K_e)$ and $M(K_e)$ defined in Equations 3.12 and 3.15, respectively, using the last year of data (2013). Here, at each point and for a given month, we define the mean variable field as the monthly average, while the eddy components are the deviations from the monthly mean. The vertical integration is confined to the upper 100 m, as we can consider contributions from deeper layers to be negligible, and also to avoid the intrusion of the Mediterranean outflow in the interpretation of the $M(K_e)$ conversion.

The monthly evolution of the baroclinic conversion term, $D(K_e)$, is shown in Figure 4.16. The largest conversion rates take place along the SoG. Even though this is barely perceptible, the narrowest section of the Strait is dominated by a dipole pattern of alternating $P_e \leftrightarrow K_e$ conversions, triggered mainly by the effect of bathymetry and tides. The sensitivity of $D(K_e)$ to bottom bathymetry is perceptible throughout the basin over the full sequence with more or less intensity (*e.g.*, over the Alboran Ridge). The slightly red background field dominating the region is intensified during the cold months (January–March and November), due to enhanced winter mixing. Besides the large values within the SoG, the strongest signature appears along the track of the incoming Atlantic current, especially in the frontal regions where the two water masses (AW and MW) meet: at the eastern edge of the WAG, and from Cape Three Forks towards the Algerian basin, mostly visible during February and March; in January, larger instabilities appear around the signature of the EAG and the associated AO front, which dominate the circulation in the eastern basin over this winter season (see Figure 4.11, top left pannel).

Barotropic instabilities are shown in Figure 4.17. Again, larger values are found within the SoG, with a dipole pattern on the Altantic side, in contrast to strong EKE generation through $K_m \rightarrow K_e$ conversion at the eastern exit of the Strait, where the AJ meets the open basin and turbulence arises. Over the WAG, areas with negative $M(K_e)$ at the upstream side of the main topographic obstacles, where intensified horizontal shear inhibits perturbation growth (*e.g.*, Cala de Mijas or Cape Three Forks), are followed by positive $M(K_e)$ on the downstream side, where the current becomes unstable and transfers energy to the eddy flow.

4.4 Discussion

In our nesting approach, SMCs arise in the finer solution, when resolution is increased to $\Delta x = 500$ m and output fields are stored as 3-hourly averages. Strongest submesoscale activity is registered along the track of the Atlantic inflow (AJ, WAG, AO front, etc.) and a marked positive skewness in the surface vorticity field shows a clear predominance of cyclonic vorticity, an indicator of the submesoscale regime, against the cyclonic-anticyclonic symmetry predicted by the QG theory. The regional characterization of the energy conversion terms reveals that eddies can be mainly generated by the interaction of the mean flow with topography through barotropic shear instabilities, or via baroclinic instabilities arising during the mixing processes in the boundary layer (winter mixing) and in the development of frontogenesis. These mechanisms, TVG and FG, are further examined in the next chapter using the Alb500 solution.

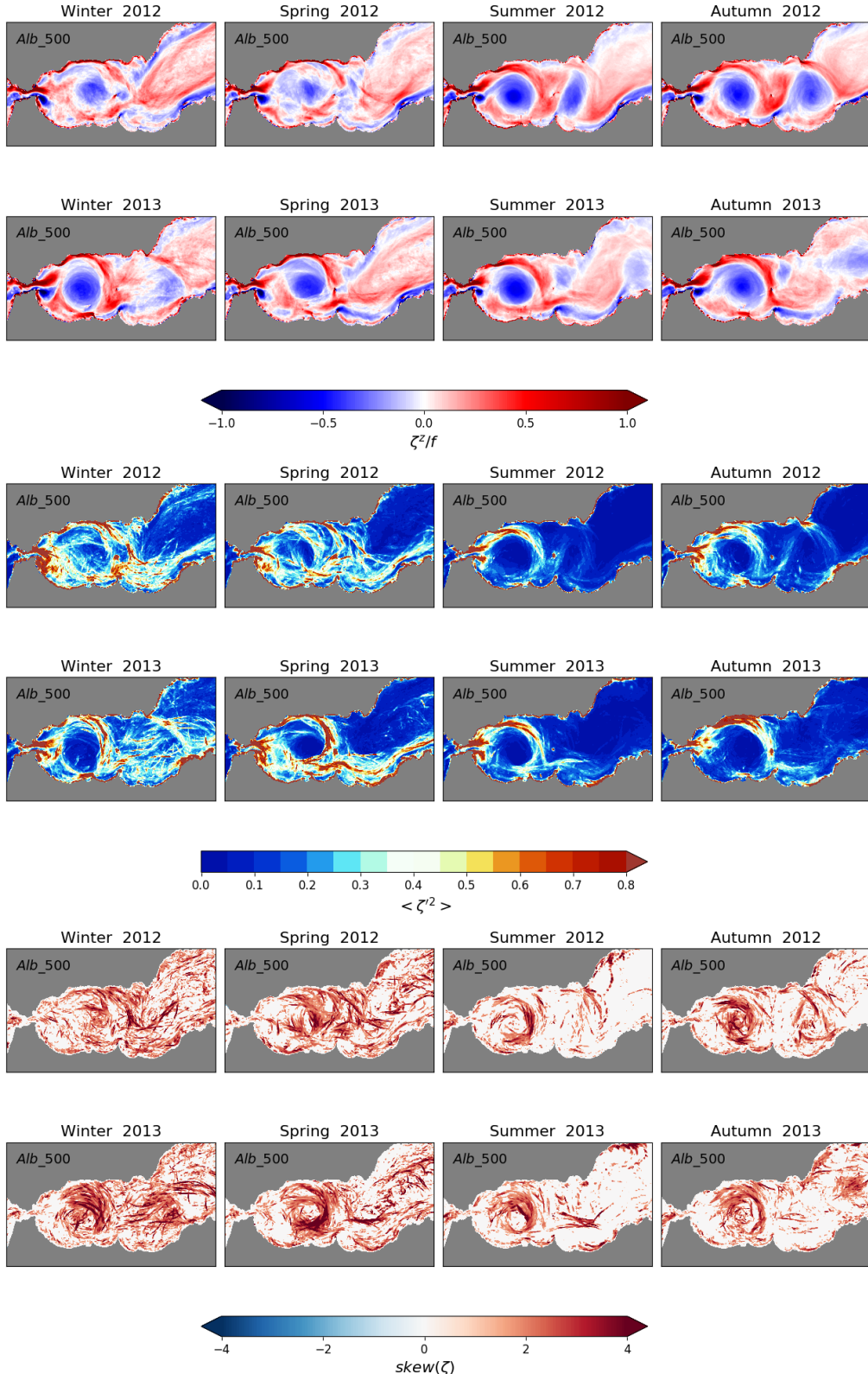


Figure 4.15: Seasonal averages of surface ζ/f (top); rms variability, $\langle \zeta'^2 \rangle$, (middle) and skewness (bottom) over the last 2 years (2012–2013) of the Alb500 simulation.

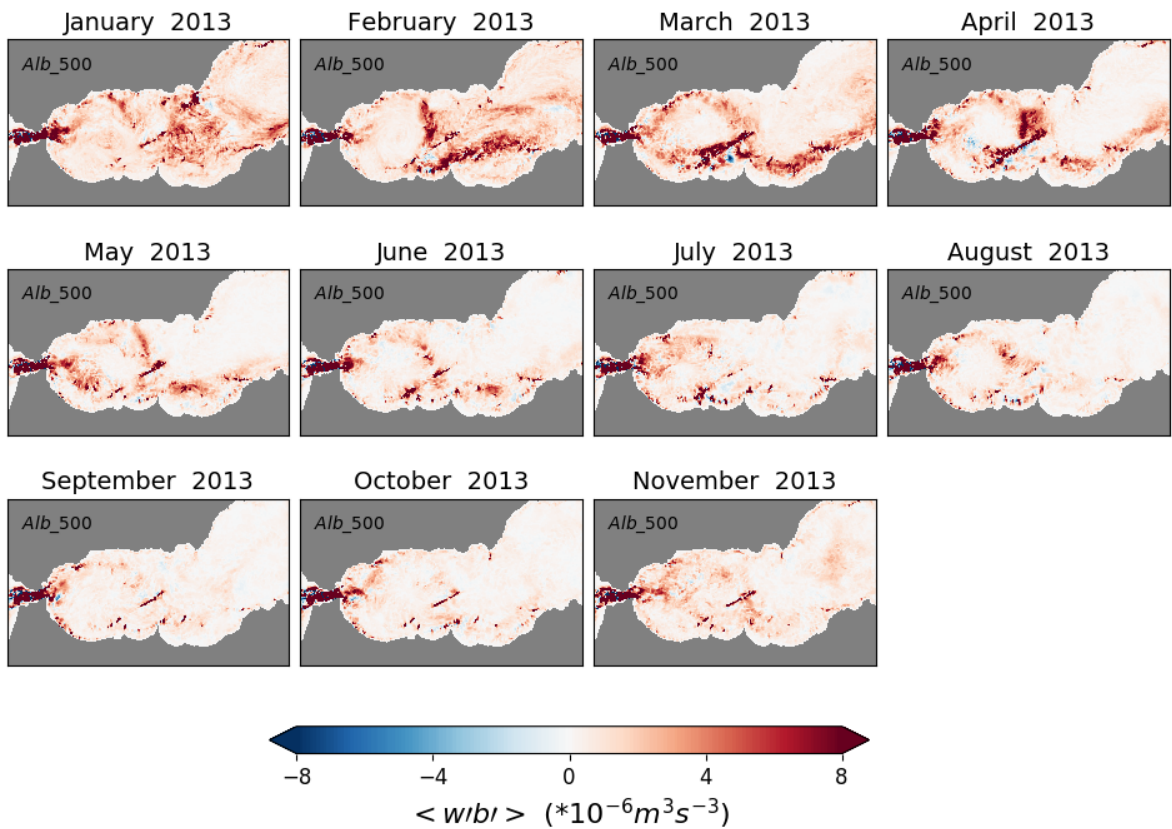


Figure 4.16: Monthly evolution of the vertical buoyancy flux ($P_e \rightarrow K_e$, or $D(K_e)$ conversion term) integrated along the top 100 m. Positive values indicate the areas of perturbation growth through baroclinic instabilities.

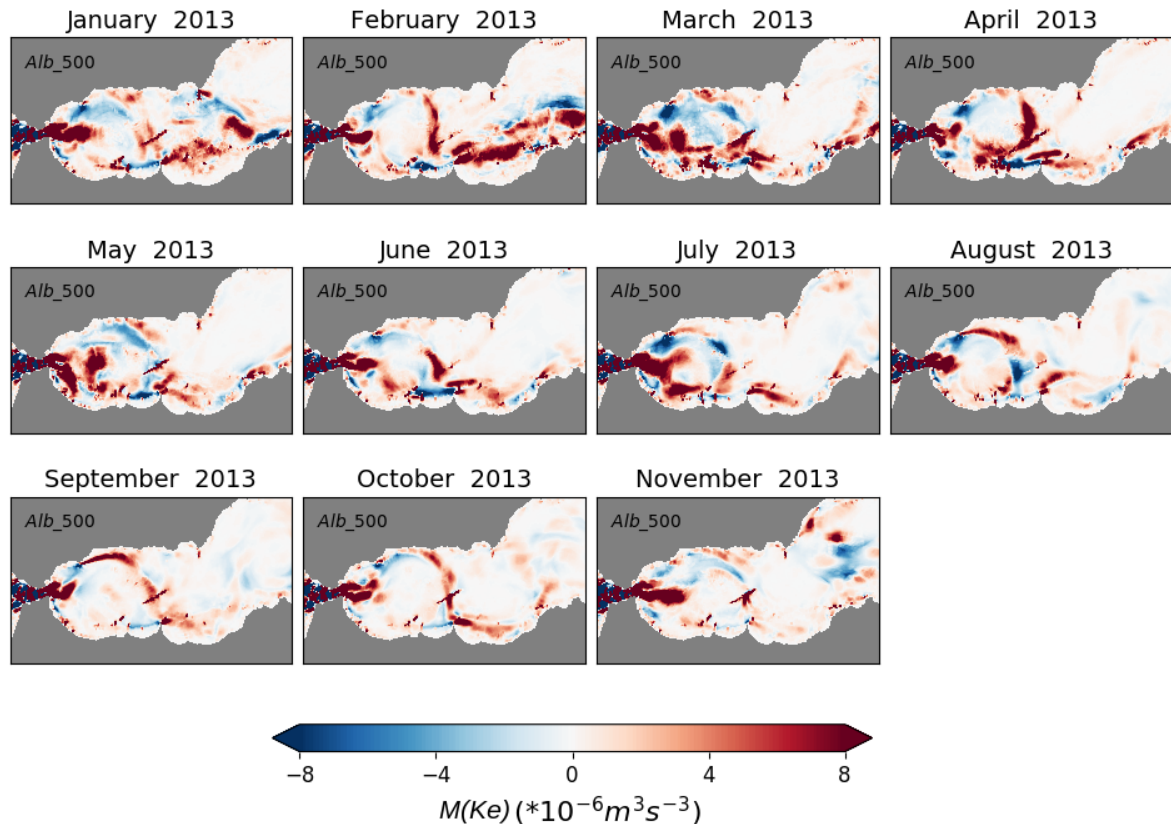


Figure 4.17: Monthly evolution of the barotropic conversion term ($K_m \rightarrow K_e$, or $M(K_e)$) integrated along the top 100 m. Positive (red) values indicate conversion from mean to eddy kinetic energy as a result of horizontal shear instability.

Chapter 5

Submesoscale processes

Results obtained in the previous chapters suggest that topographic vorticity generation and frontogenesis are two principal mechanisms responsible for generation of SMCs in the Alboran Sea. Based on the analysis carried out in Chapter 4, these mechanisms occur primarily around the path followed by the incoming AW in the Alboran Sea and are presumably motivated by three main factors: (1) the strength of the Atlantic current, in contrast with (2) the size and shape of the basin, and (3) the clash with resident MW.

The objective of this chapter is, first, to show the capability of the Alb500 simulation to reproduce SMCs in the Alboran Sea and, second, to describe and quantify the mechanisms of TVG and FG and the roles they play in the Alboran Sea dynamics.

The occurrence of TVG and FG in our simulation does not display a clear spatial nor temporal variability which facilitates the identification of events for an in-depth study. From the statistical analysis given in Chapters 3 and 4 we can get an estimate of the areas in which such episodes most frequently occur, although an accurate description and quantification of the processes (sometimes lasting just a few days) involves a more rigorous selection.

To this aim, the Alb500 solution has been explored in order to create a catalogue of potential, well-defined "submesoscale events". The primary screening of TVG and/or FG events is based on a visualization of the sequence of 3-hourly averaged surface vorticity fields from the Alb500 solution. A subsequent finer selection is done after contrasting the preselected events with the corresponding surface salinity, density and divergence fields, and considering other criteria such as the duration of the events and

their recurrence along the simulation period.

The process comes with a set of prevalent and typical regimes which can be considered as representative of the Alboran Sea submesoscale dynamics.

5.1 Topographic vorticity generation

TVG consists of the dissipative interaction of the geostrophic flow against bottom topography. This process is typical in strong currents that flow along sharp bathymetric slopes and interact with a topographic obstacle; the subsequent current separation leads to offshore injection of the strong potential vorticity generated by enhanced horizontal shear against the slope.

Dynamically, the interaction of the flow with topography can be described in terms of form drag, the force resulting from bottom pressure differences across an obstacle (Molemaker et al., 2015; Gula et al., 2015a). As a current flows along a sloping shelf with topographic irregularities, inertia is balanced by pressure forces against the bottom and the current is forced to flow around the obstacles, following contour lines of constant depth. A positive bottom pressure anomaly, p_b , on the upstream side of the obstacle retards and diverts the flow, while a downstream negative p_b keeps the current attached to the coast as it flows along the isobaths. In this context, the process of current separation from the coast can be interpreted as a combination of a strong positive p_b upstream of the obstacle, and the absence of a compensating negative p_b downstream which overcomes inertia, resulting in the detachment of the flow from the coast.

In the Alb500 simulation we find recurrent TVG events primarily in these areas (Figure 5.1):

- At both sides of the exit of the SoG, where the AJ interacts with the north/south corners of the Strait, generating very strong cyclonic/anticyclonic vorticity, respectively.
- Along the northern edge of the WAG, especially when the AJ enters the Alboran Sea directed toward the Spanish coast. A narrow band of strong positive vorticity develops as the current flows eastward along the coast. When the flow passes the sharp topographic obstacles between Cala de Mijas (CM) and Motril (Mo),

separation occurs and cyclonic vorticity is advected offshore. The same situation frequently extends along the coast between the Mo and west Almeria (Al) headlands, during eastern WAG migrations or during a double-gyre configuration.

- Around Cape Three Forks (3F): In this case, the current flows eastward with the coast to its right and generates strong anticyclonic vorticity ($\zeta < -f$).
- The same mechanism generates anticyclonic vorticity at the Oran headland along the path of the Algerian current.

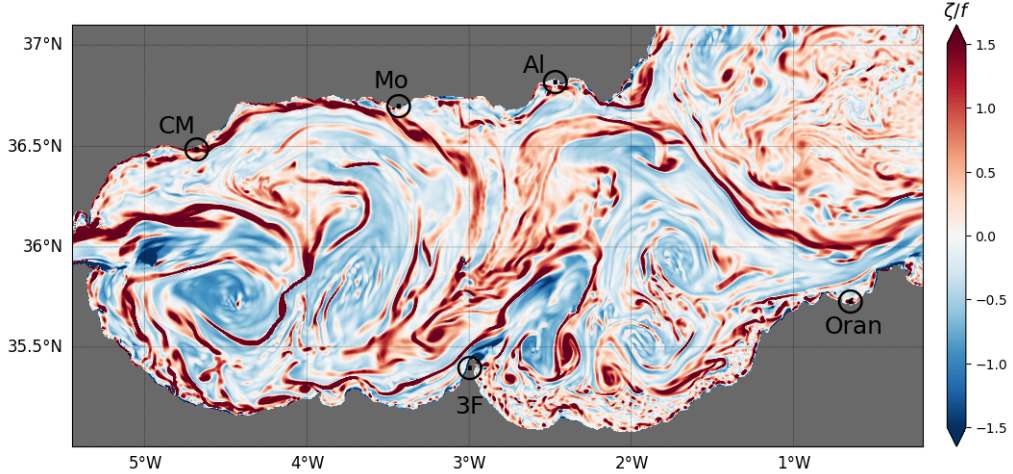


Figure 5.1: Surface relative vorticity snapshot from the Alb500 simulation on October 30, 2011 (during a double-gyre configuration) and locations of interest: Cala de Mijas (CM), Motril (Mo), Almeria (Al), Cape Three Forks (3F) and Oran.

We focus our analysis on the TVG along the Spanish coast between CM and Mo, due to the strong influence of this process in the shape and evolution of the WAG, and because these events are recurrent throughout the full simulation period and frequently linked with frontogenesis developed along the eastern edge of the gyre.

In summary, the TVG mechanism in this region (and, in general, in currents flowing with the coast to the left) follows this sequence:

- Positive relative vorticity increases to values $\zeta \gtrsim f$ as the current flows along the coast.
- Current separation occurs after impacting against a topographic obstacle and vorticity is advected offshore.

- On the downstream side, the flow is unstable and advected vorticity usually self-organizes into small coherent vortices.
- There is eddy to mean KE conversion on the upstream side of the topographic feature, where perturbation growth is restrained due to enhanced horizontal shear. Downstream, the destabilization of the current results in mean to eddy KE conversion (Energy conversion is analyzed in Section 3.2.4).

In the next sections we examine the evolution of the vorticity field during a TVG event and analyze the barotropic vorticity equation in order to show the role of topography in generation of cyclonic vorticity.

Evidence of TVG in the Alboran sea

The TVG process is analyzed using the Alb500 solution during a model period over which recurrent episodes of topographic cyclonic vorticity generation occur along the coast between CM and Mo (we refer to this episode as the WAG_2011 event). WAG_2011 occurred during February-March 2011 with a duration of about 45 days, and it is characterized by a single gyre configuration, with the WAG centered around 36°N - 3.8°W, but with recurrent migrations of its eastern edge toward Almeria headland.

Time averaged surface velocity during this event is shown in Figure 5.2. The northern edge of the gyre flows along the Spanish coast, between the CM and Mo headlands. Separation of the boundary current occurs near Mo, flowing southeastward and following a circular trajectory around the gyre.

The surface mean relative vorticity field for the WAG_2011 event shows that higher values ($\zeta/f \gtrsim 1$) occur in areas where the current interacts with topography (Figure 5.3). Strong cyclonic vorticity is generated in regions where the current flows with the coast to its left, while anticyclonic vorticity is enhanced around headlands with the coast to the right.

Although the mean position of the WAG is centered around 36°N, 3.8°W (Figure 5.2), the vorticity field reveals eastward migrations of the gyre west of the Almeria headland (around 2.8°W) as reflected in the succession of snapshots shown in Figure 5.4. The sequence starts on February 28, 2011, with the WAG displaced to the south (top left panel); on March 9, 2011 (top right panel) the WAG has moved northward

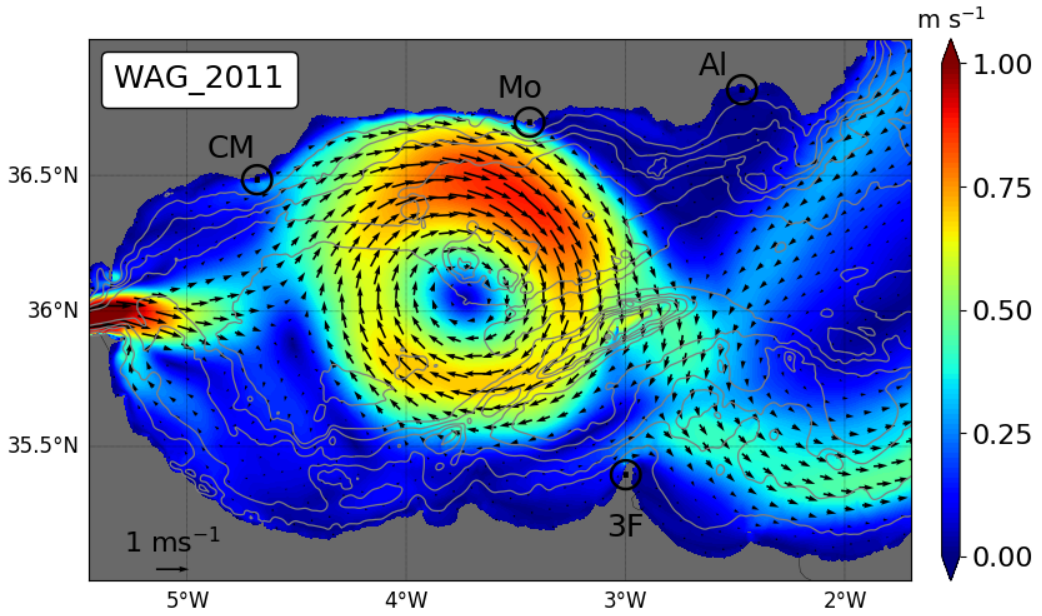


Figure 5.2: Surface velocity averaged over the period of the WAG_01/2011 event and locations of interest: Cala de Mijas (CM), Motril (Mo), Almeria (Al) and Cape Three Forks (3F). Bathymetry is plotted at 100, 300, 500, 750, 1000, 1500 and 2000 m.

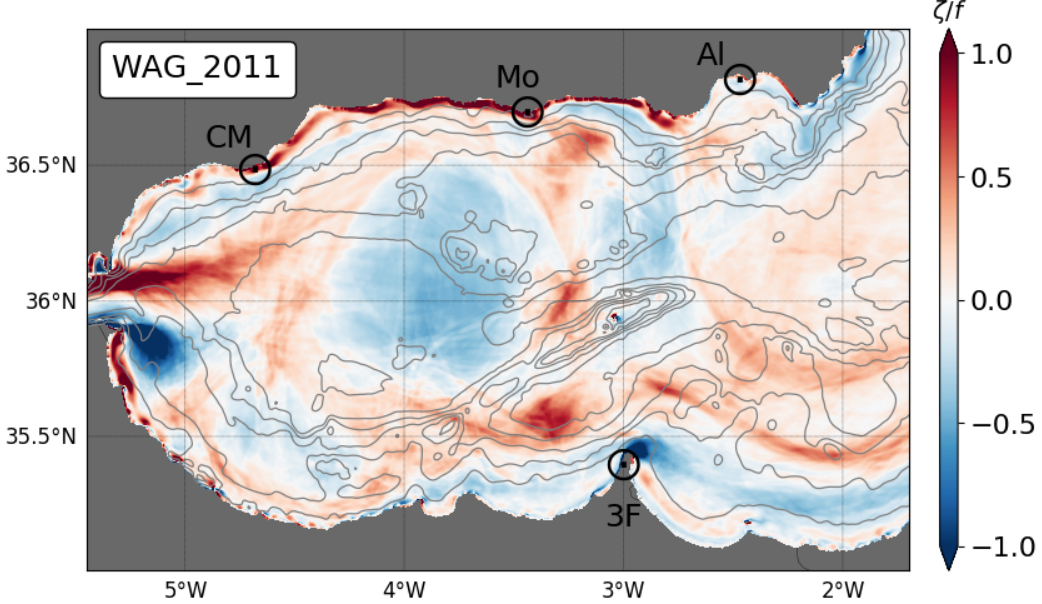


Figure 5.3: Surface relative vorticity normalized by the Coriolis parameter, ζ/f , averaged over the period of the WAG_2011 event. Bathymetry is plotted at 100, 300, 500, 750, 1000, 1500 and 2000 m.

and a secondary half-gyre emerges from the open eastern edge of the WAG, leading to

an incomplete double-gyre configuration several days later (bottom left panel; March 17, 2011) which is diluted at the end of the sequence (bottom right panel; March 23, 2011). Narrow strips of large cyclonic vorticity ($\zeta/f > 2.5$) emerge along the northern coast and the eastern edges of the gyres.

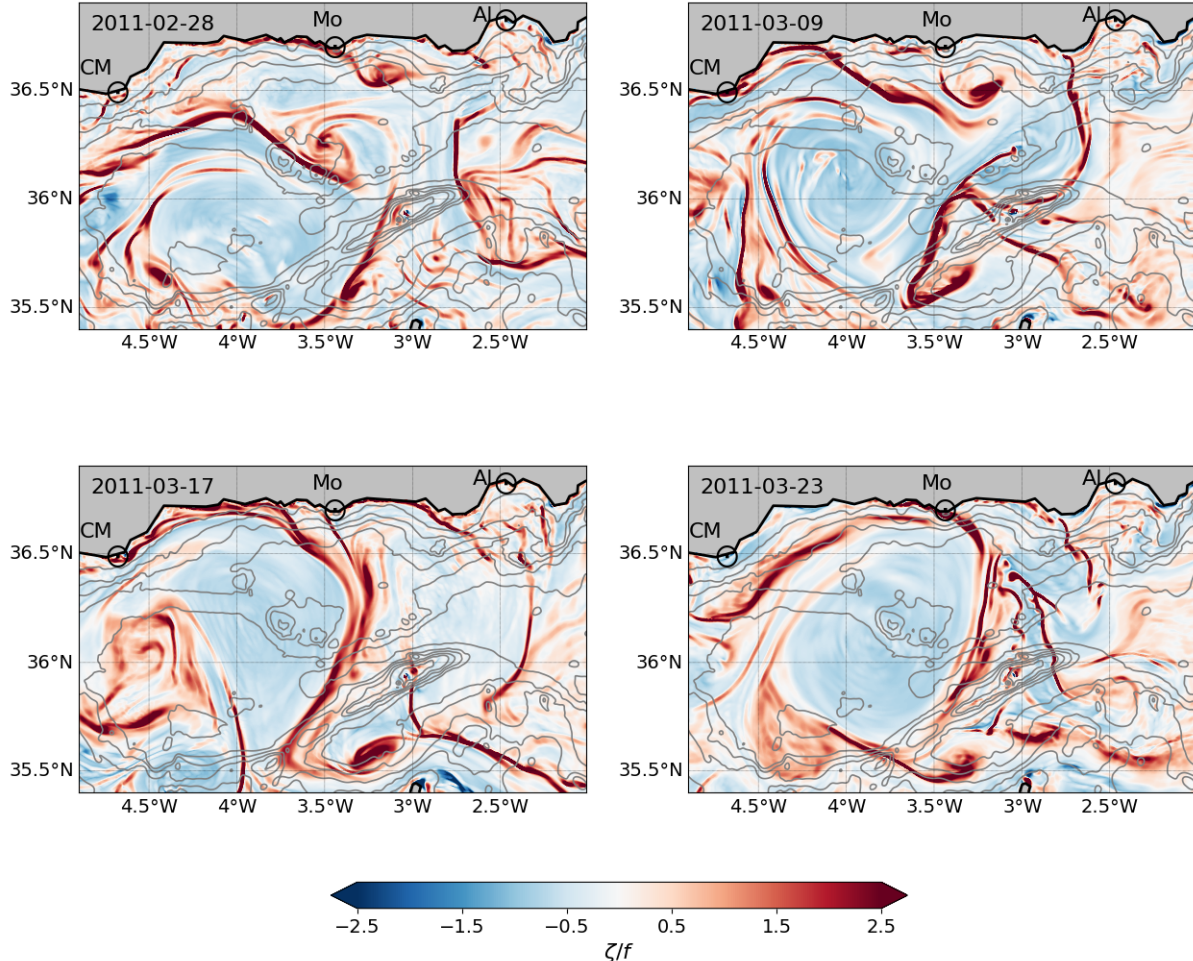


Figure 5.4: Snapshots (3-hourly averages) of surface relative vorticity, ζ/f , along the coast connecting the Cala de Mijas (CM), Motril (Mo) and Almeria (Al) headlands corresponding to different days during the WAG_2011 event. Bathymetry is plotted at 100, 300, 500, 750, 1000, 1500 and 2000 m.

More evidence of the presumed topographic origin of the positive vorticity input is shown in Figure 5.5. The left panel is a snapshot of the surface ζ/f field with several numbered vertical sections along the northern edge of the WAG. A strip of large cyclonic vorticity is generated along the coast between CM and Mo (right panels, vertical sections 2 and 3). Then, the current separates from the coast (section 4) and vorticity is advected offshore (section 5). Cyclonic vorticity is generated within the

Atlantic current that flows eastward along the coast (above isopycnal 28.2; see Section 4.2.2). Below this isopycnal surface, the Mediterranean counter-current flows westward toward the Strait with the coast to its right, thus generating negative vorticity along the slope (*e.g.*, vertical section 2). This two-layer configuration affects the barotropic vorticity budget and this must be carefully considered in the interpretation of the results in the next section.

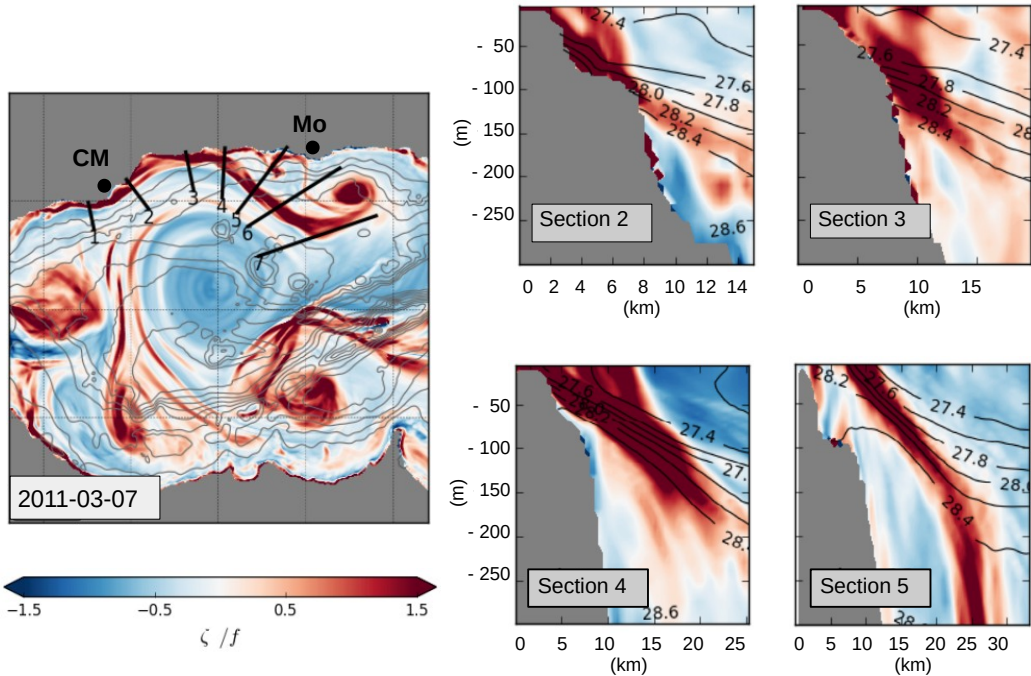


Figure 5.5: Left: snapshot (3-hourly average) of surface ζ/f along the coast between CM and Mo on March 7, 2011, with numbered vertical sections along the path of the Atlantic current (northern edge of the WAG). Bathymetry is plotted at 100, 300, 500, 750, 1000, 1500 and 2000 m. Right panels: evolution of the vertical field of ζ/f at the corresponding sections indicated on the surface map, with a 2-day interval between adjacent sections. Isopycnals are plotted at 0.2 kg m^{-3} intervals.

Quantification of TVG: the barotropic vorticity budget

The primary screening of the Alb500 surface vorticity fields shows that the WAG_2011 event is characterized by slight but rapid changes in the shape and position of the WAG, coupled with transient episodes of strong cyclonic vorticity generation along the

Spanish coast. This vorticity apparently stems from the interaction of the Atlantic current with the coast although, *a priori*, relative vorticity can result from a variety of sources: topographic interaction, wind and bottom stress, advection, etc. With the aim to demonstrate the principal role of topography in the generation of positive ζ , we analyze the terms in the barotropic vorticity equation in order to evaluate the contribution of each potential source.

Net vorticity in the ocean (see Appendix B) can be generated by one, or a combination of the following processes:

- Planetary vorticity advection: because f varies with latitude, planetary vorticity can vary during meridional displacements of the flow, while zonal migrations keep the f component invariant.
- Vortex stretching: stretching of the water column due to non-zero horizontal divergence implies a change in its relative vorticity by conservation of angular momentum. Because Ertel potential vorticity is conserved along the trajectory of the fluid, an increase (decrease) of the water column depth implies an increment (reduction) of the net vorticity.
- Relative vorticity production by frictional torques in the Ekman layers: frictional torques can be generated by wind or bottom stress (within the surface and bottom Ekman layers, respectively)
- Relative vorticity production by topographic steering of the flow: Interaction of the geostrophic flow against the topographic features generates large vertical vorticity within the sloped turbulent bottom boundary layer.
- Relative vorticity advection through fluid displacement.

The contribution of each potential vorticity source (or sink) can be quantified using the barotropic vorticity (BV) equation, which describes the rate of change of the barotropic vorticity of the flow. This equation can be written in a form which allows differentiation of the different sources of vorticity variability over the full water column.

Following the formulation from Gula et al. (2015a), we depart from the horizontal momentum equations in the Boussinesq approximation,

$$\frac{\partial u}{\partial t} + u \frac{\partial u}{\partial x} + v \frac{\partial u}{\partial y} + w \frac{\partial u}{\partial z} = -\frac{1}{\rho} \frac{\partial P}{\partial x} + fv + \mathcal{F}_x \quad (5.1)$$

$$\frac{\partial v}{\partial t} + u \frac{\partial v}{\partial x} + v \frac{\partial v}{\partial y} + w \frac{\partial v}{\partial z} = -\frac{1}{\rho} \frac{\partial P}{\partial y} - fu + \mathcal{F}_y \quad (5.2)$$

where \mathcal{F}_x and \mathcal{F}_y represent the horizontal components of the viscous stress and include horizontal diffusion and vertical mixing terms.

The barotropic velocity is the vertical integral of the horizontal velocity vector, \mathbf{u} , from the ocean floor ($z = -H$) to the free surface ($z = \eta$):

$$\mathbf{U} = (U, V) = \int_{-H}^{\eta} \mathbf{u} dz, \quad (5.3)$$

therefore BV is the curl of the vertically integrated velocity, that is, the curl of the transport:

$$\omega = \frac{\partial V}{\partial x} - \frac{\partial U}{\partial y}. \quad (5.4)$$

If we integrate Equations 5.1 and 5.2 in the vertical and cross-differentiate them, we obtain the rate of change of barotropic vorticity,

$$\frac{\partial \omega}{\partial t} = -\mathbf{U} \cdot \vec{\nabla} f - f \vec{\nabla} \cdot \mathbf{U} + \frac{J(P_b, H)}{\rho_0} + \vec{k} \cdot \vec{\nabla} \times \frac{\vec{\tau}_w}{\rho_0} - \vec{k} \cdot \vec{\nabla} \times \frac{\vec{\tau}_b}{\rho_0} - \mathcal{A} + \mathcal{D}, \quad (5.5)$$

where the rhs terms represent the contributions of:

- $-\mathbf{U} \cdot \vec{\nabla} f$: This is the βV term in the Sverdrup balance (Pedlosky, 2013) and accounts for the advection of planetary vorticity, f , through meridional water transport.
- $-f \vec{\nabla} \cdot \mathbf{U}$: Vorticity stretching caused by the divergence of the depth-integrated flow.
- $J(P_b, H)/\rho_0$: The bottom pressure torque, BPT, is the Jacobian of the bottom pressure, P_b , and the bottom depth, H . It represents the effect of interaction of the flow with topographic obstacles.
- $\vec{k} \cdot (\vec{\nabla} \times \vec{\tau}_w)/\rho_0$: The vertical component of the wind stress curl.
- $-\vec{k} \cdot (\vec{\nabla} \times \vec{\tau}_b)/\rho_0$: The vertical component of the bottom stress curl, BSC, quantifies the turbulent boundary layer processes at the bottom (bottom drag).
- $-\mathcal{A}$: Represents the nonlinear advective terms and is defined as:

$$\mathcal{A} = \frac{\partial^2 (VV - UU)}{\partial x \partial y} + \frac{\partial^2 UV}{\partial x^2} - \frac{\partial^2 UV}{\partial y^2}, \quad (5.6)$$

- \mathcal{D} : Contribution of horizontal diffusion.

Because we use an advective scheme with implicit diffusion (see Section 2.1), in practice, \mathcal{D} is included in the non-linear advective term, $-\mathcal{A}$.

Figure 5.6 shows the time-averaged barotropic vorticity, $\langle \omega \rangle$, for the WAG_2011 event after applying some smoothing using a Gaussian kernel of 4.0 km halfwidth. Figures 5.3 and 5.6 are significantly different in that the surface ζ is much more shoreline concentrated than the transport curl. These differences reflect that the Alboran Sea is a two layer system, with two water masses (AW in the surface layer and MW in the bottom layer) flowing in opposite directions. In the $\langle \omega \rangle$ map, the path of the deep Mediterranean flow is especially visible along the Spanish coast around the 400 m isobath, between CM and the SoG, and in the NE edge of the domain. These regions are preferred paths for this counter-current, as shown in Figure 4.11. Despite the presence of an opposing flow, there is positive net generation of BV in our region of interest, between CM and Mo.

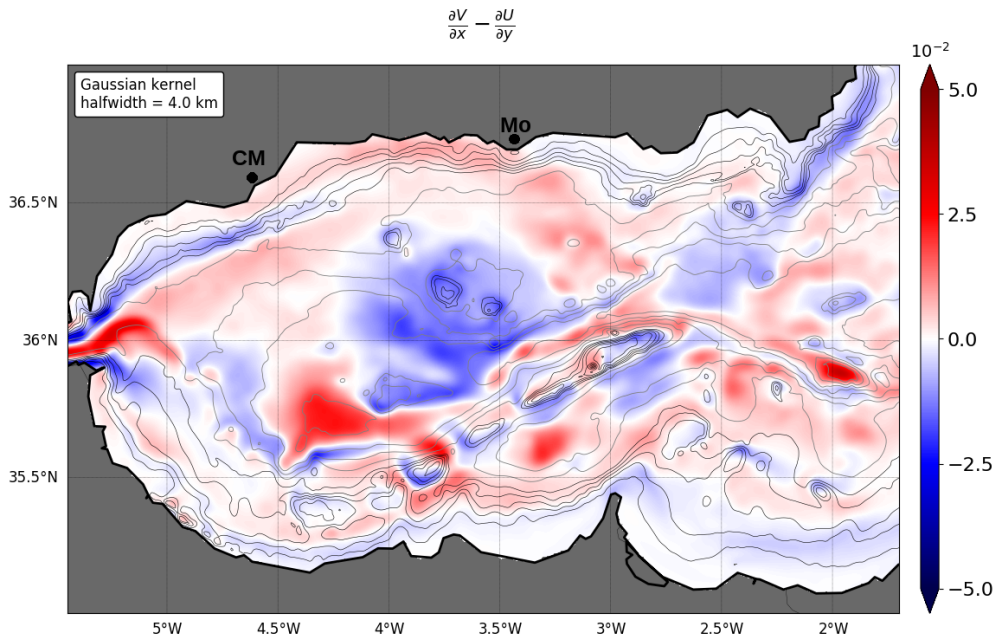


Figure 5.6: Top: Time-averaged barotropic vorticity, $\frac{\partial V}{\partial x} - \frac{\partial U}{\partial y}$, in m s^{-1} , smoothed using a Gaussian kernel of halfwidth 4 km. Bathymetry lines are contoured in black every 100 m down to 500 m depth, and in gray contours every 250 m down to 2500 m.

The effect of topography on vorticity generation relies in the BPT and BSC terms in Eq. 5.5. The average contributions of those terms over the WAG_2011 event shown in

Figure 5.7 reveal that the vorticity input due to bottom stress is one order of magnitude lower than the contribution of bottom pressure torques.

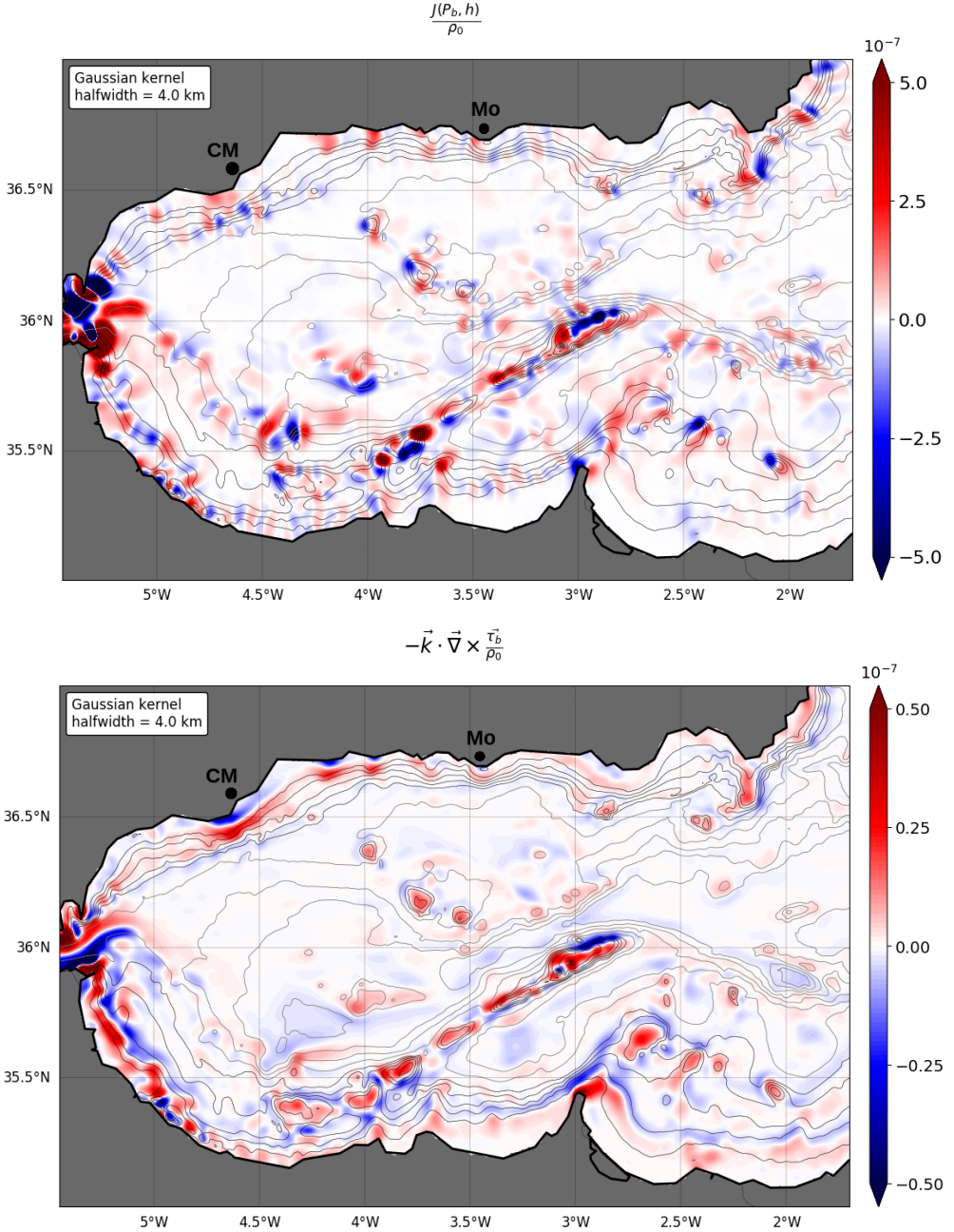


Figure 5.7: Contribution of BPT, $\frac{J(P_b, H)}{\rho_0}$ (top), and BSC, $-\vec{k} \cdot \vec{\nabla} \times \frac{\vec{\tau}_b}{\rho_0}$ (bottom), to the BV balance, in m s^{-2} . Both fields have been smoothed using a Gaussian kernel of halfwidth 4 km. Bathymetry lines are contoured in black every 100 m down to 500 m depth, and in gray contours every 250 m down to 2500 m.

BPT presents a very noisy dipole signal resulting from the complex topography, with alternating positive-negative spots around small scale features. This term quantifies the interaction of the flow with topographic features, as it is directly related to the net p_b around an obstacle through the relation

$$p_b = - \int \frac{J(P_b, H)}{\partial H / \partial n} ds , \quad (5.7)$$

where (n, s) are right-handed horizontal coordinates with s the distance along a fixed topographic contour and $\partial H / \partial n$ is the local slope (Molemaker et al., 2015).

On the other hand, as the flow attempts to follow the coast along constant bathymetry lines, the bottom pressure anomaly is balanced by the advection term in the momentum equations. It is therefore to be expected that there should be a local balance between the contributions of BPT and $-\mathcal{A}$ in the BV equation, as reflected in Figures 5.8 (showing the smoothed $-\mathcal{A}$ contribution) and 5.9 (showing the sum of the two terms).

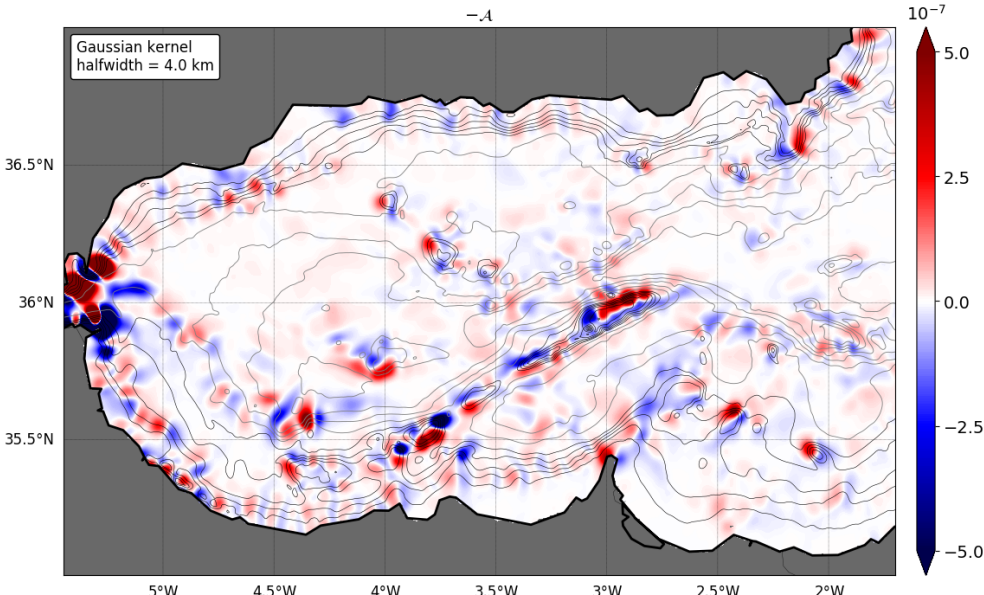


Figure 5.8: Contribution of non-linear advection term, $-\mathcal{A}$, in $m s^{-2}$, smoothed using a Gaussian kernel of halfwidth 4 km. Bathymetry lines are contoured at 100, 300, 500, 750, 1000, 1500, 2000 m.

As expected from the complex bathymetric configuration of the Alboran basin, planetary vorticity advection (Figure 5.10) largely contributes to the BV budget through the topographic vorticity stretching term, $-f \vec{\nabla} \cdot \mathbf{U}$, while the βV term (reflecting the

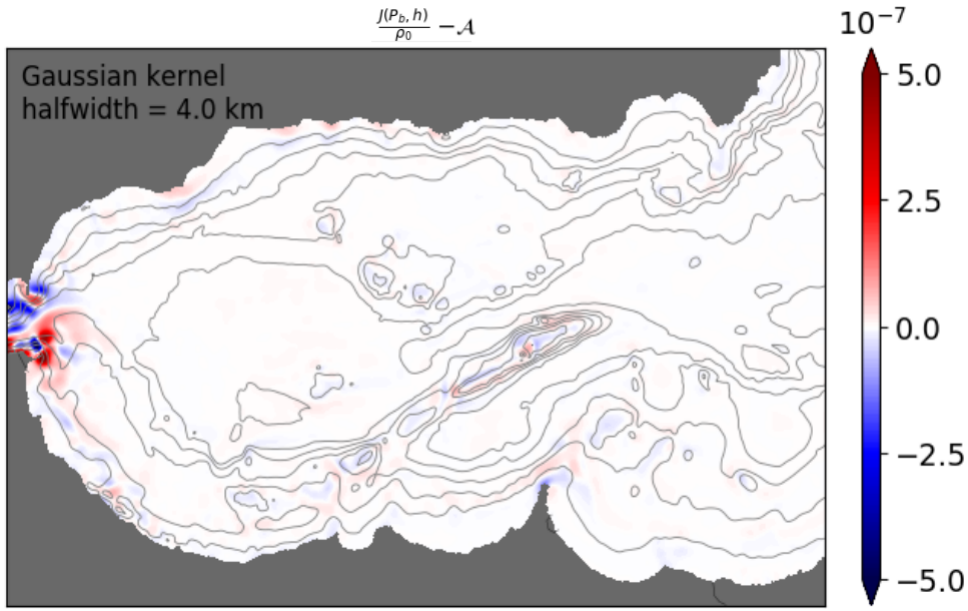


Figure 5.9: Addition of BPT and the non-linear advection term, $\frac{J(P_b, h)}{\rho_0} - A$, represented in Figures 5.7 (top) and 5.8, respectively. Bathymetry lines are contoured at 100, 300, 500, 750, 1000, 1500, 2000 m.

northward negative and southward positive advection of planetary vorticity) is negligible. Finally, the wind stress curl contribution is also negligible, being two or three orders of magnitude below the dominant components (Figure 5.11).

In order to show the rapid evolution of the TVG mechanism, the process of cyclonic relative vorticity generation, current separation and enhancement of barotropic vorticity through bottom pressure torques is further detailed through the sequence at daily intervals shown in Figures 5.12 to 5.14. Snapshots of surface ζ/f show an intensification of cyclonic vorticity along the coast as the northern edge of the WAG approaches the coast. After the current separates from the coast, vorticity is advected offshore and generates a cyclonic vortex, which is finally absorbed by the current flowing along the eastern edge of the gyre. The generation of cyclonic vorticity along the coast occurs within the Atlantic current (above the 28.2 isopycnal), as shown in the corresponding vertical sections. Below, from around 150 m depth, the Mediterranean current is a counter-current that flows towards the SoG. This is reflected in the BV maps, showing that positive BV generated along the coast is limited to the upper 100-150 m, exclusively occupied by the Atlantic eastward flow. The time evolution of this strip of BV coincides with the progressive enhancement of the BPT contribution, with peak values around days 8-9 in both cases. As in the current case, a large positive local BPT on

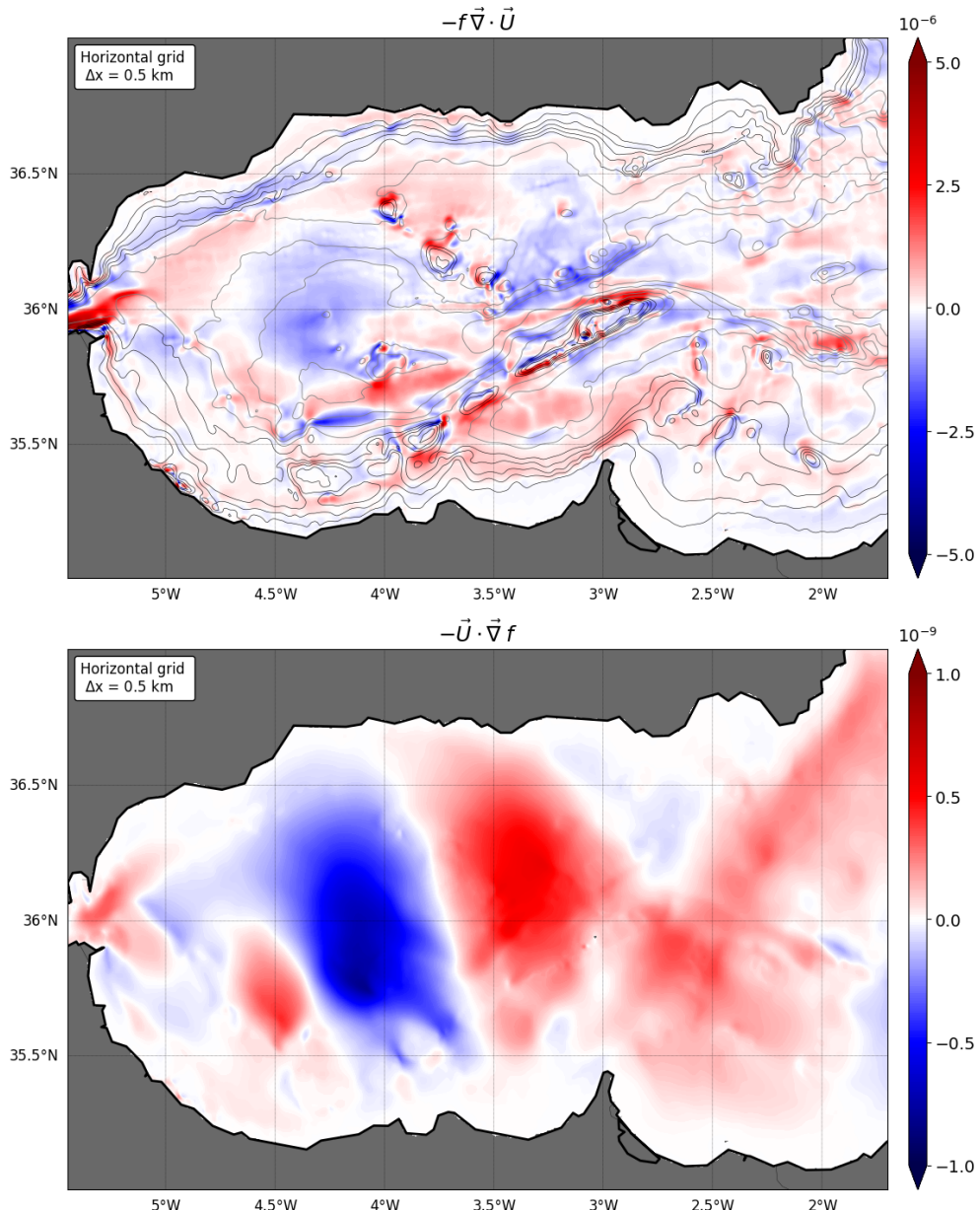


Figure 5.10: Contribution of planetary vorticity, $-\vec{\nabla} \cdot (f \vec{U})$, which is the sum of a topographic vorticity stretching term, $-f \vec{\nabla} \cdot \vec{U}$ (top), and the βV term, $-\vec{U} \cdot \vec{\nabla} f$ (bottom). All terms are in m s^{-2} . Bathymetry lines in the top panel are plotted in black every 100 m down to 500 m depth, and in gray contours every 250 m down to 2500 m.

the upstream side of a topographic feature does not necessarily imply current separation downstream; the region of negative BPT (broader, but less intense) downstream the obstacle, when integrated along fixed bathymetric contours, can provide enough

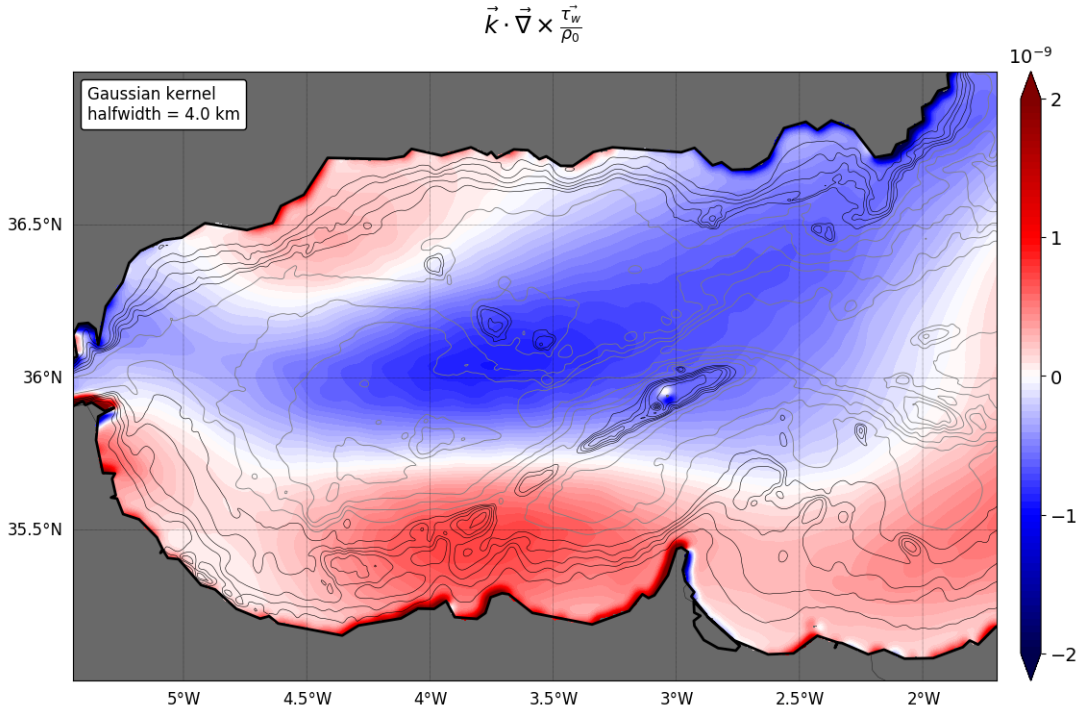


Figure 5.11: Contribution of wind stress curl, $\vec{k} \cdot \vec{\nabla} \times \frac{\vec{\tau}_w}{\rho_0}$, to the BV balance, in m s^{-2} , smoothed using a Gaussian kernel of halfwidth 4 km. Bathymetry lines are contoured in black every 100 m down to 500 m depth, and in gray contours every 250 m down to 2500 m.

negative p_b to overcome inertia and steer the flow attached to the coast.

Although here we have shown the TVG mechanism over one single event, we find the same sequence for similar events over the full Alb500 simulation. This TVG is a recurrent phenomenon along the Spanish coast and it is strongly linked to the presence of the WAG. Rapid changes in the shape, location and intensity of the gyre involve variations in the degree of vorticity generated along the slope and, furthermore, in the occurrence and location of current separation and offshore vorticity injection. With this example, we have shown that this solution provides enough spatial and temporal resolution to accurately reproduce the TVG mechanism in the Alboran Sea and to perform a comprehensive analysis of the process.

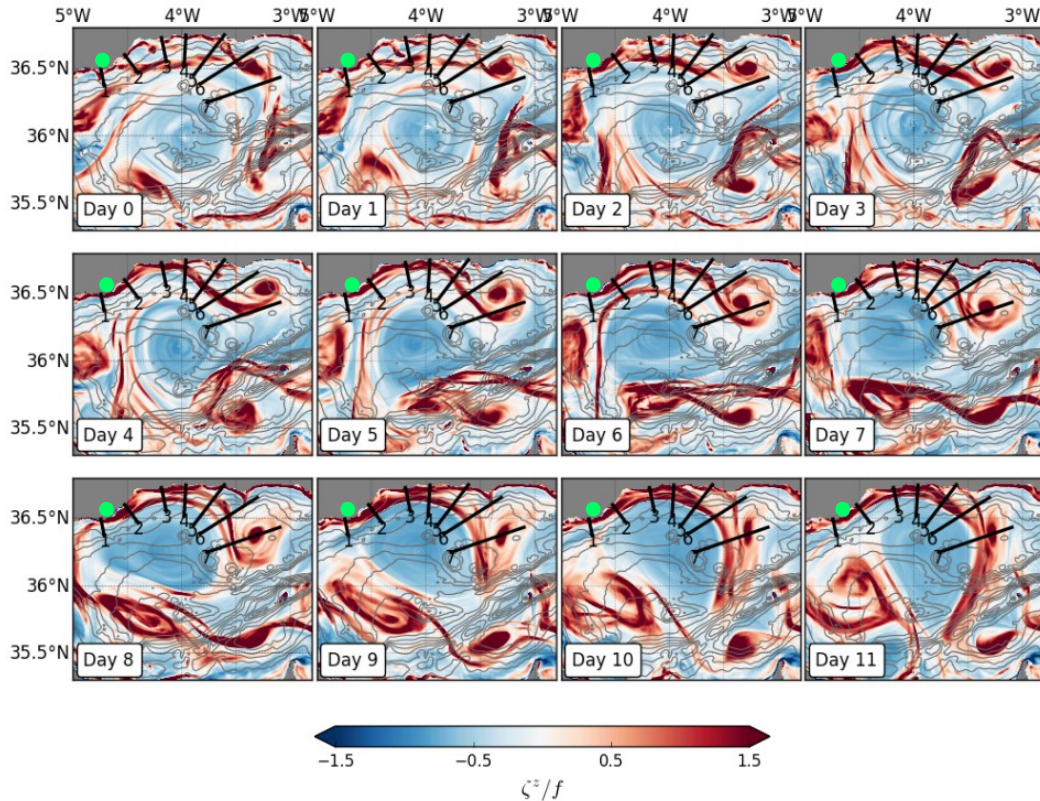


Figure 5.12: Snapshots of surface vorticity, ζ/f , over a sequence in which the Atlantic current interacts with topography along the Spanish coast in March 2011, during the *WAG_2011* event. The green spot on each panel indicates the location of the Cala de Mijas headland.

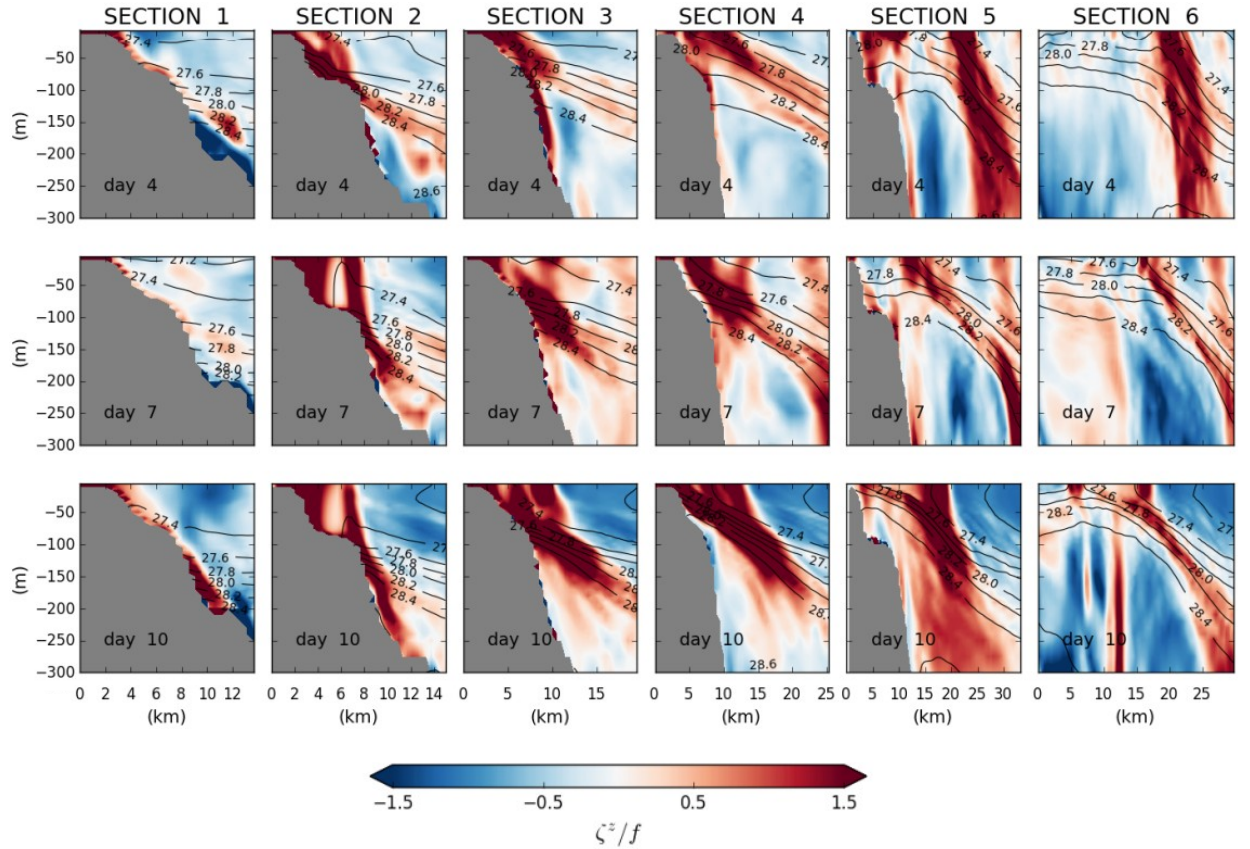


Figure 5.13: Vertical sections of surface vorticity, ζ/f , for the days and sections depicted in Figure 5.12. Isopycnals are plotted at 0.2 kg m^{-3} intervals, showing density anomalies relative to 1020 kg m^{-3} . The transition between the surface, fresh Atlantic water and the deep, dense Mediterranean flow occurs around isopycnal 28.2

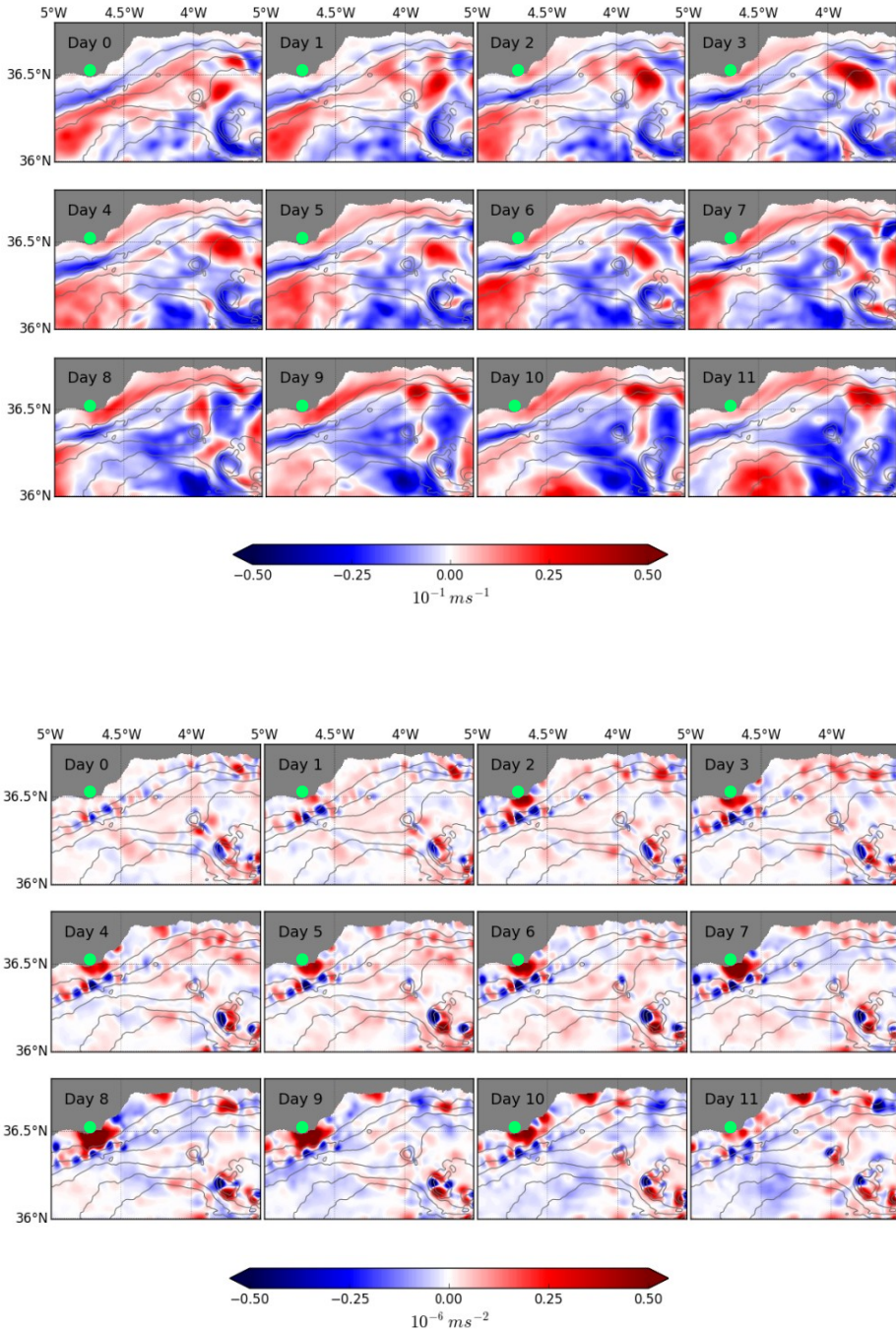


Figure 5.14: Top: Evolution of the barotropic vorticity, $\frac{\partial V}{\partial x} - \frac{\partial U}{\partial y}$, around the Cala de Mijas headland (green spot) over the sequence depicted in Figure 5.12. Bottom: evolution of the contribution of the BPT term, $\frac{J(P_b, h)}{\rho_0}$, to the BV budget. Bathymetry is plotted every 100 m in both panels.

5.2 Frontogenesis

A leading mechanism responsible for the emergence of submesoscale structures in the Alboran Sea is frontogenesis, a process promoted by the enhancement of the lateral buoyancy (mainly salinity) gradients, $\nabla_h b$, in the mixed layer (Hoskins and Bretherton, 1972; Capet et al., 2008). The sequence starts with the straining of the mesoscale velocity field, followed by disruption of the geostrophic balance for the alongfront flow and the development of an ageostrophic secondary circulation in the cross-frontal plane (Figure 5.15). The role of this secondary circulation is to restratify the mixed layer by

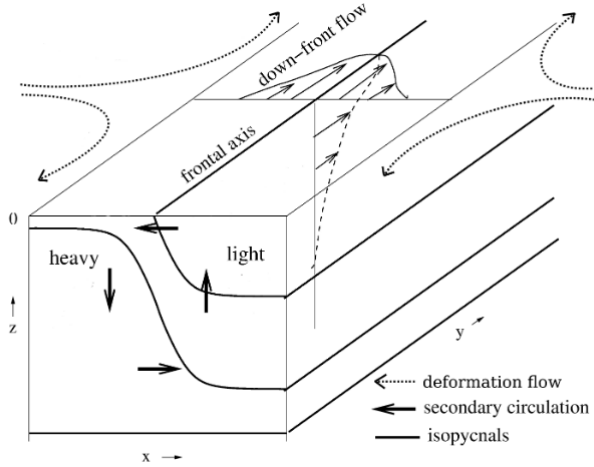


Figure 5.15: Schematic configuration of the secondary circulation developed in the cross-front plane of a strained induced surface front. Adapted from Capet et al. (2008).

tilting isopycnals toward the horizontal and thus restoring geostrophic balance. Vertical velocities are generated in the vicinity of the $\nabla_h b$ maximum, positive (upward) on the light side of the front and negative (downward) on the denser side. The large vertical velocity gradients ($\partial w / \partial z$) can lead to relative vorticity generation through the vertical vortex stretching term in the vorticity equation:

$$\frac{d\zeta}{dt} \approx (\zeta + f) \frac{\partial w}{\partial z}, \quad (5.8)$$

leading to enhanced cyclonic vorticity on the dense side of the front (with downward w).

Hoskins and Bretherton (1972) addressed the strain induced frontogenesis mechanism by analyzing the rate of increase of the horizontal buoyancy gradient induced by

the straining of the horizontal velocity field:

$$\frac{d|\nabla_h b|^2}{dt} = \mathcal{F}_h \quad (5.9)$$

where \mathcal{F}_h denotes the horizontal advective term of the *Lagrangian frontogenetic tendency*:

$$\mathcal{F}_h = - \left(\frac{\partial u}{\partial x} \frac{\partial b}{\partial x} + \frac{\partial v}{\partial x} \frac{\partial b}{\partial y}, \frac{\partial u}{\partial y} \frac{\partial b}{\partial x} + \frac{\partial v}{\partial y} \frac{\partial b}{\partial y} \right) \cdot \left(\frac{\partial b}{\partial x}, \frac{\partial b}{\partial y} \right) \quad (5.10)$$

where x and y represent the horizontal coordinates in the cross-front and along-front directions, respectively. Fronts are usually formed when $\mathcal{F}_h > 0$. Although this is the principal frontogenetic term in our case, the entire expression for the Lagrangian frontogenetic tendency, \mathcal{F} , includes other terms concerning vertical advection (associated with the restratification process), vertical mixing and horizontal diffusion, which might be of relative importance in other regions (Capet et al., 2008; Gula et al., 2014).

FG in the Alboran Sea

The particular strength of the Alboran Sea surface currents, together with the small size and complex shape of the basin, condition the permanent clash between Atlantic and Mediterranean waters in this region. Under this scenario, although recurrent surface fronts are to be expected, their occurrence, location, development and lifespans are highly variable. Their generation mechanisms and evolution are difficult to unravel, as they can easily interact with other submesoscale structures deriving from other typical dynamical processes with similar scales, such as internal waves, tides or the TVG mechanism described in the previous section.

The Almeria-Oran front represents the largest surface density (mostly salinity) jump in the Mediterranean Sea. The AO front has been extensively studied over recent decades, principally from a mesoscale perspective (see Section 1.5). However, understanding the generation mechanisms and the evolution of the frontal process (*e.g.*, the associated ageostrophic secondary circulation that provides coherent pathways between the surface water and depths below the pycnocline) remains a pending task as their developing scales demand large resolution in both time and space.

In our Alb500 simulation, the climatological AO front is only present in two episodes over the model period, in summer-autumn 2011 and in autumn 2013 (see Chapter 4). Faithful to the traditional description, the modeled AO front is linked to the presence of

the “two-gyre system” and coincides with the eastern flank of the EAG. Over the bulk of the 3-year model sequence, the dominant pattern is a single gyre (the WAG) that feeds an eastward current along the African coast. Under this regime, the principal salinity front is shifted to the west and coincides with the eastern edge of the WAG. The principal difference between both fronts lies in the shape and location of their respective associated gyres. In contrast, they have a similar structure, salinity gradients and isopycnal inclinations. Under these circumstances, and with regard to the study of the generation and evolution of the fronts, both configurations are analogous.

As in the case of the TVG events, the occurrence, location and duration of the frontal processes in our simulation display large variability, ruling out a general description from a statistical analysis of the full solution. Instead, we focus our analysis on a frontal event occurring during the *WAG_2011* sequence. The spatial structure is persistent over the full sequence with some modest lateral migrations of the front, associated with variations in the position of the eastern edge of the WAG. Recurrent frontogenesis during this event is revealed in the time averaged maps of $|\nabla b|$ and \mathcal{F}_h (Figure 5.16). The advective frontal tendency displays a positive (frontogenetic) background throughout the domain, with strong values at the principal frontal areas. Figures 5.17 and 5.18 show snapshots of the surface salinity and density gradient fields, respectively. The AO front is located between 3°W – 2.5°W and 36°N – 36.5°N . On the $|\nabla\rho|$ map in Figure 5.18 (top), areas with significant downwelling at 100 m depth ($w < -0.5 \text{ cm s}^{-1}$) are marked in orange. There is a narrow strip of downwelling along an adjacent line parallel to the front, on its heavy side, that confirms the development of a secondary circulation, as predicted in the schematic representation in Figure 5.15. The velocity vectors in the bottom panel in Figure 5.18 reveal some convergence at the surface around the strips of large $|\nabla\rho|$.

The cross-frontal secondary circulation is better characterized in the vertical sections shown in Figure 5.19. V_{\parallel} denotes a southward along-front flow, with the current located on the light side of the front (AW) and within the upper 20 m. V_{\perp} reveals a convergent cross-frontal flow down to about 100 m depth, associated with a narrow strip of very strong downwelling on the denser side that extends from the surface down to ~ 250 m depth, with a central velocity maximum of 2.35 cm s^{-1} ($\sim 2 \text{ km per day}$). Strong cyclonic vorticity is also present in the upper central front.

These episodes of frontogenesis, secondary circulation and vorticity generation do not necessarily persist over the lifespan of the surface front. They can lapse into

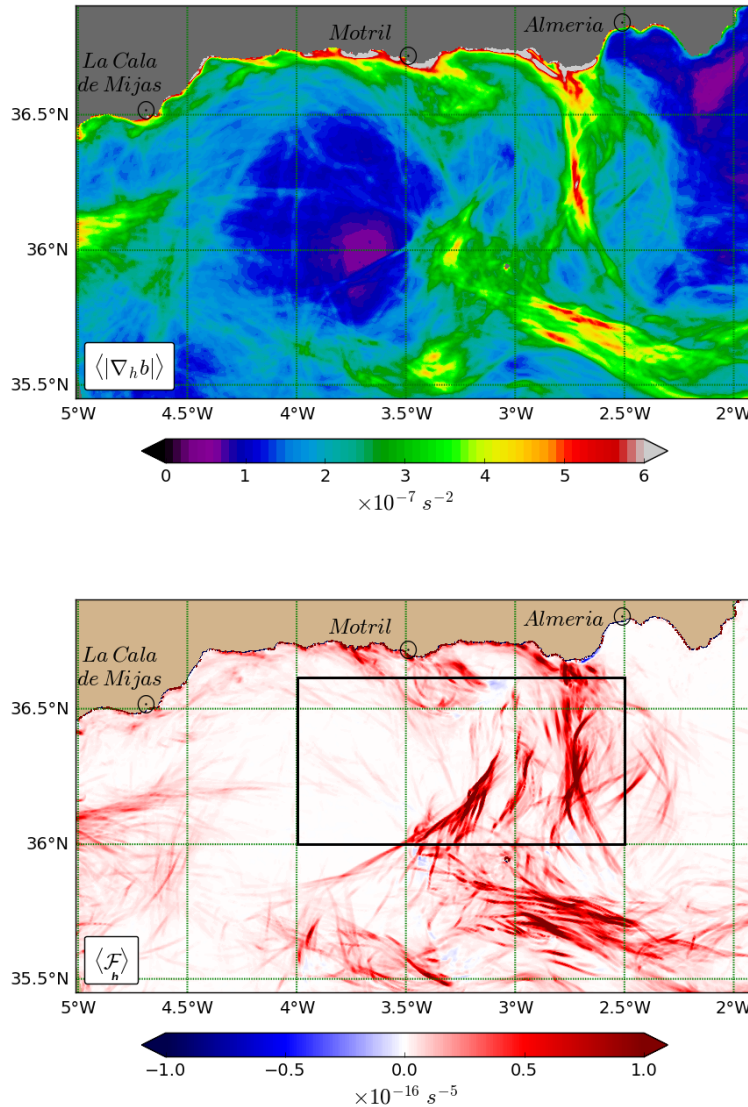


Figure 5.16: Top: Map of surface $|\nabla b|$ averaged over the *WAG_2011* event. Bottom: the corresponding time averaged advective frontogenetic tendency, \mathcal{F}_h , over this period. The black box in the bottom panel delimits the integration domain of the time series illustrated in Figure 5.21.

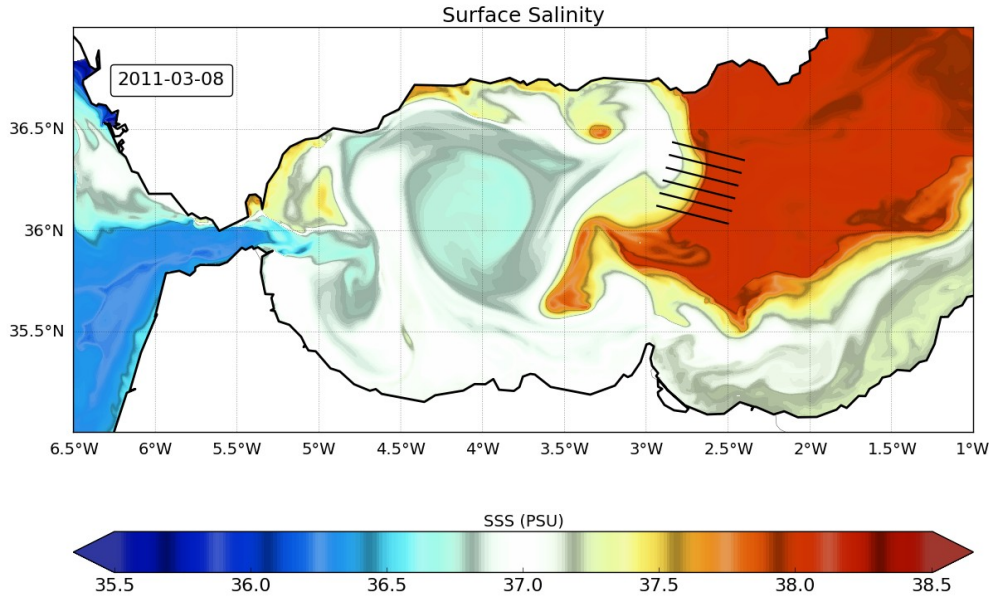


Figure 5.17: Surface salinity map on March 8, 2011, showing the front associated with the eastern edge of the WAG. The black lines along the front depict the vertical sections used to analyze the vertical structure of the front

a resting phase during which these processes are weak or suspended. This can be appreciated in the sequence shown in Figure 5.20, in which the downwelling phase is a transient process occurring within a persistent frontal event. The transience of the frontogenetic process is also revealed in Figure 5.21, showing the time evolution of the area integrated \mathcal{F}_h over the domain depicted in Figure 5.16 (bottom) during the *WAG_2011* event. Besides several relative maxima appearing during the sequence, a remarkable peak occurs around day 21, which corresponds to March 6, 2011, just a few hours prior to the strong downwelling event shown in Figures 5.19 and 5.20.

To conclude, we note that besides the front example presented here, there are many areas within the Alboran Sea with significant surface density frontal lines which do not necessarily have an associated downwelling. On the other hand, large deep w values might be associated with tidal effects and/or internal waves near topography (*e.g.*, at the Strait of Gibraltar or around the Alboran ridge).

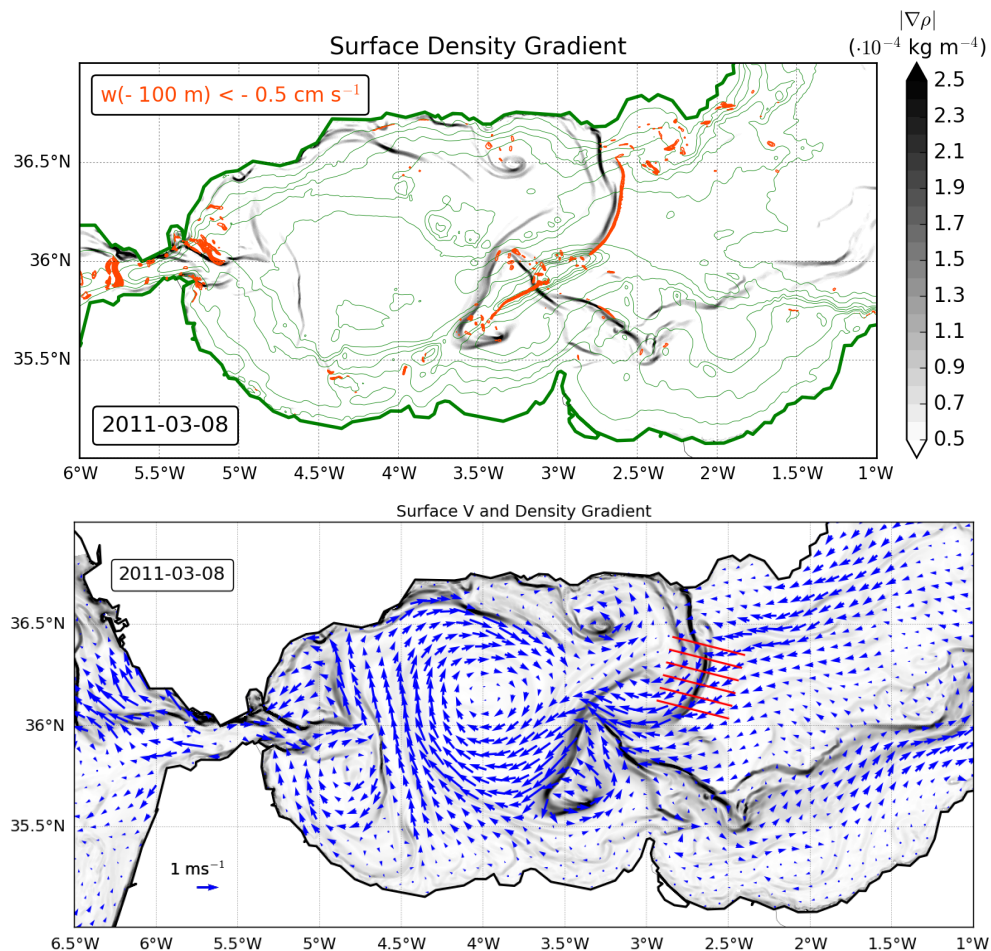


Figure 5.18: Top: Map of surface $|\nabla \rho|$ (gray) on March 8, 2011, and locations where downwelling at 100 m depth is significant, with $w < 0.5 \text{ cm s}^{-1}$ (orange). The green lines show topographic contours. Bottom: Surface velocity vectors superimposed on the density gradient field.

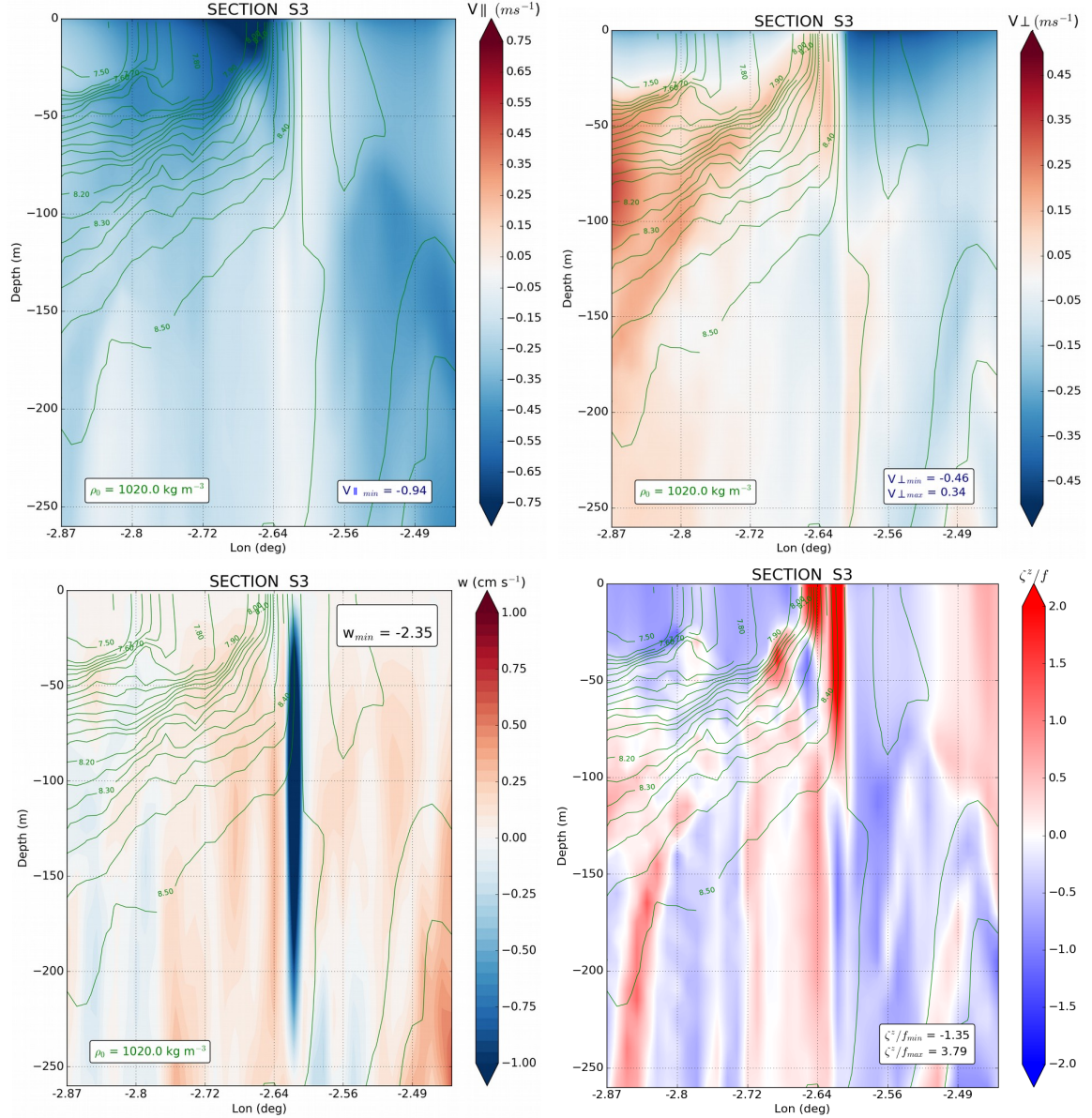


Figure 5.19: Plots of along-front V_{\parallel} (positive northward), cross-front V_{\perp} (positive eastward), vertical velocity, w , and vertical vorticity, ζ/f , on a middle cross-section for the selected front on March 8, 2011. The green lines are isopycnals for the density anomaly relative to 1020 kg/m^3 .

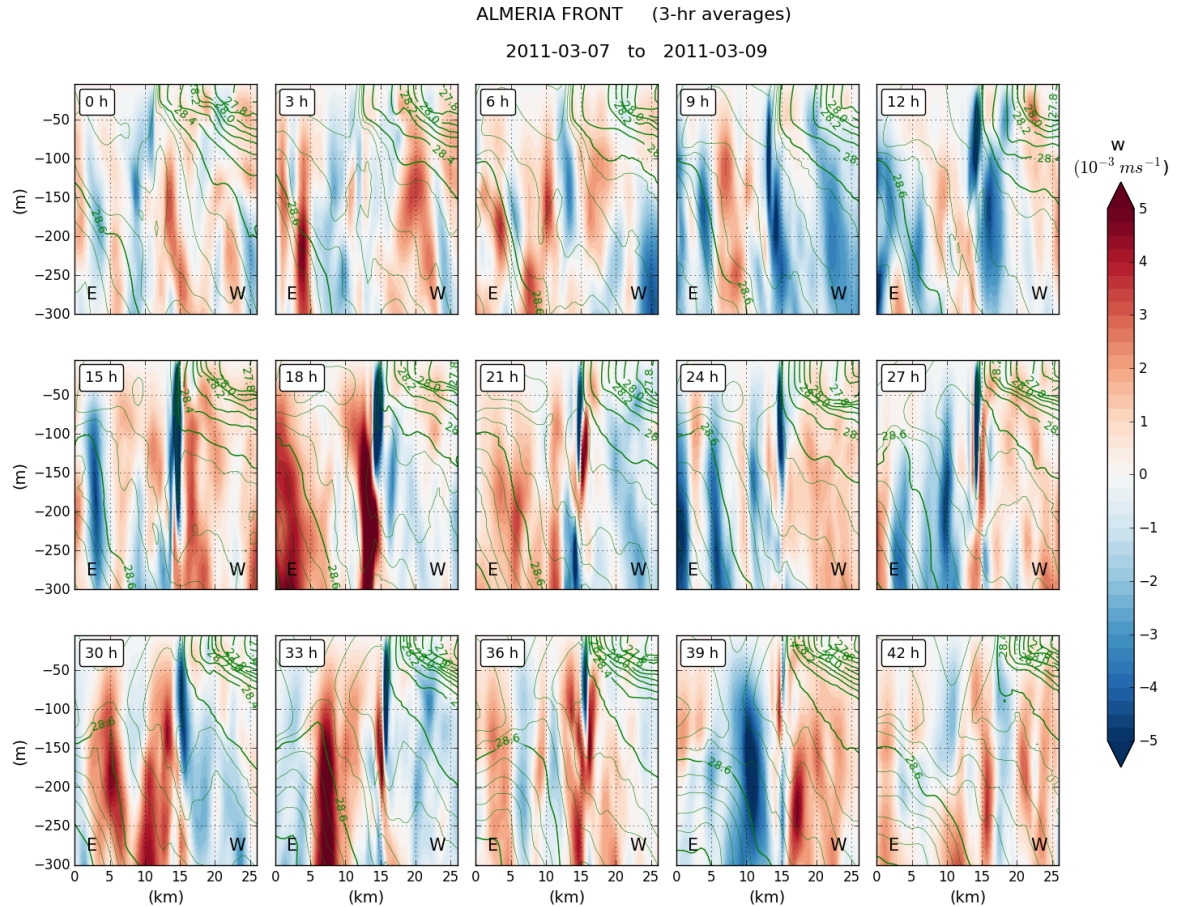


Figure 5.20: Evolution over 42 h of the vertical w field in the central section of the front shown in Figure 5.19 (note that here the sections are displayed from a downfront perspective, with the light side to the west). The narrow strip of downwelling associated with the secondary circulation persists almost over the full sequence. In contrast, the background field presents significant variability which could be related to other high frequency perturbations, such as internal waves of topographic or tidal origin. The green lines are isopycnals for the density anomaly.

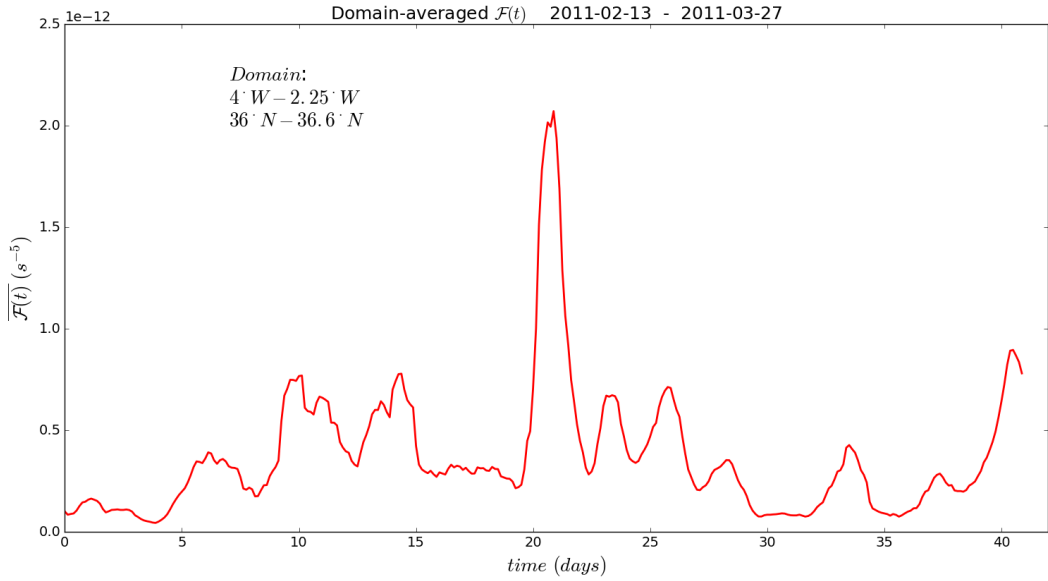


Figure 5.21: Time evolution of area averaged \mathcal{F}_h over the domain shown in Figure 5.16 (bottom) during the WAG_2011 event.

5.3 Discussion

From recent years, TVG has been proposed as a primary route to energy dissipation. Because this process occurs in the submesoscale range and involves the bottom layers, currently it has been only addressed from a model perspective, requiring large spatial and temporal resolutions. This mechanism has been investigated in the principal boundary currents, like the California Undercurrent and the Gulf Stream (Molemaker et al., 2015; Gula et al., 2015a) and also at a regional scale (D’Asaro, 1988; Hristova et al., 2014; Vic et al., 2015; Srinivasan et al., 2017; Morvan et al., 2019). To our knowledge, this is the first time that TVG is investigated in the Alboran Sea. The results obtained from the Alb500 simulation show that this mechanism plays a crucial role in driving ocean dynamics in this region, together with frontogenesis.

The frontal process described here has similar characteristics to the climatological AO front, which has been extensively documented over recent decades. For example, in the first *in situ* investigation of the front, Tintoré et al. (1988) detected a cross-front secondary circulation associated with surface convergence, characterized by an along-isopycnal sinking east of the front and an upwelling in the less dense waters west of the surface front.

Most of the early studies consist of mesoscale diagnostics of the frontal structure

based on altimetry observations and *in situ* measurements, from which vertical velocities are obtained using QG theory (*e.g.*, the mesoscale vertical motions of around 20–25 m day⁻¹ estimated by Allen et al. (2001)). However, the modeled vertical velocities in our case are much larger, with peak values up to around 2 km day⁻¹. Similar results have been recently obtained in other regions with similar frontal structures. During the Lagrangian Submesoscale Experiment (LASER) carried out during January–February 2016 in the Gulf of Mexico, D’Asaro et al. (2018) report the occurrence of submesoscale surface convergence around a strong density front, accompanied by cyclonic vorticity with local values larger than f and large density gradients. Observations show that the surface water converging at the front sinks with vertical velocities of 1–2 cm s⁻¹ (more than 1 km per day).

The evolution of research into frontal processes suggests that a detailed depiction of the mechanisms accompanying the development of a front require high spatial and temporal resolution in both observational and modeling approaches. With the example presented here, we show the capability of the Alb500 simulation to reproduce a front and its associated processes, mainly frontogenesis and the generation of ageostrophic secondary circulation. However, our results reveal that an accurate diagnostic of the vertical velocity field might require higher time resolution in order to determine the sources of the perturbations (frontogenesis, tides, MLIs, internal waves, etc.). This is expected to be achieved in further analyses using Lagrangian techniques.

Chapter 6

Summary and Conclusions

The transition from mesoscale to submesoscale dynamics is examined in the western Mediterranean Sea using a set of ROMS model simulations. The work is structured in a series of consecutive stages, starting from a large scale characterization of the regional WMed dynamics, and zooming in towards local submesoscale processes focusing on the Alboran Sea.

The ROMSWMED32 solution provides a suitable dataset for the mesoscale exploration. The analysis is assessed in terms of the Lorenz energy cycle, which affords a quantification of the kinetic-potential energy exchanges through eddy-mean flow interactions. The regional distribution of the principal energy conversion pathways reveals the nature of the submesoscale processes driving the conversion in the different areas of the basin.

Results from the LEC analysis lead us to focus our submesoscale research in the Alboran Sea. The transition is explored by means of two nested, realistic simulations covering this region with increasing horizontal resolutions ranging from 1.5 km (WMed1500) to 0.5 km (Alb500).

We hypothesize that two dominant submesoscale mechanisms set the energy routes toward dissipation: frontogenesis, a primary source of submesoscale currents in the upper mixed layer, and topographic vorticity generation at the bottom.

Conclusions

The analysis of the ROMSWMED32 solution provides a reliable characterization of the mesoscale currents and their seasonal variability in the western Mediterranean Sea. The twenty-year temporal extent of this dataset enables a statistically stationary state of the ocean, in which the energy balance is maintained through eddy-mean flow interactions.

At the basin scale, the Lorenz energy cycle reveals that the amount of KE stored in the large scale circulation (~ 0.6 PJ) is almost quadrupled by the reserves in the eddy flow (~ 2.2 PJ), a similar proportion to that obtained in other studies at a global scale.

The regional LEC formulation used in this study provides insight into the locality or non-locality of the mean-eddy flow interactions:

- In the Alboran Sea, barotropic and baroclinic instabilities contribute equally to EKE generation. While the former can be considered of local origin, nearly half of the EAPE converted into EKE via baroclinic instabilities is injected from the surroundings.
- In the Algerian Basin, the barotropic conversion route is highly nonlocal and half of the EKE generated through eddy momentum fluxes is injected from the outer regions. The largest contribution to the EKE in this subregion comes from EAPE transformations via baroclinic instabilities.
- APE transformations in the Northern Basin are significantly nonlocal, since a large amount of EAPE is supplied from outlying regions and converted into EKE. In this sector EKE production via barotropic instability (mostly local) results in less than 10% of the amount generated through baroclinic instability.

From the LEC analysis, the Alboran Sea – connecting the Mediterranean Sea to the Atlantic Ocean – is found to be the most energetic spot in the WMed. Its shape, location and complex bathymetry has significant implications for the dynamics in this area, characterized by a two-layer system with strong surface currents, gyres, fronts and topographic interaction, which necessarily induce the development of flow instabilities in the submesoscale range.

From this point, our nested WMed1500 and Alb500 simulations provide the spatial and temporal resolution required to address the transition towards submesoscale dynamics. SMCs arise in the finer solution, in which a strong positive skewness of the surface vorticity field reveals the dilution of the cyclonic-anticyclonic symmetry predicted by quasi-geostrophic theory. The regional characterization of the barotropic and baroclinic energy conversion terms suggest that SMCs emerge through shear instability generated by flow-topography interaction, or via eddy buoyancy fluxes generated in the boundary layer through winter mixing and frontogenesis.

The relatively short integration period of the Alb500 solution (3 years), together with the large spatial and temporal variability in the simulation, vetoes the possibility of a statistical approach to the submesoscale processes. Instead, our analysis is focused on particular events of topographic vorticity generation and frontogenesis which can be considered as representative of the Alboran Sea dynamics.

TVG is explored along the Spanish coast, in the area where the Atlantic current follows the path of the northern edge of the WAG. The analyzed event reproduces the sequence of typical TVG mechanisms: generation of strong positive vorticity ($\zeta/f > 1$) in the boundary current through enhanced horizontal shear; separation of the flow from the coast after impacting against a topographic obstacle; offshore advection of positive vorticity; and self-organization into small coherent vortices and/or absorption by the mean flow.

The potential sources of vorticity are analyzed and quantified in terms of the barotropic vorticity balance equation, in which the role of flow-topography interaction relies on two terms: the contribution of bottom pressure torque and the contribution of bottom stress, with the latter being one order of magnitude lower than the BPT term.

The analysis of TVG carried out in the Alboran Sea can be extrapolated to other regions in the WMed where this mechanism appears to be a source of SMCs: over the paths of the Algerian Current and the Northern Current, and around the Balearic Islands, etc. The characteristics of the WMed1500 solution allows local nested simulations focused on any region of interest, using a similar configuration as in the Alb500, which has proved to be highly effective in the Alboran basin.

Strain induced frontogenesis is a leading SMC generation mechanism in the Alboran Sea. The principal density fronts in our simulation appear along the eastern edge of

the WAG, in the vicinity of the climatological Almeria-Oran front, and have similar structures. In our analyzed event, FG is instigated by straining of the mesoscale velocity field, as revealed by the enhancement of the lateral buoyancy gradients within the mixed layer and from the evolution of the advective frontogenetic tendency over the sequence. An ageostrophic circulation develops in the cross-frontal plane, showing a narrow strip of strong downwelling which extends down to nearly 250 m depth and with vertical velocities of up to 2 km per day.

The background vertical velocity observed over this front and, in general, the 3D exploration of the Alb500 solution, suggest that the vertical motions might stem from additional sources of perturbations in the submesoscale range: MLIs, tidal effects, topographic internal waves, etc.

In future work, all these mechanisms and the possible interactions among them will be explored in further analysis of the Alb500 simulation and using Lagrangian techniques. The output dataset from this solution (including one restart file per day) provides the possibility to carry out new simulations of any event of interest with the large temporal resolution (up to several minutes) required for Lagrangian analysis.

Appendix A

The Rossby radius of deformation.

The horizontal scale of mesoscale eddies can be estimated from the Rossby radius of deformation, as it is the scale at which the effects of Earth rotation become as important as the gravitational forces. The *barotropic* or *external* Rossby radius, R_0 , is a function of depth and latitude and can be defined as “the distance over which deformations of the fluid surface by the Coriolis force are balanced by the gravitational tendency to flatten the free surface” (Pedlosky, 2013),

$$R_0 = \frac{\sqrt{gH}}{f}, \quad (\text{A.1})$$

where g is gravitational acceleration, H is the column depth and f the Coriolis parameter. However, in a stratified ocean, the horizontal scales also depend on the vertical stratification. Following Chelton et al. (1998), the baroclinic Rossby radii of deformation can be obtained by solving a Sturm–Liouville eigenvalue problem for the vertical structure of the vertical velocity, which can be written in the form:

$$\frac{d^2w}{dz^2} + \lambda^2 N^2 w = 0, \quad (\text{A.2})$$

where λ represents the eigenvalues, $w(z)$ the vertical velocity (and the eigenfunctions) and $N(z)$ is the Brunt–Väisälä frequency, defined as

$$N^2(z) = -\frac{g}{\rho_0} \frac{\partial \rho}{\partial z}, \quad (\text{A.3})$$

where ρ_0 is the reference density. Eq. A.2 permits an infinite number of eigenvalues, λ_m , and corresponding eigenfunctions, $w_m(z)$, where the subscript m refers to the baroclinic mode number. Applying the rigid–lid and flat–bottom boundary conditions

(*i.e.*, $w = 0$ at $z = 0$ and $z = -H$), Chelton et al. (1998) find an approximate solution for the first eigenvalue,

$$\lambda_1 \approx \frac{\pi}{\int_{-H}^0 N(z) dz}, \quad (\text{A.4})$$

from which we obtain the *first baroclinic* or *internal* Rossby radius,

$$R_1 = \frac{1}{\lambda_1 |f|} \approx \frac{\int_{-H}^0 N(z) dz}{\pi |f|}. \quad (\text{A.5})$$

The phase speed of long, first mode gravity waves in a non-rotating, continuously stratified fluid is given by $c_1 = \lambda_1^{-1}$, therefore the internal Rossby radius R_1 can be understood as the distance traveled by gravity waves at speed c_1 during a period f^{-1} .

An exhaustive derivation of the baroclinic Rossby radius estimate can be found in Chelton et al. (1998).

Appendix B

Vorticity

Vorticity represents the net spin of a fluid and is the contribution of two components: *planetary vorticity* due to Earth rotation ($= 2\vec{\Omega}$, where $\vec{\Omega}$ is the Earth's angular velocity) and *relative vorticity*, the curl of the fluid velocity ($\vec{\nabla} \times \mathbf{u}$, where \mathbf{u} is the flow velocity). In oceanic motions only the vertical component of the absolute vorticity is relevant. The vertical component of the planetary vorticity is the Coriolis parameter,

$$f = 2\Omega \sin \phi, \quad (\text{B.1})$$

where ϕ represents latitude. f defines the frequency of inertial oscillations, which is the angular velocity required for a fluid particle to describe a zonal displacement (along a constant latitude line). The inverse of the Coriolis frequency is called the *inertial period*, T_f . By definition, f is always positive in the Northern Hemisphere, with values ranging from $f = 0 \text{ s}^{-1}$ at the Equator (where $T_f = \infty$) to $f \approx 1.45 \cdot 10^{-4} \text{ s}^{-1}$ at the North Pole (where $T_f \approx 12 \text{ h}$). In typical Mediterranean latitudes (e.g., $\phi = 39^\circ\text{N}$) $f \approx 0.9 \cdot 10^{-4} \text{ s}^{-1}$, corresponding to an inertial period of $T_f \approx 19 \text{ hours}$. The vertical component of relative vorticity is, by definition:

$$\zeta = \partial v / \partial x - \partial u / \partial y, \quad (\text{B.2})$$

where u and v are the zonal and meridional components of the fluid velocity, respectively. Under such assumptions, we usually refer to absolute vorticity as

$$\text{Absolute vorticity} \approx f + \zeta \quad (\text{B.3})$$

In geostrophically balanced flows, mainly driven by Coriolis and pressure gradient forces, $|\zeta|$ is much smaller than f . In contrast, the submesoscale regime is characterized

by the enhancement of relative vorticity ($|\zeta| \sim \mathcal{O}(f)$) and the subsequent disruption of geostrophic balance. Under this scenario, a stability criterion can be derived in terms of Ertel potential vorticity, Π (Hoskins, 1974), a quantity related to the vorticity and stratification of the fluid:

$$\Pi = (\zeta + f) \cdot \nabla b , \quad (\text{B.4})$$

where b is buoyancy. In the absence of friction, heating and external forces, Ertel potential vorticity is conserved by fluid parcels. A sign reversal of Π is an indicator of ageostrophic centrifugal instability (Hoskins, 1974; Molemaker et al., 2015).

In relation to vorticity, we assume ocean motions in the Northern Hemisphere throughout the text.

Appendix C

ROMSWMED32 validation

C.1 Some validation aspects

The mean surface circulation of the western Mediterranean Sea is well reproduced in ROMSWMED32 as compared with the mean dynamic topography from Rio et al. (2014). The latter is performed by averaging the outputs from the Mediterranean Forecasting System ocean model as a first guess, updated with *in-situ* data from the available observations in the area. Escudier (2015) affirms that this dataset constitutes the best estimate of the mean surface circulation that is currently available for the WMed.

ROMSWMED32 eddy kinetic energy is compared with estimations derived from altimetry, drifter trajectories and the parent simulation NEMOMED12. Although the spatial distributions show similar patterns in the four data sets, the values are lower for altimetry and NEMOMED12. By contrast, energy values obtained from ROMSWMED32 are closer to those derived from drifters, as expected from the higher resolution capability of this model.

Validation of the thermohaline content is performed by comparing ROMSWMED32 with the NEMOMED12 model and with the gridded ENACT-ENSEMBLE version 4 (EN4) product from observational data. Time series of volume averaged temperature and salinity at different layers show that both models slightly overestimate the heat and salt contents, especially in the intermediate (150 – 600 m) and deep (600 – 3000 m) layers. ROMSWMED32 also displays a significant positive trend over time in both variables within the deep layer. This could be due to slight differences in the

transports through the boundaries, mainly the eastern one, computed from ROMS and NEMOMED12. Escudier (2015) states that the trend in the saline content could be partly responsible for the inability of this model to properly reproduce deep convection in the Gulf of Lions, while the parent NEMOMED12 simulation does. Exploring the sources of such deviations is not our goal, although we must take this constraint into consideration for the computation and interpretation of energy budgets in Chapter 3, with special care to potential energy.

A precise model description and validation can be consulted in Escudier (2015) and Escudier et al. (2016).

C.2 Assessment of statistical equilibrium and model spin-up

LEC analysis is based on the statistical stationarity of the amounts involved in the energy balance equations. In this regard, two issues should be addressed concerning the model outputs: it is necessary, first, to determine the spin-up time needed for the solution to reach stability and, secondly, to assess whether statistical equilibrium of the energy amounts is maintained over the analyzed period. To this end, the time evolution of volume integrated EKE and EAPE is computed in each region (Figure C.1). Although the annual cycle has been removed, many other sources of variability involving a wide spectrum of scales can affect the statistical equilibrium of the series: from the small scale fluctuations emerging from local dynamics, to the long-term tendencies stemming from the non-stationarity of atmospheric and boundary forcings. Despite this variability, these plots show that the stability of the model is virtually achieved in the three regions after three years. Beyond this spin-up, we can assume a form of statistical equilibrium of the series in the framework of the energy budget equations.

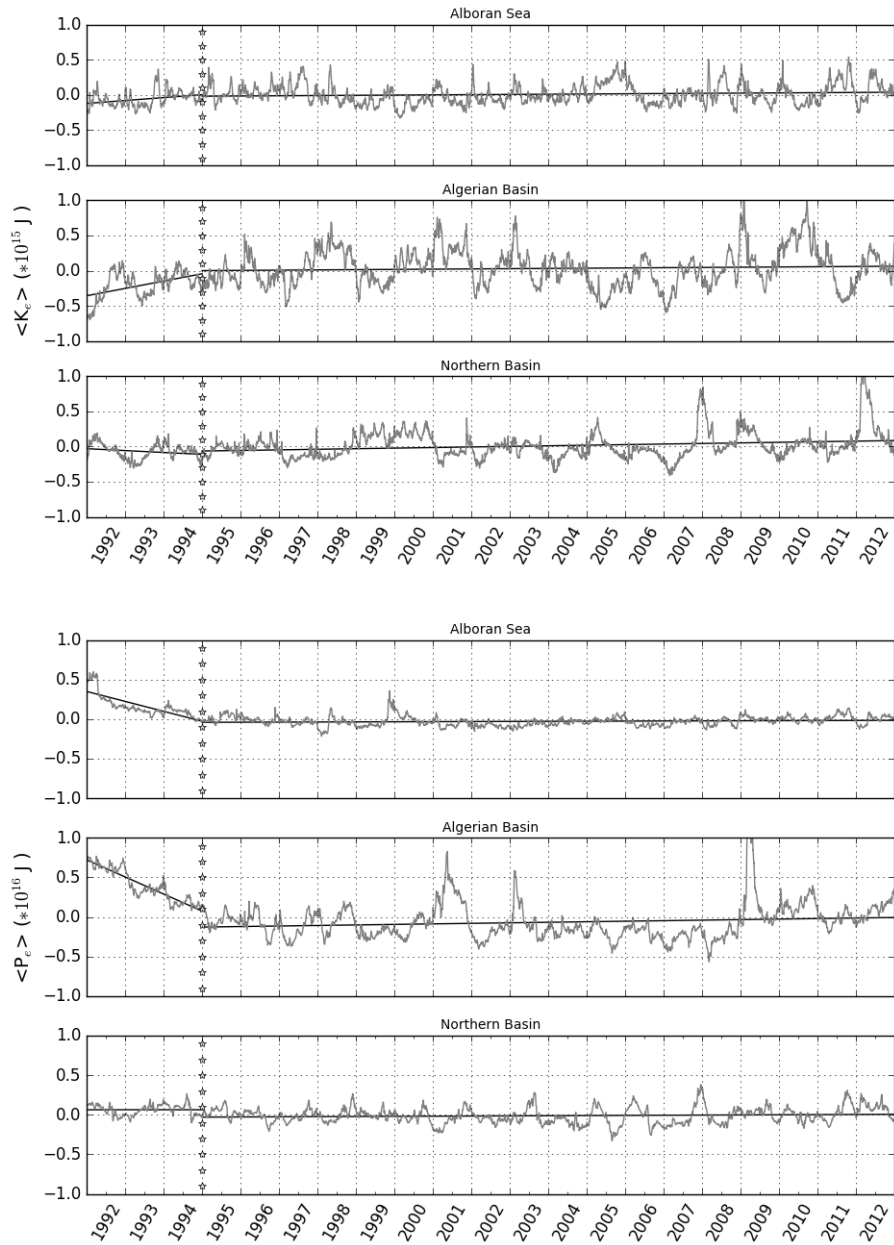


Figure C.1: Time series of the volume integrated EKE (top half) and EAPE (bottom half) for each region of the domain in ROMSWMED32. The annual cycle has been removed from the respective series. Linear adjustments (black lines) show the trends of the first three years of the series (1992 – 1994) in comparison with those of the 18 year remaining period (1995 – 2012).

Appendix D

The RANS equations

The mathematical concept of EKE strictly arises from the *Reynolds-averaged Navier-Stokes* (RANS) equations, whose development is based on the Reynolds decomposition of the flow properties (Equation (3.1)). The RANS momentum equations in the x, y and z directions are, respectively:

$$\frac{\partial \bar{u}}{\partial t} + \bar{u} \frac{\partial \bar{u}}{\partial x} + \bar{v} \frac{\partial \bar{u}}{\partial y} + \bar{w} \frac{\partial \bar{u}}{\partial z} = -\frac{1}{\rho} \frac{\partial \bar{p}}{\partial x} + \nu \left(\frac{\partial^2 \bar{u}}{\partial x^2} + \frac{\partial^2 \bar{u}}{\partial y^2} + \frac{\partial^2 \bar{u}}{\partial z^2} \right) - \left(\frac{\partial \bar{u}' u'}{\partial x} + \frac{\partial \bar{u}' v'}{\partial y} + \frac{\partial \bar{u}' w'}{\partial z} \right) \quad (\text{D.1})$$

$$\frac{\partial \bar{v}}{\partial t} + \bar{u} \frac{\partial \bar{v}}{\partial x} + \bar{v} \frac{\partial \bar{v}}{\partial y} + \bar{w} \frac{\partial \bar{v}}{\partial z} = -\frac{1}{\rho} \frac{\partial \bar{p}}{\partial y} + \nu \left(\frac{\partial^2 \bar{v}}{\partial x^2} + \frac{\partial^2 \bar{v}}{\partial y^2} + \frac{\partial^2 \bar{v}}{\partial z^2} \right) - \left(\frac{\partial \bar{v}' u'}{\partial x} + \frac{\partial \bar{v}' v'}{\partial y} + \frac{\partial \bar{v}' w'}{\partial z} \right) \quad (\text{D.2})$$

$$\frac{\partial \bar{w}}{\partial t} + \bar{u} \frac{\partial \bar{w}}{\partial x} + \bar{v} \frac{\partial \bar{w}}{\partial y} + \bar{w} \frac{\partial \bar{w}}{\partial z} = -\frac{1}{\rho} \frac{\partial \bar{p}}{\partial z} + \nu \left(\frac{\partial^2 \bar{w}}{\partial x^2} + \frac{\partial^2 \bar{w}}{\partial y^2} + \frac{\partial^2 \bar{w}}{\partial z^2} \right) - \left(\frac{\partial \bar{w}' u'}{\partial x} + \frac{\partial \bar{w}' v'}{\partial y} + \frac{\partial \bar{w}' w'}{\partial z} \right) \quad (\text{D.3})$$

As the averaged derivatives of the eddy components are zero, the averaged continuity equation is:

$$\frac{\partial \bar{u}}{\partial x} + \frac{\partial \bar{v}}{\partial y} + \frac{\partial \bar{w}}{\partial z} = 0 \quad (\text{D.4})$$

Equations (D.1) - (D.3) differ from the original Navier-Stokes in the last terms in parentheses on the rhs, which involve the velocity covariances and represent the *Reynolds stresses*. Its relevance lies in the fact that the mean turbulent (or eddy) kinetic energy

per unit mass, k_e , is defined to be half the trace of the Reynolds stress tensor:

$$\bar{k} = \frac{1}{2} \overline{(u'u' + v'v' + w'w')}, \quad (\text{D.5})$$

Appendix E

Notes about derivation of the KE balance equations

As stated in Storch et al. (2012, Appendix D), the balance equation of mean kinetic energy (Equation 3.7) is obtained by multiplying the zonal and meridional components of the momentum equations with \bar{u} and \bar{v} , summing up and averaging the results over time. To avoid any confusion arising from the time averaging of the tendency terms, here we show the derivation process for these terms.

First, we multiply the tendency terms in the zonal and meridional components of the Navier–Stokes momentum equations by \bar{u} and \bar{v} , respectively. Applying the Reynolds decomposition of the flow, we get

$$\bar{u} \frac{\partial (\bar{u} + u')}{\partial t} = \bar{u} \frac{\partial \bar{u}}{\partial t} + \bar{u} \frac{\partial u'}{\partial t}, \quad \text{and} \quad (\text{E.1})$$

$$\bar{v} \frac{\partial (\bar{v} + v')}{\partial t} = \bar{v} \frac{\partial \bar{v}}{\partial t} + \bar{v} \frac{\partial v'}{\partial t}. \quad (\text{E.2})$$

As \bar{u} and \bar{v} are the time averages of u and v , respectively, their partial derivatives (the first terms on the rhs of Equations E.1 and E.2) vanish. However, we retain those terms, since we want to achieve an expression that explicitly contains K_m . Thus, rewriting these terms and summing Equations E.1 and E.2 yields

$$\bar{u} \frac{\partial (\bar{u} + u')}{\partial t} + \bar{v} \frac{\partial (\bar{v} + v')}{\partial t} = \frac{\partial}{\partial t} \left(\frac{\bar{u}^2}{2} \right) + \frac{\partial}{\partial t} \left(\frac{\bar{v}^2}{2} \right) + \bar{u} \frac{\partial u'}{\partial t} + \bar{v} \frac{\partial v'}{\partial t}. \quad (\text{E.3})$$

The addition of the first two terms on the rhs gives $(1/\rho_0) \partial K_m / \partial t$. Then, time aver-

aging yields

$$\overline{u \frac{\partial (\bar{u} + u')}{\partial t} + \bar{v} \frac{\partial (\bar{v} + v')}{\partial t}} = \frac{1}{\rho_0} \frac{\partial K_m}{\partial t} + \overline{\bar{u} \frac{\partial u'}{\partial t}} + \overline{\bar{v} \frac{\partial v'}{\partial t}} = \frac{1}{\rho_0} \frac{\partial K_m}{\partial t}, \quad (\text{E.4})$$

as the averaged eddy components are, by definition, zero. Although $\partial K_m / \partial t$ is also zero, we retain this term in Equation 3.7 in order to maintain the symmetry of the four balance equations.

The same procedure, but multiplying the tendency terms in the zonal and meridional components of the Navier–Stokes momentum equations with u' and v' , respectively, yields the eddy kinetic energy balance (Equation 3.8).

Bibliography

- Allen, J. T., Smeed, D., Tintoré, J., and Ruiz, S. (2001). Mesoscale subduction at the Almeria–Oran front: Part 1: Ageostrophic flow. *Journal of Marine Systems*, 30(3-4):263–285.
- Baschek, B., Send, U., Lafuente, J. G., and Candela, J. (2001). Transport estimates in the Strait of Gibraltar with a tidal inverse model. *Journal of Geophysical Research: Oceans*, 106(C12):31033–31044.
- Becker, J., Sandwell, D., Smith, W., Braud, J., Binder, B., Depner, J., Fabre, D., Factor, J., Ingalls, S., Kim, S., et al. (2009). Global bathymetry and elevation data at 30 arc seconds resolution: SRTM30_PLUS. *Marine Geodesy*, 32(4):355–371.
- Beuvier, J., Béranger, K., Lebeaupin Brossier, C., Somot, S., Sevault, F., Drillet, Y., Bourdallé-Badie, R., Ferry, N., and Lyard, F. (2012). Spreading of the Western Mediterranean Deep Water after winter 2005: Time scales and deep cyclone transport. *Journal of Geophysical Research: Oceans*, 117(C7).
- Boccaletti, G., Ferrari, R., and Fox-Kemper, B. (2007). Mixed layer instabilities and restratification. *Journal of Physical Oceanography*, 37(9):2228–2250.
- Bosse, A., Testor, P., Houpert, L., Damien, P., Prieur, L., Hayes, D., Taillandier, V., de Madron, X. D., d'Ortenzio, F., Coppola, L., et al. (2016). Scales and dynamics of Submesoscale Coherent Vortices formed by deep convection in the northwestern Mediterranean Sea. *Journal of Geophysical Research: Oceans*, 121(10):7716–7742.
- Bosse, A., Testor, P., Mortier, L., Prieur, L., Taillandier, V., d'Ortenzio, F., and Coppola, L. (2015). Spreading of Levantine Intermediate Waters by submesoscale coherent vortices in the northwestern Mediterranean Sea as observed with gliders. *Journal of Geophysical Research: Oceans*, 120(3):1599–1622.

- Bracco, A., Liu, G., and Sun, D. (2019). Mesoscale-submesoscale interactions in the Gulf of Mexico: From oil dispersion to climate. *Chaos, Solitons & Fractals*, 119:63–72.
- Bryden, H. L. and Kinder, T. H. (1991). Steady two-layer exchange through the Strait of Gibraltar. *Deep Sea Research Part A. Oceanographic Research Papers*, 38:S445–S463.
- Cacho, I., Grimalt, J. O., Sierro, F. J., Shackleton, N., and Canals, M. (2000). Evidence for enhanced Mediterranean thermohaline circulation during rapid climatic coolings. *Earth and Planetary Science Letters*, 183(3-4):417–429.
- Candela, J. (2001). .7 Mediterranean water and global circulation. In *International Geophysics*, volume 77, pages 419–XLVIII. Elsevier.
- Capet, X., McWilliams, J. C., Molemaker, M. J., and Shchepetkin, A. (2008). Mesoscale to submesoscale transition in the California Current System. Part II: Frontal processes. *Journal of Physical Oceanography*, 38(1):44–64.
- Capó, E., Orfila, A., Mason, E., and Ruiz, S. (2019). Energy conversion routes in the western Mediterranean Sea estimated from eddy–mean flow interactions. *Journal of Physical Oceanography*, 49(1):247–267.
- Chelton, D. B., DeSzoeke, R. A., Schlax, M. G., El Naggar, K., and Siwertz, N. (1998). Geographical variability of the first baroclinic Rossby radius of deformation. *Journal of Physical Oceanography*, 28(3):433–460.
- Chen, R., Flierl, G. R., and Wunsch, C. (2014). A description of local and nonlocal eddy–mean flow interaction in a global eddy-permitting state estimate. *Journal of Physical Oceanography*, 44(9):2336–2352.
- D’Asaro, E. A. (1988). Generation of submesoscale vortices: A new mechanism. *Journal of Geophysical Research: Oceans*, 93(C6):6685–6693.
- D’Asaro, E. A., Shcherbina, A. Y., Klymak, J. M., Molemaker, J., Novelli, G., Guigand, C. M., Haza, A. C., Haus, B. K., Ryan, E. H., Jacobs, G. A., et al. (2018). Ocean convergence and the dispersion of flotsam. *Proceedings of the National Academy of Sciences*, 115(6):1162–1167.
- Debreu, L., Voulard, C., and Blayo, E. (2008). Agrif: Adaptive grid refinement in Fortran. *Computers & Geosciences*, 34(1):8–13.

- Escudier, R. (2015). *Mesoscale eddies in the western Mediterranean Sea: Characterization and understanding from satellite observations and model simulations*. PhD thesis, Universitat de les Illes Balears.
- Escudier, R., Renault, L., Pascual, A., Brasseur, P., Chelton, D., and Beuvier, J. (2016). Eddy properties in the Western Mediterranean Sea from satellite altimetry and a numerical simulation. *Journal of Geophysical Research: Oceans*, 121(6):3990–4006.
- Ferrari, R. and Wunsch, C. (2009). Ocean circulation kinetic energy: Reservoirs, sources, and sinks. *Annual Review of Fluid Mechanics*, 41:253–282.
- Fox-Kemper, B., Ferrari, R., and Hallberg, R. (2008). Parameterization of mixed layer eddies. Part I: Theory and diagnosis. *Journal of Physical Oceanography*, 38(6):1145–1165.
- García Lafuente, J., Delgado, J., Sánchez Román, A., Soto, J., Carracedo, L., and Díaz del Río, G. (2009). Interannual variability of the Mediterranean outflow observed in Espartel sill, western Strait of Gibraltar. *Journal of Geophysical Research: Oceans*, 114(C10).
- García Lafuente, J., Sánchez Román, A., Díaz del Río, G., Sannino, G., and Sánchez Garrido, J. (2007). Recent observations of seasonal variability of the Mediterranean outflow in the Strait of Gibraltar. *Journal of Geophysical Research: Oceans*, 112(C10).
- Garrett, C., Bormans, M., and Thompson, K. (1990). Is the exchange through the Strait of Gibraltar maximal or submaximal? In *The physical oceanography of sea straits*, pages 271–294. Springer.
- Garrett, C., Outerbridge, R., and Thompson, K. (1993). Interannual variability in Mediterranean heat and buoyancy fluxes. *Journal of Climate*, 6(5):900–910.
- Gula, J., Molemaker, M., and McWilliams, J. (2015a). Topographic vorticity generation, submesoscale instability and vortex street formation in the Gulf Stream. *Geophysical Research Letters*, 42(10):4054–4062.
- Gula, J., Molemaker, M. J., and McWilliams, J. C. (2014). Submesoscale cold filaments in the Gulf Stream. *Journal of Physical Oceanography*, 44(10):2617–2643.

- Gula, J., Molemaker, M. J., and McWilliams, J. C. (2015b). Gulf stream dynamics along the southeastern US seaboard. *Journal of Physical Oceanography*, 45(3):690–715.
- Gula, J., Molemaker, M. J., and McWilliams, J. C. (2016). Topographic generation of submesoscale centrifugal instability and energy dissipation. *Nature communications*, 7:12811.
- Harrison, D. and Robinson, A. (1978). Energy analysis of open regions of turbulent flows – Mean eddy energetics of a numerical ocean circulation experiment. *Dynamics of Atmospheres and Oceans*, 2(2):185–211.
- Heburn, G. W. and La Violette, P. E. (1990). Variations in the structure of the anti-cyclonic gyres found in the Alboran Sea. *Journal of Geophysical Research: Oceans*, 95(C2):1599–1613.
- Hernández-Carrasco, I. and Orfila, A. (2018). The Role of an Intense Front on the Connectivity of the Western Mediterranean Sea: The Cartagena-Tenes Front. *Journal of Geophysical Research: Oceans*, 123(6):4398–4422.
- Heslop, E. E., Ruiz, S., Allen, J., López-Jurado, J. L., Renault, L., and Tintoré, J. (2012). Autonomous underwater gliders monitoring variability at “choke points” in our ocean system: A case study in the Western Mediterranean Sea. *Geophysical Research Letters*, 39(20).
- Hoskins, B. (1974). The role of potential vorticity in symmetric stability and instability. *Quarterly Journal of the Royal Meteorological Society*, 100(425):480–482.
- Hoskins, B. J. and Bretherton, F. P. (1972). Atmospheric frontogenesis models: Mathematical formulation and solution. *Journal of the Atmospheric Sciences*, 29(1):11–37.
- Hristova, H. G., Kessler, W. S., McWilliams, J. C., and Molemaker, M. J. (2014). Mesoscale variability and its seasonality in the Solomon and Coral Seas. *Journal of Geophysical Research: Oceans*, 119(7):4669–4687.
- Huang, R. X. (2005). Available potential energy in the world’s oceans. *Journal of Marine Research*, 63(1):141–158.
- Lamb, K. G. (2014). Internal wave breaking and dissipation mechanisms on the continental slope/shelf. *Annual Review of Fluid Mechanics*, 46:231–254.

- Large, W. G., McWilliams, J. C., and Doney, S. C. (1994). Oceanic vertical mixing: A review and a model with a nonlocal boundary layer parameterization. *Reviews of Geophysics*, 32(4):363–403.
- Lellouche, J.-M., Greiner, E., Galloudec, O. L., Garric, G., Regnier, C., Drevillon, M., Benkiran, M., Testut, C.-E., Bourdalle-Badie, R., Gasparin, F., et al. (2018). Recent updates to the Copernicus Marine Service global ocean monitoring and forecasting real-time 1/12° high-resolution system. *Ocean Science*, 14(5):1093–1126.
- Lemarié, F., Debreu, L., Shchepetkin, A., and Mcwilliams, J. C. (2012a). On the stability and accuracy of the harmonic and biharmonic isoneutral mixing operators in ocean models. *Ocean Modelling*, 52:9–35.
- Lemarié, F., Kurian, J., Shchepetkin, A. F., Molemaker, M. J., Colas, F., and McWilliams, J. C. (2012b). Are there inescapable issues prohibiting the use of terrain-following coordinates in climate models? *Ocean Modelling*, 42:57–79.
- Lévy, M., Franks, P. J., and Smith, K. S. (2018). The role of submesoscale currents in structuring marine ecosystems. *Nature communications*, 9(1):4758.
- Li, L., Ingersoll, A. P., Jiang, X., Feldman, D., and Yung, Y. L. (2007). Lorenz energy cycle of the global atmosphere based on reanalysis datasets. *Geophysical Research Letters*, 34(16).
- Lorenz, E. N. (1955). Available potential energy and the maintenance of the general circulation. *Tellus*, 7(2):157–167.
- Macias, D., Garcia-Gorriz, E., and Stips, A. (2016). The seasonal cycle of the Atlantic Jet dynamics in the Alboran Sea: direct atmospheric forcing versus mediterranean thermohaline circulation. *Ocean Dynamics*, 66(2):137–151.
- Mahadevan, A. (2016). The impact of submesoscale physics on primary productivity of plankton. *Annual review of marine science*, 8:161–184.
- Malanotte-Rizzoli, P., Artale, V., Borzelli-Eusebi, G., Brenner, S., Crise, A., Gacic, M., Kress, N., Marullo, S., Ribera d’Alcalà, M., Sofianos, S., et al. (2014). Physical forcing and physical/biochemical variability of the Mediterranean Sea: a review of unresolved issues and directions for future research.

- Marchesiello, P., Debreu, L., and Couvelard, X. (2009). Spurious diapycnal mixing in terrain-following coordinate models: The problem and a solution. *Ocean Modelling*, 26(3-4):156–169.
- Marchesiello, P., McWilliams, J. C., and Shchepetkin, A. (2001). Open boundary conditions for long-term integration of regional oceanic models. *Ocean modelling*, 3(1-2):1–20.
- Marchesiello, P., McWilliams, J. C., and Shchepetkin, A. (2003). Equilibrium structure and dynamics of the California Current System. *Journal of physical Oceanography*, 33(4):753–783.
- Mason, E., Colas, F., Molemaker, J., Shchepetkin, A. F., Troupin, C., McWilliams, J. C., and Sangrà, P. (2011). Seasonal variability of the Canary Current: A numerical study. *Journal of Geophysical Research: Oceans*, 116(C6).
- Mason, E., Molemaker, J., Shchepetkin, A. F., Colas, F., McWilliams, J. C., and Sangrà, P. (2010). Procedures for offline grid nesting in regional ocean models. *Ocean modelling*, 35(1-2):1–15.
- Mason, E. and Pascual, A. (2013). Multiscale variability in the Balearic Sea: An altimetric perspective. *Journal of Geophysical Research: Oceans*, 118(6):3007–3025.
- Mason, E., Ruiz, S., Bourdalle-Badie, R., Reffray, G., García-Sotillo, M., and Pascual, A. (2019). New insight into 3-d mesoscale eddy properties from CMEMS operational models in the western Mediterranean. *Ocean Science*, 15(4):1111–1131.
- McWilliams, J. C. (2016). Submesoscale currents in the ocean. *Proceedings of the Royal Society A: Mathematical, Physical and Engineering Sciences*, 472(2189):20160117.
- Menemenlis, D., Fukumori, I., and Lee, T. (2007). Atlantic to Mediterranean sea level difference driven by winds near Gibraltar Strait. *Journal of physical oceanography*, 37(2):359–376.
- Millot, C. (1985). Some features of the Algerian Current. *Journal of Geophysical Research: Oceans*, 90(C4):7169–7176.
- Millot, C. (1999). Circulation in the western Mediterranean Sea. *Journal of Marine Systems*, 20(1-4):423–442.

- Molcard, A., Pinardi, N., Iskandarani, M., and Haidvogel, D. (2002). Wind driven general circulation of the Mediterranean Sea simulated with a spectral element ocean model. *Dynamics of Atmospheres and Oceans*, 35(2):97–130.
- Molemaker, M. J., McWilliams, J. C., and Dewar, W. K. (2015). Submesoscale instability and generation of mesoscale anticyclones near a separation of the California Undercurrent. *Journal of Physical Oceanography*, 45(3):613–629.
- Morvan, M., L'Hégaret, P., Xavier, C., Gula, J., Vic, C., Sokolovskiy, M., and Koshel, K. (2019). The life cycle of submesoscale eddies generated by topographic interactions. *Ocean Science*, pages 1–20.
- Naranjo, C., Garcia-Lafuente, J., Sannino, G., and Sanchez-Garrido, J. (2014). How much do tides affect the circulation of the Mediterranean Sea? from local processes in the Strait of Gibraltar to basin-scale effects. *Progress in oceanography*, 127:108–116.
- Nikurashin, M., Vallis, G. K., and Adcroft, A. (2013). Routes to energy dissipation for geostrophic flows in the Southern Ocean. *Nature Geoscience*, 6(1):48.
- Omand, M. M., D'Asaro, E. A., Lee, C. M., Perry, M. J., Briggs, N., Cetinić, I., and Mahadevan, A. (2015). Eddy-driven subduction exports particulate organic carbon from the spring bloom. *Science*, 348(6231):222–225.
- Oort, A. H., Anderson, L. A., and Peixoto, J. P. (1994). Estimates of the energy cycle of the oceans. *Journal of Geophysical Research: Oceans*, 99(C4):7665–7688.
- Orr, W. M. (1907). The stability or instability of the steady motions of a perfect liquid and of a viscous liquid. Part II: A viscous liquid. In *Proceedings of the Royal Irish Academy. Section A: Mathematical and Physical Sciences*, pages 69–138. JSTOR.
- Pascual, A., Ruiz, S., Olita, A., Troupin, C., Claret, M., Casas, B., Mourre, B., Poulain, P.-M., Tovar-Sanchez, A., Capet, A., et al. (2017). A multiplatform experiment to unravel meso-and submesoscale processes in an intense front (AlborEx). *Frontiers in Marine Science*, 4:39.
- Pedlosky, J. (2013). *Geophysical fluid dynamics*. Springer Science Business Media.
- Peliz, A., Boutov, D., Cardoso, R. M., Delgado, J., and Soares, P. M. (2013). The Gulf of Cadiz–Alboran Sea sub-basin: model setup, exchange and seasonal variability. *Ocean Modelling*, 61:49–67.

- Penven, P., Debreu, L., Marchesiello, P., and McWilliams, J. C. (2006). Evaluation and application of the ROMS 1-way embedding procedure to the central California upwelling system. *Ocean Modelling*, 12(1-2):157–187.
- Pinardi, N. and Masetti, E. (2000). Variability of the large scale general circulation of the Mediterranean Sea from observations and modelling: a review. *Palaeogeography, Palaeoclimatology, Palaeoecology*, 158(3-4):153–173.
- Pinot, J.-M., López-Jurado, J. L., and Riera, M. (2002). The CANALES experiment (1996–1998). interannual, seasonal, and mesoscale variability of the circulation in the Balearic Channels. *Progress in Oceanography*, 55(3-4):335–370.
- Pope, S. B. (2001). Turbulent flows.
- Poulain, P.-M., Bussani, A., Gerin, R., Jungwirth, R., Mauri, E., Menna, M., and Notarstefano, G. (2013). Mediterranean surface currents measured with drifters: From basin to subinertial scales. *Oceanography*, 26(1):38–47.
- Pujol, M.-I. and Larnicol, G. (2005). Mediterranean Sea eddy kinetic energy variability from 11 years of altimetric data. *Journal of Marine Systems*, 58(3-4):121–142.
- Reid, R., Elliott, B., and Olson, D. (1981). Available potential energy: A clarification. *Journal of Physical Oceanography*, 11(1):15–29.
- Renault, L., Molemaker, M. J., McWilliams, J. C., Shchepetkin, A. F., Lemarié, F., Chelton, D., Illig, S., and Hall, A. (2016). Modulation of wind work by oceanic current interaction with the atmosphere. *Journal of Physical Oceanography*, 46(6):1685–1704.
- Renault, L., Oguz, T., Pascual, A., Vizoso, G., and Tintoré, J. (2012). Surface circulation in the Alboran Sea (western Mediterranean) inferred from remotely sensed data. *Journal of Geophysical Research: Oceans*, 117(C8).
- Rio, M.-H., Pascual, A., Poulain, P.-M., Menna, M., Barceló, B., and Tintoré, J. (2014). Computation of a new mean dynamic topography for the Mediterranean Sea from model outputs, altimeter measurements and oceanographic in situ data. *Ocean Science*, 10(4):731–744.
- Robinson, A. R., Leslie, W. G., Theocaris, A., and Lascaratos, A. (2001). Mediterranean Sea circulation. *Ocean currents*, 1:19.

- Rudnick, D. L. (2001). On the skewness of vorticity in the upper ocean. *Geophysical Research Letters*, 28(10):2045–2048.
- Rudnick, D. L. and Davis, R. E. (1988). Frontogenesis in mixed layers. *Journal of physical oceanography*, 18(3):434–457.
- Ruiz, J., Echevarría, F., Font, J., Ruiz, S., García, E., Blanco, J., Jiménez-Gómez, F., Prieto, L., González-Alaminos, A., García, C., et al. (2001). Surface distribution of chlorophyll, particles and gelbstoff in the Atlantic jet of the Alborán Sea: from submesoscale to subinertial scales of variability. *Journal of Marine Systems*, 29(1-4):277–292.
- Ruiz, S., Pascual, A., Garau, B., Pujol, I., and Tintoré, J. (2009). Vertical motion in the upper ocean from glider and altimetry data. *Geophysical Research Letters*, 36(14).
- Sánchez Garrido, J. C., García Lafuente, J., Criado Aldeanueva, F., Baquerizo, A., and Sannino, G. (2008). Time-spatial variability observed in velocity of propagation of the internal bore in the Strait of Gibraltar. *Journal of Geophysical Research: Oceans*, 113(C7).
- Sánchez-Román, A., Jordà, G., Sannino, G., and Gomis, D. (2018). Modelling study of transformations of the exchange flows along the Strait of Gibraltar. *Ocean Science*, 14(6):1547–1566.
- Sánchez-Román, A., Sannino, G., García-Lafuente, J., Carillo, A., and Criado-Aldeanueva, F. (2009). Transport estimates at the western section of the Strait of Gibraltar: A combined experimental and numerical modeling study. *Journal of Geophysical Research: Oceans*, 114(C6).
- Sannino, G., Garrido, J. S., Liberti, L., and Pratt, L. (2014). Exchange flow through the Strait of Gibraltar as simulated by a σ -coordinate hydrostatic model and a z-coordinate non-hydrostatic model. *The Mediterranean Sea: Temporal Variability and Spatial Patterns*, pages 25–50.
- Sanz, J. L. (1991). *Prospección geofísica del Estrecho de Gibraltar: resultados del programa Hércules (1980–1983)*. Number 7. Ministerio de Agricultura, Pesca y Alimentación, Secretaría General Técnica.

- Sarhan, T., Lafuente, J. G., Vargas, M., Vargas, J. M., and Plaza, F. (2000). Upwelling mechanisms in the northwestern Alboran Sea. *Journal of Marine Systems*, 23(4):317–331.
- Shchepetkin, A. F. (2015). An adaptive, Courant-number-dependent implicit scheme for vertical advection in oceanic modeling. *Ocean Modelling*, 91:38–69.
- Shchepetkin, A. F. and McWilliams, J. C. (2003). A method for computing horizontal pressure-gradient force in an oceanic model with a nonaligned vertical coordinate. *Journal of Geophysical Research: Oceans*, 108(C3).
- Shchepetkin, A. F. and McWilliams, J. C. (2005). The regional oceanic modeling system (ROMS): a split-explicit, free-surface, topography-following-coordinate oceanic model. *Ocean modelling*, 9(4):347–404.
- Shchepetkin, A. F. and McWilliams, J. C. (2009a). Computational kernel algorithms for fine-scale, multiprocess, longtime oceanic simulations. In *Handbook of Numerical Analysis*, volume 14, pages 121–183. Elsevier.
- Shchepetkin, A. F. and McWilliams, J. C. (2009b). Correction and commentary for “Ocean forecasting in terrain-following coordinates: Formulation and skill assessment of the regional ocean modeling system” by Haidvogel et al., J. Comp. Phys. 227, pp. 3595–3624. *Journal of Computational Physics*, 228(24):8985–9000.
- Shcherbina, A. Y., D’Asaro, E. A., Lee, C. M., Klymak, J. M., Molemaker, M. J., and McWilliams, J. C. (2013). Statistics of vertical vorticity, divergence, and strain in a developed submesoscale turbulence field. *Geophysical Research Letters*, 40(17):4706–4711.
- Smith, W. H. and Sandwell, D. T. (1997). Global sea floor topography from satellite altimetry and ship depth soundings. *Science*, 277(5334):1956–1962.
- Sorgente, R., Olita, A., Oddo, P., Fazioli, L., and Ribotti, A. (2011). Numerical simulation and decomposition of kinetic energy in the central Mediterranean: insight on mesoscale circulation and energy conversion. *Ocean Science (OS)*.
- Soto-Navarro, J., Criado-Aldeanueva, F., García-Lafuente, J., and Sánchez-Román, A. (2010). Estimation of the Atlantic inflow through the Strait of Gibraltar from climatological and in situ data. *Journal of Geophysical Research: Oceans*, 115(C10).

- Spall, M. A. (1995). Frontogenesis, subduction, and cross-front exchange at upper ocean fronts. *Journal of Geophysical Research: Oceans*, 100(C2):2543–2557.
- Srinivasan, K., McWilliams, J. C., Renault, L., Hristova, H. G., Molemaker, J., and Kessler, W. S. (2017). Topographic and mixed layer submesoscale currents in the near-surface southwestern tropical Pacific. *Journal of Physical Oceanography*, 47(6):1221–1242.
- Storch, J.-S. v., Eden, C., Fast, I., Haak, H., Hernández-Deckers, D., Maier-Reimer, E., Marotzke, J., and Stammer, D. (2012). An estimate of the Lorenz energy cycle for the world ocean based on the STORM/NCEP simulation. *Journal of Physical Oceanography*, 42(12):2185–2205.
- Su, Z., Wang, J., Klein, P., Thompson, A. F., and Menemenlis, D. (2018). Ocean submesoscales as a key component of the global heat budget. *Nature communications*, 9(1):775.
- Thomas, L. N., Tandon, A., and Mahadevan, A. (2008). Submesoscale processes and dynamics. *Ocean modeling in an Eddying Regime*, 177:17–38.
- Thomas, L. N., Taylor, J. R., Ferrari, R., and Joyce, T. M. (2013). Symmetric instability in the Gulf Stream. *Deep Sea Research Part II: Topical Studies in Oceanography*, 91:96–110.
- Tintoré, J., La Violette, P., Blade, I., and Cruzado, A. (1988). A study of an intense density front in the eastern Alboran Sea: the Almeria–Oran front. *Journal of Physical Oceanography*, 18(10):1384–1397.
- Troupin, C., Pascual, A., Ruiz, S., Olita, A., Casas, B., Margirier, F., Poulain, P.-M., Notarstefano, G., Torner, M., Fernández, J. G., et al. (2019). The AlborEX dataset: sampling of sub-mesoscale features in the Alboran Sea. *Earth System Science Data*, 11(1):129–145.
- Vargas-Yáñez, M., Plaza, F., García-Lafuente, J., Sarhan, T., Vargas, J., and Vélez-Belchí, P. (2002). About the seasonal variability of the Alboran Sea circulation. *Journal of Marine Systems*, 35(3-4):229–248.
- Vic, C., Roullet, G., Capet, X., Carton, X., Molemaker, M. J., and Gula, J. (2015). Eddy-topography interactions and the fate of the Persian Gulf outflow. *Journal of Geophysical Research: Oceans*, 120(10):6700–6717.

- Viúdez, Á., Haney, R. L., and Vázquez-Cuervo, J. (1998). The deflection and division of an oceanic baroclinic jet by a coastal boundary: a case study in the Alboran Sea. *Journal of physical oceanography*, 28(2):289–308.
- Viúdez, Á., Tintoré, J., and Haney, R. L. (1996). Circulation in the Alboran Sea as determined by quasi-synoptic hydrographic observations. Part I: Three-dimensional structure of the two anticyclonic gyres. *Journal of Physical Oceanography*, 26(5):684–705.
- Vlasenko, V., Sanchez Garrido, J. C., Stashchuk, N., Garcia Lafuente, J., and Losada, M. (2009). Three-dimensional evolution of large-amplitude internal waves in the Strait of Gibraltar. *Journal of Physical Oceanography*, 39(9):2230–2246.
- Wu, Y., Wang, Z., and Liu, C. (2017). On the response of the Lorenz energy cycle for the Southern Ocean to intensified westerlies. *Journal of Geophysical Research: Oceans*, 122(3):2465–2493.
- Zaron, E. D. and Rocha, C. B. (2018). Internal gravity waves and meso/submesoscale currents in the ocean: Anticipating high-resolution observations from the SWOT Swath Altimeter Mission. *Bulletin of the American Meteorological Society*, 99(9):ES155–ES157.
- Ziegenbein, J. (1969). Short internal waves in the Strait of Gibraltar. In *Deep Sea Research and Oceanographic Abstracts*, volume 16, pages 479–487. Elsevier.